공학박사 학위논문

Evaluation of Train Runnability on Bridges Considering Train/Track/Wind Interaction

차량/궤도/바람 상호작용을 고려한 교량 상 열차 주행성 평가

2015년 2월

서울대학교 대학원

건설환경공학부

황 성 호

Abstract

Evaluation of Train Runnability on Bridges Considering Train/Track/Wind Interaction

Hwang, Sung Ho

Dept. of Civil & Environmental Engineering

The Graduate School

Seoul National University

A unified framework for the train/track/bridge/wind interaction was proposed under consideration of lateral action of wind. To reflect the contact phenomenon between wheel and rail, calculated were the contact positions, creepages and contact forces on the basis of the contact theory. By combining the Direct Stiffness Method (DSM) and Mode Superposition Method (MSM), track dynamics with 3-dimensional bridge interaction was applied with efficiency and accuracy for calculating both vertical and lateral wheelloads. Finally System Matrix Approximation (SMA) method was embedded into the MSM to reflect the aeroelastic effect in bridge/wind interaction.

The validity of the proposed framework was confirmed by comparing its result to that of VI-Rail or previous study for each interaction step. With this framework, some case studies investigated the factors that can affect the running characteristics of train. The evaluation for safety and running behavior was performed as a target of KTX running through Yeongjong Bridge, and finally the critical wind velocity was suggested after analyzing the result for various wind and train velocities on the basis of the assumed conditions and

criteria.

As a result, the train runnability on the bridge under cross wind, was more susceptible to the variation of wind velocity than the train velocity, because the response of running train is closely related to the acceleration and displacement of bridge. Therefore the aeroelastic effect that determines the behavior of bridge under strong wind loads, needs to be included in the runnability evaluation inevitably.

Keywords: Train/track/bridge/wind interaction, Runnability evaluation, Track dynamics, Bridge aeroelasticity

Student Number: 2005-30271

Contents

List of Tables

List of Figures

Chapter 1 Introduction

1.1 Background

To make trains faster and bridges longer has been a trend of engineering development for the past decades. The railway or civil engineers have to design and construct the longer bridge on which the train can run faster. As a result of overcoming such challenging problems, however, a few bridges with a very long span length were designed or built to carry both roadway and railway around the world, such as Tsing Ma Bridge (1,377m, Hong Kong, 1997), Minami Bisan-Seto Bridge (1,100m, Japan, 1988), Kita Bisan-Seto Bridge (990m, Japan, 1988), and Shimotsui Seto Bridge (940m, Japan, 1988).[1, 2] As a representative in domestic area, Yeongjong Bridge (300m, Korea, 2000) is opened to traffic in 2000 and still under operation to connect Incheon International Airport to Seoul.

Basically the railway vehicle running on the track can be usually subject to the lateral forces (e.g. the lateral impact by hunting motion, the centrifugal force during running on curve, the wind load by gust wind and the earthquake load, etc.) which may influence the running safety of train and could lead the carbody to the derailment or turn-over ultimately.[3] In addition, the long-span bridges are relatively flexible in the lateral direction. For example, the natural frequencies for Tsing Ma Bridge (suspension bridge) are as follows.[4]

- Lateral mode: 1^{st} 0.069Hz, 2^{nd} 0.164Hz
- Vertical mode: 1^{st} 0.113Hz, 2^{nd} 0.139Hz
- Torsional mode: 1^{st} 0.267Hz, 2^{nd} 0.320Hz

Therefore, it is most important to guarantee the safety of the vehicles running on long-span bridges under these lateral forces.

Deviated from the typical research for estimating the impact loads exerted on bridge[5-7], the research for the evaluating the running safety and behavior of train is increasing continuously.[8-12] For this kind of evaluation, a unified approach is necessary to integrate the train, track, bridge and even wind interaction, and it has to contain the analysis for both the vertical and lateral interaction. Especially the derailment coefficient and wheel load reduction rate, which are the main indices for running safety of railway vehicles, can be obtained after identifying the contact phenomenon between wheel and rail exactly. However the hardship to reflect the contact problem or to model the long bridge with track, has restricted the development of the evaluation method for runnability. An ‘efficiency’ problem would occur in the assessment of running safety when applying the unified framework including all the interactions.[13] Consequently there is almost no analysis carried out using such a unified method for a long-span bridge, and there are only limited analysis results by simplifying some of these interactions.

In summary,

- Bridges have been designed to take longer and longer span lengths.
- Long-span bridges are relatively flexible to the lateral-directional

movement.

- The trains running on the track can be derailed by climb-up, rollover, etc. in the lateral direction.
- There are increasing interests on the runnability of vehicles and trains on bridges.
- The evaluation for the long-span bridge has not been carried out due to the inefficiency of the unified analysis.

The train safety running on the long-span bridge is estimated to be very susceptible to wind load which can induce the vertical and lateral vibration of the long bridge.[11, 14] Therefore the unified approach which can assess the safety and running behavior considering train/track/bridge/wind interactions, has an important meaning not only for the bridges that were constructed already in-situ, but also for the long-span bridges that will be designed and constructed in the future.

1.2 Literature review

This section summarizes mainly the status of development in the individual interaction programs which compose the parts of the unified analysis program. Therefore, it deals with

① The rolling contact theory which is the most complex and can give the great affects to the train/track response

② The examples for the commercial or in-house programs that can analyze the train/track interaction

③ The review of mode superposition method that is useful to analyze long bridges, and

④ The vehicle/bridge/wind interaction to consider the effect of wind load.

1.2.1 Wheel/rail rolling contact theory

If an external load is applied on two bodies in contact, the two bodies will deform at the contact point to form an area of contact. The contact area in the case of the nonconformal contact is small as compared to the dimensions of the two bodies. In 1882, Hertz[15] presented a contact theory that accounts for the shape of the surfaces in the neighborhood of the contact area. Hertz assumed that the area of contact is elliptical. In wheel/rail dynamics, the assumption of nonconformal contact is often used, since the shapes of the wheel and rail surfaces are significantly different. In this case, the use of Hertz theory to examine the contact geometry and the maximum stresses can be justified. Hertz theory is the most commonly used theory to determine the shape of the contact

area and the normal contact force.

Due to the elasticity of the bodies and the externally applied normal load, some points on the surfaces in the contact region may slip while others may stick when the two bodies move relative to each other. The difference between the tangential strains of the bodies in the adhesion area loads to a small apparent slip. This slip is creepage defined by using the kinematics of the two bodies.

Creepages generate creep forces, such as tangential creep forces and creep spin moment. Many researchers made efforts to define the relationship between creepage and creep force for a long time. Carter[16] first was concerned with the action of locomotive wheels and thus found the braking or traction coupling. However, the Carter's formulation was based on the two-dimensional analysis for a cylinder rolling on a plane, which means it is not applicable to the complex geometries of wheel and rail.

Vermeulen and Johnson[17] proposed a creep force law, which included the longitudinal and the lateral creepages, and excluded only the spin creepage. They used Hertzian contact theory to calculate the shape and the size of wheel/rail contact. The treatment of the Hertz theory in detail can be seen in Johnson.[18]

The most successful method to calculate the creep force is presented by Kalker[19-21] who then wrote the computer program CONTACT, a universal program for all contact problems between two bodies that can be described by half-space. Because the CONTACT program is based on Kalker's exact theory and takes a long calculation time, it is not suitable for real time applications in vehicle dynamics. Concerned with this, in 1973 Kalker introduced the simplified theory of rolling contact and then used the theory to build a fast

algorithm and computer program FASTSIM.[22]

Although it is based on Kalker's work with simplification of the distribution of normal and tangential stresses in the wheel/rail contact patch, Polach[23] made another program for calculating creep forces, which is claimed to perform better under high creepage. According to this theory the creep forces can be computed efficiently with significant saving in computational effort.

More detailed discussion on the subject of rolling contact theory can be found in the literature Garg[24] and Shabana.[25]

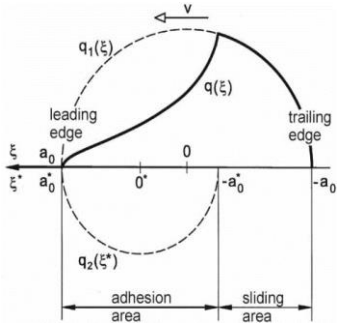

(a) Carter[16]

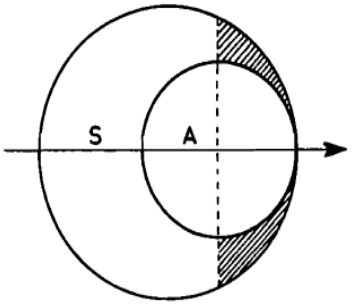

(b) Johnson[18]

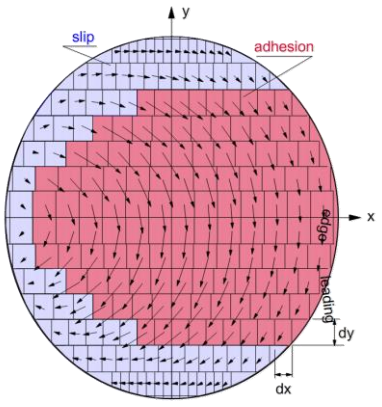

(c) Kalker[22]

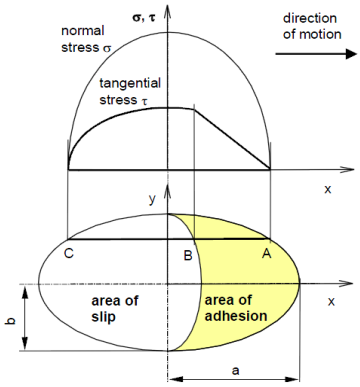

(d) Polach[23]

Figure 1.1 Various assumptions for contact patch

1.2.2 Train/track interaction

Many commercial packages for train/track interaction are now under development for a long time, such as ADAMS, GENSYS, NUCARS, SIMPACK, VAMPIRE, etc. These packages basically focus mainly on designing the train components (mass, suspension, damper and its dimensions) and analyzing the train responses only. Of course they embed the easy-handling pre- and post-analysis system with graphical support, and they can perform lots of analysis with regard to the vehicles, such as the stability analysis, mode analysis, etc. But they have some deficiencies with the modeling of track and substructure. In addition that the track is usually assumed to be simplified as rigid rails with little or no movement in these packages, the substructure such as bridge or tunnel cannot be modeled.

Shabana[25-32] reported a survey of train/track simulations which include flexible multibody dynamics. He suggested the parameterizing functions for expressing the profiles of wheel and rail in three-dimensional space, and the constraint equations for finding the contact points between them. In their paper they have pointed out that, with the recent development in computational mechanics, it is possible to develop a tool to comprehensively analyze the complex dynamics of railway vehicles and tracks.

In Queensland University in Australia, Handoko[33, 34] used the Shabana's method for finding the wheel/rail contact position and Polach's method for calculating the creep force. He developed 3-dimensional train/track interaction program which simulates the traction/braking forces between wheel and rail. It has a good accuracy in calculating the wheel/rail contact forces by finding the

wheel/rail contact position at every step, but some limitations like modeling just one bogie and no substructure.

Instead of the typical FE modeling for railway bridges, Yang[5, 6, 35-44] applied dynamic condensation technique and modal superposition for analyzing train/bridge interaction during earthquake. He deeply studied the development and cancellation of bridge resonance according to the train loads. However he focused on the bridge behaviors (neither the track nor train), so modeled very simplified track and did not include the wheel/rail contact mechanism directly.

The Railway Technical Research Institute (RTRI) in Japan has developed DIASTARS[45-47], that is the analysis program of train/track interaction. Differently from other commercial packages, DIASTARS focuses on track or bridge responses, not the train response, so it contains various nonlinear spring elements in track components. Especially it analyzed the train behavior interacting with and running on cable-stayed bridge during earthquake. Even though it uses the simplified wheel profiles as a contact input, it is evaluated as an excellent program in the train/track/bridge interaction fields.

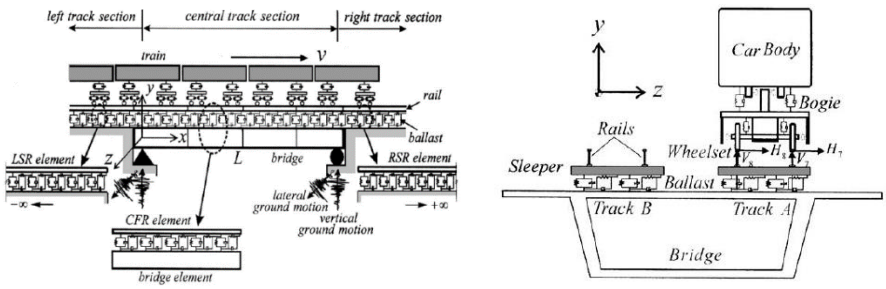

(a) Dynamic Condensation Technique (b) Track modeling

Figure 1.2 Bridge and track model of Yang[35]

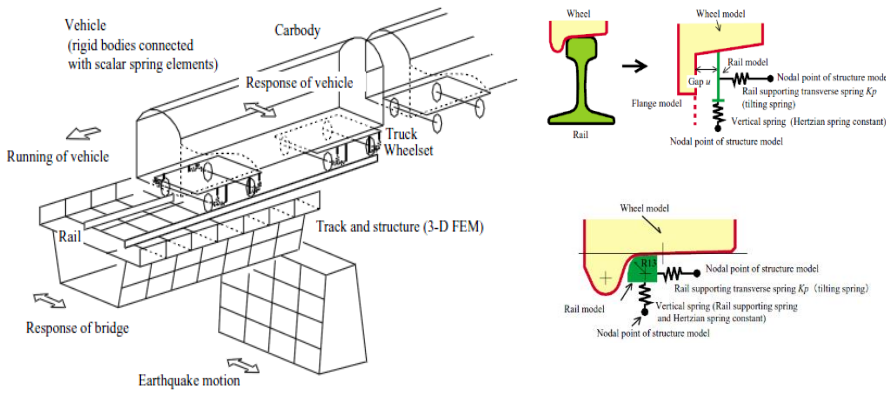

(a) Bridge model (b) Contact model

Figure 1.3 Bridge and contact model of DIASTARS[45]

Zhai, Cai and Xia[10, 48-58] in China continue to develop the 3-D train/track interaction program for many years. They use the common method to analyze the interaction between train and track, that is first to find the contact point between wheel and rail about one vehicle, second to calculate the normal forces using Hertzian nonlinear contact theory, and finally to calculate the tangential forces after computing the creepages using the geometrical condition and velocity differences at contact points. It is one of the most developed programs that includes very detailed track components such as rail movement and ballast behavior, thus it can simulate the roadbed condition. Recently they made the bridge model under the ballast or ballastless track by using Ritz's method to solve the governing equations.

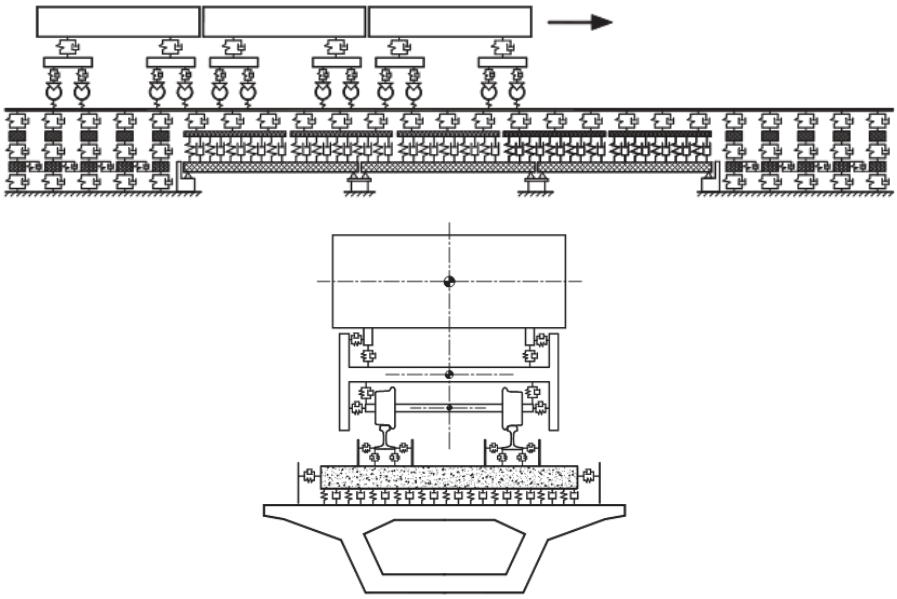

Figure 1.4 3D train/track interaction model of Zhai[50]

1.2.3 Mode superposition method

Most structures in civil engineering are so large and complex that the numerical simulation of them is not an easy work and even the analysis of dynamic response requires large computational efforts. But because the response of civil structures also tends to be definitely dependent upon the lower-order vibration mode, the Mode Superposition Method (MSM) is one of most widely used and efficient techniques in civil engineering. Basic equations for MSM is well defined in many literatures for structural dynamics, e.g. Chopra.[59]

Fryba[60] summarized the method to analyze the dynamic response of bridge including moving loads. He obtained the theoretical solution of simple beam

under loads or masses with constant velocity.

In National Taiwan University, the research team with Yang[5, 6, 35-44] published many papers and brought out a book based on these papers. It developed a new train/ bridge interaction program that uses this efficient MSM, not the FE model. It dealt with the basic phenomena about the resonance of bridge response and its cancelation by the train loads.

In domestic research, Lee[61] tried to analyze the vehicle/bridge interaction by deriving the governing equations of vehicle and bridge. But due to the complexity, he simplified the vehicle to only 1-DOF, applied MSM for modeling the bridge, and finally evaluated the influence factors to bridge/ vehicle interaction.

The Sungkyunkwan University applied this MSM to the railway field. Lim[62] showed the train movement on simple beams or 2-span continuous beams by deducing the theoretical result of modal analysis. Lee[63] developed this method to more complicated magnetic levitation system including the levitational force between train and structure.

Moreover, many programs for train/track or wind/train/track interaction have been developed using MSM. Most of them made the mode shapes of bridge including track, thus had a very good efficiency in analyzing interaction problems, but have a limitation that it is hard to calculate the accurate contact force between wheel and rail. The detailed explanation will be reviewed in 2.3.2.

1.2.4 Wind/vehicle/bridge analysis

Many long-span bridges have been built around the world in recent years, but they are often subject to multiple types of dynamic loads, especially those located in wind-prone regions and carrying both trains and road vehicles. To ensure the safety and functionality of these bridges, dynamic responses of long-span bridges are often required for bridge assessment.

The history of long-span bridge aerodynamics was reviewed by Miyata[64] and the basic theory of bridge aerodynamics is introduced well in Strømmen.[65]

Baker[66-68] developed a theoretical model that describes the dynamics of vehicles in crosswinds in the time domain. He further investigated both the steady and unsteady aerodynamic forces acting on a variety of vehicles and carried out extensive studies of the interaction between aerodynamic forces and moving vehicles.

A lot of analyses and experiments[68-73] for acquiring the aerodynamic coefficients of the train had performed for many years. They defined three forces (drag, side and lift forces) and three moments (rolling, pitching and yawing moments) induced by the interaction between train and wind. Especially Diedrichs[69] and Orellano[70] derived the aerodynamic coefficient for ICE II, and Kwon[73] for KTX by the Computational Fluid Dynamics (CFD) analysis and the wind tunnel test for scaled models.

The research team of Xu[4, 9, 11, 14, 52, 74-82] researched on the train/bridge/wind interactions without track dynamics for a long time. Xu et al. simulated the aerodynamic wind forces acting on running road vehicles using the quasi-steady approach, and they derived and simulated the steady and

unsteady aerodynamic forces acting on a moving railway vehicle in cross winds in the time domain. Li[82] simulated the two trains meeting each other on the long-span bridge under wind loads, and evaluated the acceleration of carbody for each vehicle.

Finally Chen[13] summarized recent research on the dynamic response of long-span bridges subject to wind load with a viewpoint of numerical simulation and simulation technology for bridge assessment.

1.3 Objectives and scope

Chen[13] said that "After multiple types of dynamic interactions being considered in the complex system, computational efficiency is a bottleneck problem for numerical simulation of dynamic response of a long-span bridge." There are following three problems that cause the inefficiency of unified analysis of train/track/bridge/wind interaction.

- *Nonlinear contact problem in train/track interaction* : The wheel/rail contact is defined as a nonlinear problem, and it needs the complex and time-consuming process for calculating contact positions and forces at all wheels in every time step. Moreover the nonlinearity needs the iteration process according to the train and track models.
- *Large DOFs in track/bridge interaction* : In contrast that track has to be modeled by Direct Stiffness Method (DSM) for the accurate evaluation, the long-span bridge needs too many degrees of freedom (DOFs) by DSM. Or the modeling of track and bridge by Mode Superposition Method (MSM) has a defect that the local track deflection is hard to be calculated as a combination of some lower modes. But the local deflection is a very sensitive factor that makes a great impact on the contact force between wheel and rail.
- *Aeroelasticity in bridge/wind interaction* : In order to predict the structural behavior under wind loads exactly, the aeroelasticity is needed to be reflected into the interaction of bridge and wind. For realizing such effects, some effective techniques are necessary to consider the frequency-dependent flutter derivatives in time domain.

Therefore, the main purpose of this study is to suggest a framework to integrate train/track/bridge/wind interaction under consideration of lateral behavior by wind, and to evaluate the runnability of train on a bridge subject wind loads for an example.

To develop such a unified framework, first of all, the contact modeling between wheel and rail is necessary for exact calculation of vertical/ lateral wheelload and train acceleration. After finding the accurate contact points of the assumed wheel and rail profile, the creepages, normal forces, creep forces and contact forces will be calculated by the contact theory. For the track/bridge interaction, the combination of track model with DSM and bridge with MSM is recommended as an accurate and efficient way. Therefore the hybrid method that combining the DSM and MSM will be proposed for calculating exact contact forces and simultaneously reducing the computing time. Finally in order to reflect the aeroelastic effect in bridge/wind interaction, System Matrix Approximation (SMA) method will be applied as it is useful to be applied into the MSM and has a good accuracy even it approximates the aerodynamic transfer function.

It needs to be checked whether the proposed method is valid or not. However, there is no comparable target program that integrates all the interactions discussed above. Therefore the verification of the suggested framework will be made by comparing its result to that of VI-Rail or previous study for each interaction step – train/track interaction, track/bridge interaction and bridge/ wind interaction, respectively.

After completing verification, main simulation for KTX train running on Yeongjong Bridge will be performed for two scenarios. First will be the analysis

to figure out the influence factors that can affect the behavior of running train, such as the effect of bridge, track irregularity or wind load. The other will focus on identifying the relationship between bridge and train acceleration.

Finally the runnability of KTX train on Yeongjong Bridge will be assessed. In order to evaluate the runnability, the simulation will be performed for the combination of six different wind velocities and five different train velocities with five random wind seeds. Consequently the critical wind velocity to limit the train passage under the strong wind for the target bridge will be suggested.

1.4 Outline of this thesis

This thesis contains 6 chapters that cover the formulation, verification and application of the suggested unified approach.

Chapter 1 outlines the background, objective, scope and literature review.

Chapter 2 describes overall framework for train/track/bridge/wind interaction and its algorithm. It introduces the main subsystems and processes which compose the train/track/bridge/wind interaction program. The train model is composed, and the interface of track and bridge is modeled by combination of DSM and MSM with the wind interaction by SMA.

Chapter 3 verifies the proposed approach by comparing other research results. The verification of the algorithm is divided into three major parts : ① 3-D analysis of wheel/rail interface which includes finding the contact points and calculating the creepages and contact forces, ② track/bridge interaction part that checks the appropriate result by combining the DSM and MSM, and ③ wind/bridge interaction including the aeroelastic deformation of bridge.

Chapter 4 performs some case studies for KTX train running on Yeongjong Bridge. Numerical comparative study is done for figuring out the effect of bridge, wind and irregularity, and the relationship between bridge and train acceleration.

Chapter 5 evaluates the runnability of KTX on Yeongjong Bridge for various wind and train velocity, analyzes the main indices which cause the main affects to the runnability of KTX, and finally suggests the critical wind velocity.

Chapter 6 finally provides the summary of this study and lists the conclusions that have deduced from this research.

Chapter 2 Framework for train/track/ bridge/wind interaction

2.1 Overview of the suggested framework

The main algorithm for the suggested framework in this study looks similar to the other dynamic programs in a way that it has the iterative procedure to determine the displacements and forces in every sequence. This study divides the whole system into two subsystems (① train and ② track including bridge by means of mode superposition) and two processes. (① contact-solving process and ② iteration process)

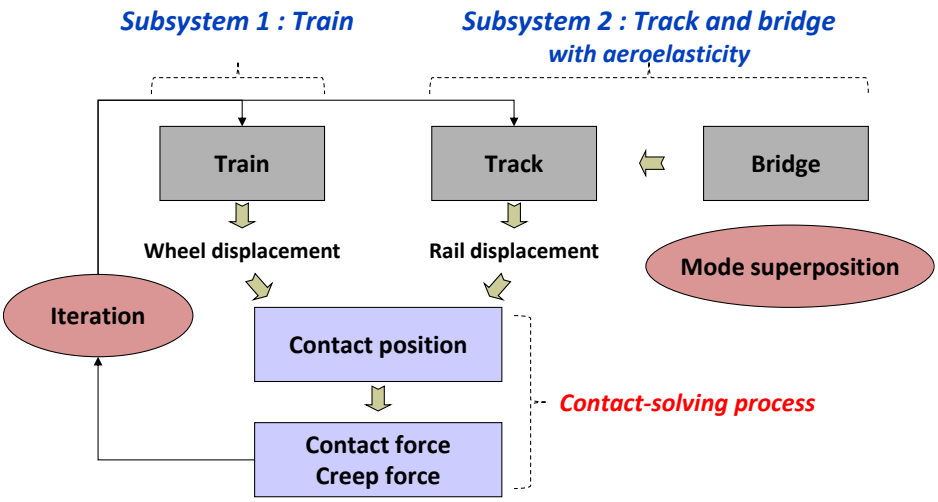

Figure 2.1 Main algorithm of the suggested framework

The two subsystems are aimed to model the train and its substructure respectively. The train subsystem has just tens of DOFs (degrees-of-freedom) per one train, depending on the train type and the interesting DOFs. The carbody, bogie, and wheelset are modeled as lumped masses with the connection to other components as spring and damper systems. And the basic equations of motions are derived from the Lagrange's equation, which uses the energy terms defined by the relative deformation and velocity of spring and damper in section 2.2.

The track subsystem has huge amount of DOFs because it contains many nodes along a pair of rails and even includes the modal DOFs for bridge. The track is modeled by direct stiffness method (DSM) and the bridge is modeled by mode superposition method (MSM). Both methods are combined after deriving some equations through sharing the interface nodes between track and bridge in section 2.3.2.

The effect of the wind load has to be included into modeling the bridge by mode superposition, because the aeroelasticity is reflected through changing the system matrix of bridge. The aeroelasticity of bridge is reflected in this modal superposition as a method of system matrix approximation (SMA). The detailed explanation of embedding SMA into MSM is in section 2.3.3.

The process for solving the contact problems has three main sub-processes. The target of first sub-process is to determine the contact points between wheel and rail at each wheelset position. The sub-process for the contact point needs the information of wheel profile, rail profile and the track irregularity in order to find the maximum penetration depth between wheel and rail according to their relative position. The sub-process for creepage uses the previous result

including geometry information and the basic contact coefficients, which is used widely in many references, and finally calculates the creep forces at each contact points between wheel and rail. Then both the wheel contact force and rail contact force are calculated from the previous creep forces by transforming and summing up. The more information is explored in section 2.4.

As the wind also acts as an external force to bridge and train, respectively, it needs to be calculated at every time step. Because the wind load on bridge is not deterministic but has some random characteristics in nature, its simulation on the basis of the determined spectrum and characteristics has to be performed ahead. The wind load on train can be calculated from the aerodynamic coefficients defined in the train aerodynamics, like section 2.5.

The iterative procedure is necessary to reflect the nonlinear property of Hertzian contact force and creep force between wheel and rail. The calculated contact forces are applied to the two subsystems by the law of action and reaction, and determine the displacements of train or track, which are used for checking the convergence of iteration. The detailed explanation is written in section 2.6.

2.2 Train modeling

The train system is one of the simplest and most independent system in this whole framework. It models the train as carbody, bogie and wheelset by combining their mass, dashpot and spring elements. The calculation of train response is made independently and its result is applied to evaluate the contact force between wheel and rail. This study chose KTX (Korea Train eXpress) for a target model which runs 300km/h on Korean high speed line.

The basic mass, damping and stiffness matrix for KTX was suggested by Park[83] and revised by Song.[84] Both papers derived the equations of motion for an individual car by substituting the equations that define the kinetic energy (E_k), potential energy (E_p) and damping energy (E_d) into Lagrange's equation like Eq. (2-1).

$$\frac{d}{dt}\left(\frac{\partial E_k}{\partial \dot{q}_v}\right) - \frac{\partial E_k}{\partial q_v} + \frac{\partial E_p}{\partial q_v} + \frac{\partial E_d}{\partial \dot{q}_v} = 0 \qquad (2\text{-}1)$$

where E_k : kinetic energy

E_p : potential energy

E_d : damping energy

q_v: vector of D.O.Fs of train

Each energy term is expressed as the combination of inertia terms for kinetic energy, relative deformations of suspension for potential energy, and relative velocities of suspension for damping energy like Eq. (2-2)

- Kinetic energy (E_k)

$$E_k = \frac{1}{2}\left[m_c\left(\dot{x}_c^2 + \dot{y}_c^2 + \dot{z}_c^2\right) + \left(I_{xc}\dot{\phi}_c^2 + I_{yc}\dot{\theta}_c^2 + I_{zc}\dot{\psi}_c^2\right)\right] + \frac{1}{2}\sum_{i=1}^{2}\left[m_{bi}\left(\dot{x}_{bi}^2 + \dot{y}_{bi}^2 + \dot{z}_{bi}^2\right) + \left(I_{x_{bi}}\dot{\phi}_{bi}^2 + I_{y_{bi}}\dot{\theta}_{bi}^2 + I_{z_{bi}}\dot{\varphi}_{bi}^2\right)\right] + \frac{1}{2}\sum_{i=1}^{4}\left[m_{wi}\left(\dot{x}_{wi}^2 + \dot{z}_{wi}^2\right) + \left(I_{x_{wi}}\dot{\phi}_{wi}^2 + I_{z_{wi}}\dot{\varphi}_{wi}^2\right)\right]$$

- Potential energy (E_p)

$$E_p = \frac{1}{2}\left[\sum_{i=1}^{4} K_{sxi}R_{K_{sxi}}^2 + \sum_{i=1}^{4} K_{syi}R_{K_{syi}}^2 + \sum_{i=1}^{4} K_{szi}R_{K_{szi}}^2 + \sum_{i=1}^{8} K_{pxi}R_{K_{pxi}}^2 + \sum_{i=1}^{8} K_{pyi}R_{K_{pyi}}^2 + \sum_{i=1}^{8} K_{pzi}R_{K_{pzi}}^2 + \sum_{i=1}^{4} K_{bsyi}R_{K_{bsyi}}^2\right] \quad (2\text{-}2)$$

- Damping energy (E_d)

$$E_d = \frac{1}{2}\left[\sum_{i=1}^{2} D_{syi}\dot{R}_{D_{syi}}^2 + \sum_{i=1}^{4} D_{szi}\dot{R}_{D_{szi}}^2 + \sum_{i=1}^{4} D_{yawi}\dot{R}_{D_{yawi}}^2 + \sum_{i=1}^{8} D_{pxi}\dot{R}_{D_{pxi}}^2 + \sum_{i=1}^{8} D_{pyi}\dot{R}_{D_{pyi}}^2 + \sum_{i=1}^{8} D_{pzi}\dot{R}_{D_{pzi}}^2\right]$$

and according to the geometric relationship, the relative deformations are defined as the Eq. (2-3) that are referred from Park[83] and Song[84] with minor modification.

$$
\begin{aligned}
R_{K_{sxi}} &= (-1)^{l}\left(x_c - x_{bl} - h_1\theta_c - h_2\theta_{bl}\right) + (-1)^{m} e_1\left(\varphi_c - \varphi_{bl}\right) \\
R_{K_{syi}} &= (-1)^{i}\left(y_c - y_{bl} + h_1\phi_c + h_2\phi_{bl}\right) + (-1)^{m} L_l\varphi_c \\
R_{K_{szi}} &= -z_c + z_{bl} + (-1)^{l+1} L_l\theta_c + (-1)^{i+1} e_1\left(\phi_c - \phi_{bl}\right) \\
R_{K_{bsyi}} &= (-1)^{i}\left[y_c - y_{bl} + \left(h_1 + h_2 - h_{bs}\right)\phi_c\right] + (-1)^{m} L_l\varphi_c
\end{aligned}
$$

$$
\begin{aligned}
R_{D_{yawi}} &= (-1)^{l}\left[x_c - x_{bl} - \left(h_1 + h_2 + h_{yaw}\right)\theta_c - h_{yaw}\theta_{bl}\right] \\
&\quad + (-1)^{m} e_3\left(\varphi_c - \varphi_{bl}\right) \\
R_{D_{syk}} &= (-1)^{k+1}\left[y_c - y_{bk} + \left(h_1 + h_2 - h_d\right)\phi_c + h_d\phi_{bk}\right] + L_k\varphi_c \\
R_{D_{szi}} &= -z_c + z_{bl} + (-1)^{l+1} L_l\theta_c + (-1)^{i+1} e_2\left(\phi_c - \phi_{bl}\right)
\end{aligned}
\qquad \text{(2-3)}
$$

$$
\begin{aligned}
R_{K_{pxj}} &= R_{D_{pxj}} = (-1)^{u+1}\left(x_{bn} - x_{au} - h_3\theta_{bn}\right) + (-1)^{v+1} b_u\left(\varphi_{bn} - \varphi_{au}\right) \\
R_{K_{pyj}} &= R_{D_{pyj}} = (-1)^{j+1}\left(x_{bn} - y_{au} + h_3\phi_{bn}\right) + (-1)^{v+1} a\varphi_{bn} \\
R_{K_{pzj}} &= R_{D_{pzj}} = -z_{bn} + z_{au} + (-1)^{u+1} a\theta_{bn} + (-1)^{j+1} b_u\left(\phi_{bn} - \phi_{au}\right)
\end{aligned}
$$

where s : the secondary suspension (i=1 to 4)

p : the primary suspension (j=1 to 8)

yaw : the yawing damper (k=1 to 2)

bs : bump stop

l=integer[(i+1)/2], m=integer[(i+2)/2]

n=integer[(j+3)/4], u=integer[(j+1)/2], v=integer[(j+2)/2]

x, y, z : translational displacement along longitudinal, lateral and vertical axis, respectively

ϕ, θ, φ : rotational displacement about longitudinal, lateral and vertical axis, respectively

c, b, a : carbody, bogie and axle(wheelset), repectively

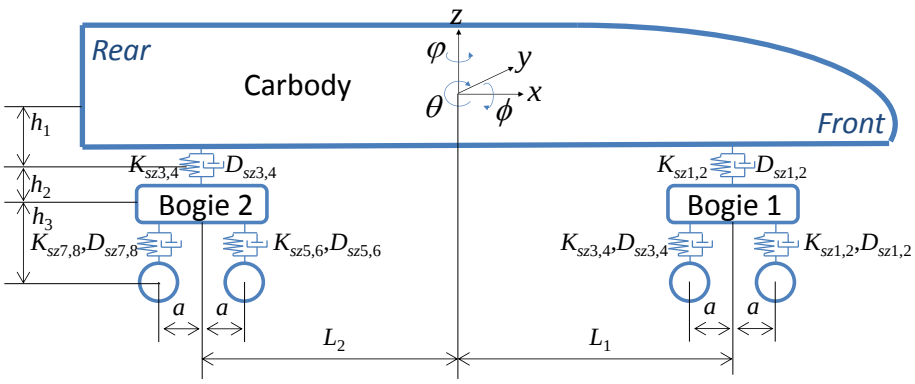

(a) Side view

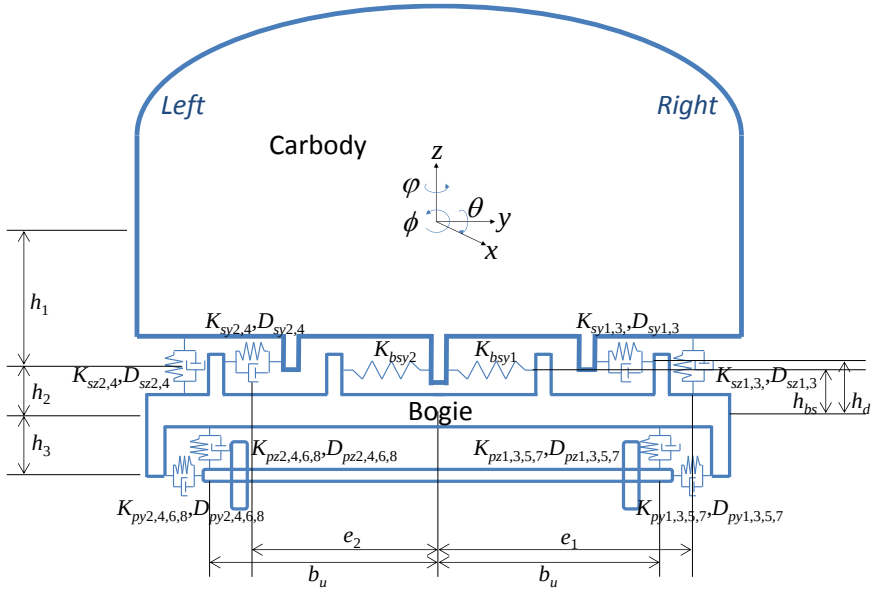

(b) Front view

Figure 2.2 Geometry of suspension in power car of KTX[83]

This study uses the same method for KTX modeling used in Park[83] and Song[84], but simplifies a few nonlinear elements such as traction link and yaw damper to linear ones. Just one power car is considered in this model and the other cars are modeled as moving masses at their wheelset position. The power car is composed of one car body, two bogies (front and rear) and 4 wheelsets (8 wheels). Each component can have 6 DOFs but the rotational DOFs of 4 wheelsets about y-axis are ignored because all the wheelsets are assumed to have the same angular velocity. So total count of train DOFs is $6 \times 7 - 4 = 38$.

Modeling not all the train but only one power car is known to evaluate the train responses more conservatively because the link between two adjacent carbodies gives a kind of constraint which decreases the response of each bodies. And the reason to add moving masses after the power car is to reflect the additional deflection from the wheelloads of subsequent carbodies and their reciprocal influence to the response of the first power car.

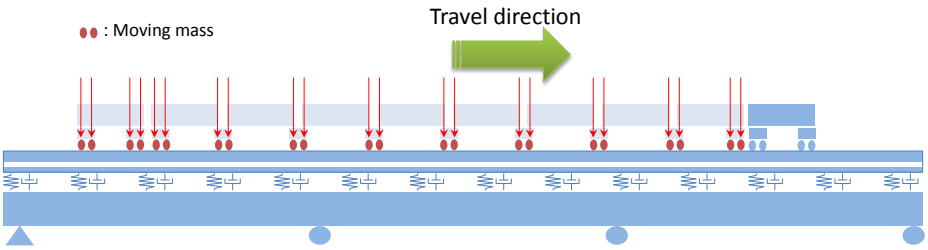

Figure 2.3 Modeling of moving mass for the subsequent vehicles

Table 2.1 General properties of power car of KTX[84]

(a) Dynamic properties of the mass constituent elements in power car of KTX

Mass of body	Weight (ton)	Height of centroid (m)	Inertia moment (ton·m^4)		
			I_x	I_y	I_z
Carbody	54.916	1.72	59.4	1131.9	1112.0
Bogie	2.446	0.56	1.645	2.593	3.068
Wheelset	2.048	0.46	1.03	0.11	1.03

(b) Dynamic properties of the primary suspension in power car of KTX

Spring coefficient (MN/m)			Damping coefficient (MN·s/m)		
K_{px}	K_{py}	K_{pz}	D_{px}	D_{py}	D_{pz}
40.581	9.581	1.252	0.010	0.022	0.010

(c) Dynamic properties of the secondary suspension in power car of KTX

Spring coefficient (MN/m) (Coil and elastic bearing)			Damping coefficient (MN·s/m)		
K_{sx}	K_{sy}	K_{sz}	D_{yaw}	D_{sy}	D_{sz}
0.302	0.302	1.268	4.23	0.10	0.02

2.3 Composition of track and bridge system

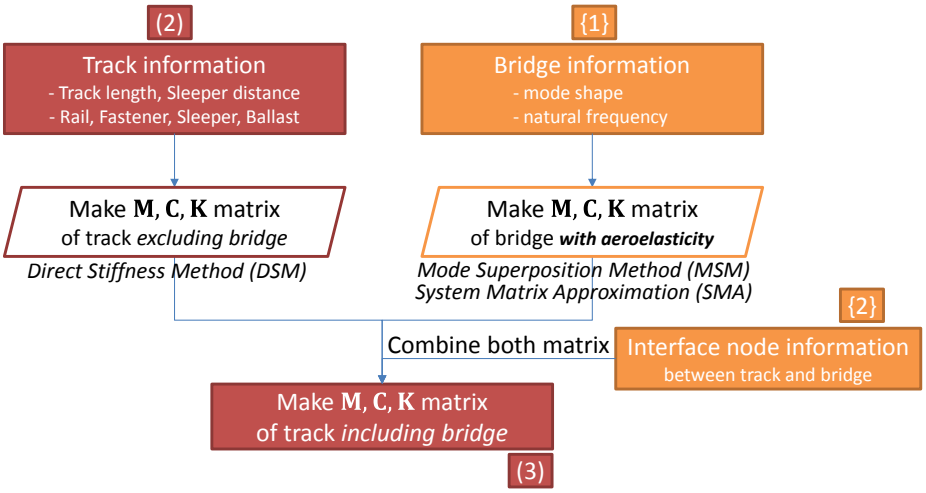

Figure 2.4 Flowchart of track/bridge interaction

2.3.1 Track modeling by direct stiffness method

The contact forces between the wheel and rail, which are significantly affected by the behavior of the track, are the important parameters in evaluating the train safety. The track behavior is affected by many factors including the nonlinear contact spring between wheel and rail, the bending stiffness of the rail, the shear deformation of the rail, the discrete support condition of the sleepers, and the mechanical behavior of track components, such as rails and fasteners. Most of the track components can be feasibly modeled with finite elements. Therefore, in this study, the track is modeled by applying the direct stiffness method.

The track model is also represented as a 3D one-layer track, which consists of track components such as rails and fasteners. The top rail is modeled as a

continuous Timoshenko beam. The fasteners are represented by linear springs and dashpots, and the sleeper is represented by a mass.

There are two nodes between one sleeper length per a rail for reproducing the sleeper motion, and each node has three DOFs for translational modes and the other three DOFs for rotational modes because the rails are modeled as three dimensional beam elements. Then track has many nodes along the whole length under consideration. When we consider the long bridge with 550m length and place one element between two sleepers, total node would be over 1,800 then the number of DOFs over 11,000. This is only the node for rails excluding any bridge nodes, which means that the modeling of detailed track and bridge with long span needs very long CPU time and memory capacity in computer to handle such big matrix. This is why this study introduced Mode Superposition Method (MSM) in modeling the bridge part. If the track and bridge is combined with MSM, the increasing number of DOFs for bridge is limited to the amount of interesting modes. The next paragraph 2.3.2 will deal with the detailed derivation and explanation for modal superposition.

When just considering the modeling of the track only, the long distance of rail still becomes a burden to be modeled. In fact, the deformation of track occurs in a narrow area (3~5m) around the loading point of wheel, and the displacement of track outside the train length is almost zero on the roadbed or as same as the displacement of substructure. Therefore the track can be modeled just 60~100m long for one power car for calculating wheel/rail contact, and it can move with the train along its designed direction. Basic concept of moving track model is depicted in Figure 2.5.

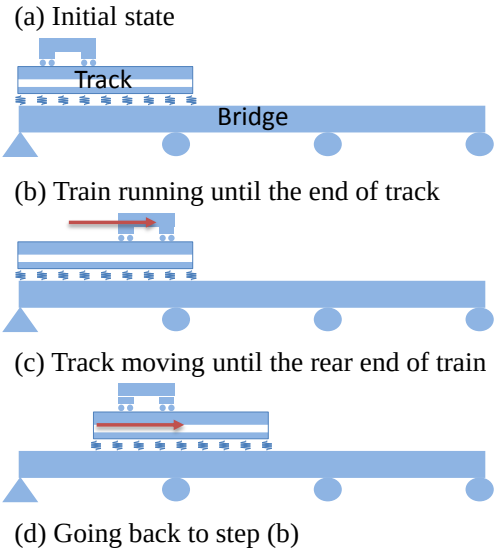

Figure 2.5 Basic concept of moving track

2.3.2 Bridge modeling by mode superposition method

The bridges can be modeled from any kind of programs, such as commercial FE packages or in-house programs that can make model of and analyze the bridge by modal superposition for structural analysis.

A track-bridge coupled model is created by combining the track model obtained with typical Direct Stiffness Method (DSM) and the bridge model obtained through MSM, which is introduced below.

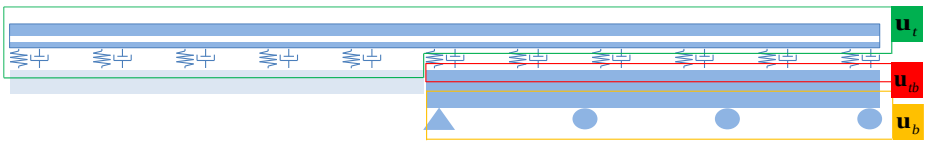

Figure 2.6 Definition of track/bridge/interface DOFs

The equilibrium equation of the individual track and bridge system, shown in Figure 2.6, can be expressed as follows.

$$\begin{bmatrix} \mathbf{M}_{11}^{t} & \mathbf{M}_{12}^{t} \\ \mathbf{M}_{21}^{t} & \mathbf{M}_{22}^{t} \end{bmatrix} \begin{pmatrix} \ddot{\mathbf{u}}_{t} \\ \ddot{\mathbf{u}}_{tb} \end{pmatrix} + \begin{bmatrix} \mathbf{C}_{11}^{t} & \mathbf{C}_{12}^{t} \\ \mathbf{C}_{21}^{t} & \mathbf{C}_{22}^{t} \end{bmatrix} \begin{pmatrix} \dot{\mathbf{u}}_{t} \\ \dot{\mathbf{u}}_{tb} \end{pmatrix}$$
$$+ \begin{bmatrix} \mathbf{K}_{11}^{t} & \mathbf{K}_{12}^{t} \\ \mathbf{K}_{21}^{t} & \mathbf{K}_{22}^{t} \end{bmatrix} \begin{pmatrix} \mathbf{u}_{t} \\ \mathbf{u}_{tb} \end{pmatrix} = \begin{pmatrix} \mathbf{p}_{t} \\ \mathbf{p}_{tb}^{t} \end{pmatrix} \tag{2-4}$$
$$\Rightarrow \quad \mathbf{M}^{T}\ddot{\mathbf{u}}_{T} + \mathbf{C}^{T}\dot{\mathbf{u}}_{T} + \mathbf{K}^{T}\mathbf{u}_{T} = \mathbf{p}_{T}$$

$$\begin{bmatrix} \mathbf{M}_{11}^{b} & \mathbf{M}_{12}^{b} \\ \mathbf{M}_{21}^{b} & \mathbf{M}_{22}^{b} \end{bmatrix} \begin{pmatrix} \ddot{\mathbf{u}}_{tb} \\ \ddot{\mathbf{u}}_{b} \end{pmatrix} + \begin{bmatrix} \mathbf{C}_{11}^{b} & \mathbf{C}_{12}^{b} \\ \mathbf{C}_{21}^{b} & \mathbf{C}_{22}^{b} \end{bmatrix} \begin{pmatrix} \dot{\mathbf{u}}_{tb} \\ \dot{\mathbf{u}}_{b} \end{pmatrix}$$
$$+ \begin{bmatrix} \mathbf{K}_{11}^{b} & \mathbf{K}_{12}^{b} \\ \mathbf{K}_{21}^{b} & \mathbf{K}_{22}^{b} \end{bmatrix} \begin{pmatrix} \mathbf{u}_{tb} \\ \mathbf{u}_{b} \end{pmatrix} = \begin{pmatrix} \mathbf{p}_{tb}^{b} \\ \mathbf{p}_{b} \end{pmatrix} \tag{2-5}$$
$$\Rightarrow \quad \mathbf{M}^{B}\ddot{\mathbf{u}}_{B} + \mathbf{C}^{B}\dot{\mathbf{u}}_{B} + \mathbf{K}^{B}\mathbf{u}_{B} = \mathbf{p}_{B}$$

where **M**, **C**, **K** : mass, damping, and stiffness matrix, respectively

u : nodal displacement vector

p : nodal load vector

superscripts *t* (*T*) and *b* (*B*) : the track and the bridge system, respectively (italic style, not roman)

subscripts *t* : DOFs of the track

subscripts *tb* : DOFs of the bridge which is in contact with the track (interface DOFs)

subscripts *b* : DOFs of the bridge except interface DOFs

Eq. (2-5) for the bridge part can be compacted by using the modeshape for bridge as $\boldsymbol{\Phi}_B = \{\boldsymbol{\Phi}_{tb} \quad \boldsymbol{\Phi}_b\}^{\mathrm{T}}$ in MSM[59] as follows.

$$\begin{aligned} &\boldsymbol{\Phi}_B^{\mathrm{T}}\mathbf{M}^B\boldsymbol{\Phi}_B\ddot{\mathbf{q}} + \boldsymbol{\Phi}_B^{\mathrm{T}}\mathbf{C}^B\boldsymbol{\Phi}_B\dot{\mathbf{q}} + \boldsymbol{\Phi}_B^{\mathrm{T}}\mathbf{K}^B\boldsymbol{\Phi}_B\mathbf{q} = \boldsymbol{\Phi}_B^{\mathrm{T}}\mathbf{p}_B \\ &\Rightarrow \quad \mathbf{M}_N^B\ddot{\mathbf{q}} + \mathbf{C}_N^B\dot{\mathbf{q}} + \mathbf{K}_N^B\mathbf{q} = \boldsymbol{\Phi}_B^{\mathrm{T}}\mathbf{p}_B \end{aligned} \tag{2-6}$$

where $\mathbf{M}_N^B, \mathbf{C}_N^B, \mathbf{K}_N^B$: modal matrix for mass, damping, and stiffness

$\mathbf{M}_N^B = \boldsymbol{\Phi}_B^T\mathbf{M}^B\boldsymbol{\Phi}_B$

$\mathbf{C}_N^B = \boldsymbol{\Phi}_B^T\mathbf{C}^B\boldsymbol{\Phi}_B$

$\mathbf{K}_N^B = \boldsymbol{\Phi}_B^T\mathbf{K}^B\boldsymbol{\Phi}_B$

N : total number of DOFs

T : transpose of the matrix (roman style, not italic)

Since both Eq. (2-4) and (2-5) use the same displacement vector, $\mathbf{u}_{tb}$, as the interface nodes, they can be collected to Eq. (2-7) for compatibility condition.

$$\begin{aligned} &\begin{bmatrix} \mathbf{M}_{11}^t & \mathbf{M}_{12}^t & \mathbf{0} \\ \mathbf{M}_{21}^t & \mathbf{M}_{22}^t & \mathbf{0} \\ \mathbf{0} & \mathbf{0} & \mathbf{0} \end{bmatrix}\begin{pmatrix} \ddot{\mathbf{u}}_t \\ \ddot{\mathbf{u}}_{tb} \\ \ddot{\mathbf{u}}_b \end{pmatrix} + \begin{bmatrix} \mathbf{0} & \mathbf{0} & \mathbf{0} \\ \mathbf{0} & \mathbf{M}_{11}^b & \mathbf{M}_{12}^b \\ \mathbf{0} & \mathbf{M}_{21}^b & \mathbf{M}_{22}^b \end{bmatrix}\begin{pmatrix} \ddot{\mathbf{u}}_t \\ \ddot{\mathbf{u}}_{tb} \\ \ddot{\mathbf{u}}_b \end{pmatrix} \\ &+ \begin{bmatrix} \mathbf{C}_{11}^t & \mathbf{C}_{12}^t & \mathbf{0} \\ \mathbf{C}_{21}^t & \mathbf{C}_{22}^t & \mathbf{0} \\ \mathbf{0} & \mathbf{0} & \mathbf{0} \end{bmatrix}\begin{pmatrix} \dot{\mathbf{u}}_t \\ \dot{\mathbf{u}}_{tb} \\ \dot{\mathbf{u}}_b \end{pmatrix} + \begin{bmatrix} \mathbf{0} & \mathbf{0} & \mathbf{0} \\ \mathbf{0} & \mathbf{C}_{11}^b & \mathbf{C}_{12}^b \\ \mathbf{0} & \mathbf{C}_{21}^b & \mathbf{C}_{22}^b \end{bmatrix}\begin{pmatrix} \dot{\mathbf{u}}_t \\ \dot{\mathbf{u}}_{tb} \\ \dot{\mathbf{u}}_b \end{pmatrix} \\ &+ \begin{bmatrix} \mathbf{K}_{11}^t & \mathbf{K}_{12}^t & \mathbf{0} \\ \mathbf{K}_{21}^t & \mathbf{K}_{22}^t & \mathbf{0} \\ \mathbf{0} & \mathbf{0} & \mathbf{0} \end{bmatrix}\begin{pmatrix} \mathbf{u}_t \\ \mathbf{u}_{tb} \\ \mathbf{u}_b \end{pmatrix} + \begin{bmatrix} \mathbf{0} & \mathbf{0} & \mathbf{0} \\ \mathbf{0} & \mathbf{K}_{11}^b & \mathbf{K}_{12}^b \\ \mathbf{0} & \mathbf{K}_{21}^b & \mathbf{K}_{22}^b \end{bmatrix}\begin{pmatrix} \mathbf{u}_t \\ \mathbf{u}_{tb} \\ \mathbf{u}_b \end{pmatrix} = \begin{pmatrix} \mathbf{p}_t \\ \mathbf{p}_{tb} \\ \mathbf{p}_b \end{pmatrix} \end{aligned} \tag{2-7}$$

where $\mathbf{p}_{tb} = \mathbf{p}_{tb}^t + \mathbf{p}_{tb}^b = \mathbf{p}_{tb}^b \ (\because \mathbf{p}_{tb}^t = 0)$

The displacement of bridge can be expressed as the multiplication of shape function and generalized coordinate as Eq (2-8). For satisfying the compatibility condition, the overall displacement vector of the coupling system can be expressed as the nodal displacements of the track, and the generalized coordinates (**q**) of the modal analysis of the bridge.

$$\mathbf{u} = \begin{pmatrix} \mathbf{u}_t \\ \mathbf{u}_{tb} \\ \mathbf{u}_b \end{pmatrix} = \begin{bmatrix} \mathbf{I} & \mathbf{0} \\ \mathbf{0} & \mathbf{\Phi}_{tb} \\ \mathbf{0} & \mathbf{\Phi}_b \end{bmatrix} \begin{pmatrix} \mathbf{u}_t \\ \mathbf{q} \end{pmatrix} = \mathbf{\Phi}\bar{\mathbf{u}} \tag{2-8}$$

where **I** : identity matrix

$\mathbf{\Phi}_{tb}$: the modal matrix for interface DOFs

$\mathbf{\Phi}_b$: the modal matrix for bridge except interface DOFs

q : vector of generalized coordinate

$\mathbf{u}_{tb} = \mathbf{\Phi}_{tb}\mathbf{q}, \mathbf{u}_b = \mathbf{\Phi}_b\mathbf{q}$ as compatibility condition

$\mathbf{\Phi} = \begin{bmatrix} \mathbf{I} & \mathbf{0} \\ \mathbf{0} & \mathbf{\Phi}_{tb} \\ \mathbf{0} & \mathbf{\Phi}_b \end{bmatrix}$: compatibility matrix

$\bar{\mathbf{u}} = \begin{pmatrix} \mathbf{u}_t \\ \mathbf{q} \end{pmatrix}$: displacement vector

The modal matrix is defined as a matrix that contains the values of the modal shape functions at the target DOFs. When *P* number of modes are considered with *Q* number of interface DOFs and total DOFs of bridge is *R* number, then $\mathbf{\Phi}_{tb}$ becomes an $Q \times P$ matrix and $\mathbf{\Phi}_b$ becomes an $(R-Q)\times P$ matrix.

If the displacement vector, $\mathbf{u}$ in Eq. (2-7) is replaced with $\overline{\mathbf{u}}$, and both sides of the equation are multiplied by $\boldsymbol{\Phi}^{\mathrm{T}}$ for equilibrium condition, Eq. (2-7) can be written as follows.

$$\begin{aligned}
&\begin{bmatrix} \mathbf{M}_{11}^{t} & \mathbf{M}_{12}^{t}\boldsymbol{\Phi}_{tb} \\ \boldsymbol{\Phi}_{tb}^{T}\mathbf{M}_{21}^{t} & \boldsymbol{\Phi}_{tb}^{T}\mathbf{M}_{22}^{t}\boldsymbol{\Phi}_{tb} \end{bmatrix}\begin{pmatrix} \ddot{\mathbf{u}}_{t} \\ \ddot{\mathbf{q}} \end{pmatrix}+\begin{bmatrix} \mathbf{0} & \mathbf{0} \\ \mathbf{0} & \begin{pmatrix} \boldsymbol{\Phi}_{tb} \\ \boldsymbol{\Phi}_{b} \end{pmatrix}^{\mathrm{T}}\begin{bmatrix} \mathbf{M}_{11}^{b} & \mathbf{M}_{12}^{b} \\ \mathbf{M}_{21}^{b} & \mathbf{M}_{22}^{b} \end{bmatrix}\begin{pmatrix} \boldsymbol{\Phi}_{tb} \\ \boldsymbol{\Phi}_{b} \end{pmatrix} \end{bmatrix}\begin{pmatrix} \ddot{\mathbf{u}}_{t} \\ \ddot{\mathbf{q}} \end{pmatrix} \\
&+\begin{bmatrix} \mathbf{C}_{11}^{t} & \mathbf{C}_{12}^{t}\boldsymbol{\Phi}_{tb} \\ \boldsymbol{\Phi}_{tb}^{\mathrm{T}}\mathbf{C}_{21}^{t} & \boldsymbol{\Phi}_{tb}^{\mathrm{T}}\mathbf{C}_{22}^{t}\boldsymbol{\Phi}_{tb} \end{bmatrix}\begin{pmatrix} \dot{\mathbf{u}}_{t} \\ \dot{\mathbf{q}} \end{pmatrix}+\begin{bmatrix} \mathbf{0} & \mathbf{0} \\ \mathbf{0} & \begin{pmatrix} \boldsymbol{\Phi}_{tb} \\ \boldsymbol{\Phi}_{b} \end{pmatrix}^{\mathrm{T}}\begin{bmatrix} \mathbf{C}_{11}^{b} & \mathbf{C}_{12}^{b} \\ \mathbf{C}_{21}^{b} & \mathbf{C}_{22}^{b} \end{bmatrix}\begin{pmatrix} \boldsymbol{\Phi}_{tb} \\ \boldsymbol{\Phi}_{b} \end{pmatrix} \end{bmatrix}\begin{pmatrix} \dot{\mathbf{u}}_{t} \\ \dot{\mathbf{q}} \end{pmatrix} \\
&+\begin{bmatrix} \mathbf{K}_{11}^{t} & \mathbf{K}_{12}^{t}\boldsymbol{\Phi}_{tb} \\ \boldsymbol{\Phi}_{tb}^{\mathrm{T}}\mathbf{K}_{21}^{t} & \boldsymbol{\Phi}_{tb}^{\mathrm{T}}\mathbf{K}_{22}^{t}\boldsymbol{\Phi}_{tb} \end{bmatrix}\begin{pmatrix} \mathbf{u}_{t} \\ \mathbf{q} \end{pmatrix}+\begin{bmatrix} \mathbf{0} & \mathbf{0} \\ \mathbf{0} & \begin{pmatrix} \boldsymbol{\Phi}_{tb} \\ \boldsymbol{\Phi}_{b} \end{pmatrix}^{\mathrm{T}}\begin{bmatrix} \mathbf{K}_{11}^{b} & \mathbf{K}_{12}^{b} \\ \mathbf{K}_{21}^{b} & \mathbf{K}_{22}^{b} \end{bmatrix}\begin{pmatrix} \boldsymbol{\Phi}_{tb} \\ \boldsymbol{\Phi}_{b} \end{pmatrix} \end{bmatrix}\begin{pmatrix} \mathbf{u}_{t} \\ \mathbf{q} \end{pmatrix} \\
&=\begin{pmatrix} \mathbf{p}_{t} \\ \boldsymbol{\Phi}_{tb}^{\mathrm{T}}\mathbf{p}_{tb}+\boldsymbol{\Phi}_{b}^{\mathrm{T}}\mathbf{p}_{b} \end{pmatrix}
\end{aligned} \tag{2-9}$$

Since the (2,2) element of the each second matrix in the above equation expresses the generalized stiffness obtained from the modal analysis, Eq. (2-9) can be expressed as follows.

$$\begin{aligned}
&\begin{bmatrix} \mathbf{M}_{11}^{t} & \mathbf{M}_{12}^{t}\boldsymbol{\Phi}_{tb} \\ \boldsymbol{\Phi}_{tb}^{\mathrm{T}}\mathbf{M}_{21}^{t} & \boldsymbol{\Phi}_{tb}^{\mathrm{T}}\mathbf{M}_{22}^{t}\boldsymbol{\Phi}_{tb}+\mathbf{M}_{N}^{B} \end{bmatrix}\begin{pmatrix} \ddot{\mathbf{u}}_{t} \\ \ddot{\mathbf{q}} \end{pmatrix} \\
&+\begin{bmatrix} \mathbf{C}_{11}^{t} & \mathbf{C}_{12}^{t}\boldsymbol{\Phi}_{tb} \\ \boldsymbol{\Phi}_{tb}^{\mathrm{T}}\mathbf{C}_{21}^{t} & \boldsymbol{\Phi}_{tb}^{\mathrm{T}}\mathbf{C}_{22}^{t}\boldsymbol{\Phi}_{tb}+\mathbf{C}_{N}^{B} \end{bmatrix}\begin{pmatrix} \dot{\mathbf{u}}_{t} \\ \dot{\mathbf{q}} \end{pmatrix} \\
&+\begin{bmatrix} \mathbf{K}_{11}^{t} & \mathbf{K}_{12}^{t}\boldsymbol{\Phi}_{tb} \\ \boldsymbol{\Phi}_{tb}^{\mathrm{T}}\mathbf{K}_{21}^{t} & \boldsymbol{\Phi}_{tb}^{\mathrm{T}}\mathbf{K}_{22}^{t}\boldsymbol{\Phi}_{tb}+\mathbf{K}_{N}^{B} \end{bmatrix}\begin{pmatrix} \mathbf{u}_{t} \\ \mathbf{q} \end{pmatrix}=\begin{pmatrix} \mathbf{p}_{t} \\ \boldsymbol{\Phi}_{tb}^{\mathrm{T}}\mathbf{p}_{tb}+\boldsymbol{\Phi}_{b}^{\mathrm{T}}\mathbf{p}_{b} \end{pmatrix}
\end{aligned} \tag{2-10}$$

where $\mathbf{M}_{N}^{B}=\mathrm{diag}\left(M_{1},\cdots,M_{N}\right)$

$$\mathbf{C}_N^B = \mathrm{diag}\left(2\xi_1\omega_1 M_1, \cdots, 2\xi_N\omega_N M_N\right)$$
$$\mathbf{K}_N^B = \mathrm{diag}\left(M_1\omega_1^2, \cdots, M_N\omega_N^2\right)$$

diag(⋯) : diagonal matrix composed of ⋯

A new stiffness matrix (the same as that for the mass and damping matrix) for a track/bridge system would be obtained by the manipulation of Eq. (2-9), which is carried out by multiplying the sub-matrices ($\mathbf{K}_{11}$, $\mathbf{K}_{12}$ and $\mathbf{K}_{22}$) of the track stiffness matrix with the modal value matrix ($\mathbf{\Phi}_{tb}$) at interface DOFs and by adding the generalized stiffness of the bridge.

This study sets the Yeongjong Bridge as a bridge model, because the bridge is the only long span cable-supported bridge which carries railway in Korea. In order to connect the Incheon international airport to Seoul station by high-speed railway, the operation line for KTX is extended to the airport recently. Consequently it is a good chance to evaluate the runnability of KTX on Yeongjong Bridge.

There is one alternative to solve the problem of track-bridge interaction; to extract the modes of track and bridge as a whole. The alternative is usually used in the commercial multibody dynamics (MBD) packages, but is not recommended in a sense that modal superposition method is not efficient to calculate the local deflection of rail between two sleepers with enough precision. Because the rail deflection occurs in a narrow length about 3~5m but gives a big effect to the magnitude of contact force, the accurate calculation for rail deflection at the contact point needs large amount of modes, thus the advantage to use modal superposition method has vanished.

2.3.3 Bridge/wind interaction by system matrix approximation

Most needed in the application of wind velocity is a special method that can be embedded into MSM and easily handle the aeroelasticity in time domain. System Matrix Approximation (SMA), proposed by Jung[85], is the very feasible method in a sense that it can use the truncated modal decomposition in the structural eigenvector space, and eliminate the dependency of the structural aerodynamic transfer function on frequency. SMA method can be summarized as follows, and the detailed derivation and application is addressed in Jung.[85]

The governing equation for bridge under the action of wind is expressed as Eq. (2-11) in dynamic virtual work expression of a discretized structure.

$$\delta\mathbf{u}_B^{\mathrm{T}}\mathbf{M}^B\ddot{\mathbf{u}}_B + \delta\mathbf{u}_B^{\mathrm{T}}\mathbf{C}^B\dot{\mathbf{u}}_B + \delta\mathbf{u}_B^{\mathrm{T}}\mathbf{K}^B\mathbf{u}_B = \delta\Pi_{ad} + \delta\mathbf{u}_B^{\mathrm{T}}\mathbf{p}_B \tag{2-11}$$

where $\mathbf{M}^B$, $\mathbf{C}^B$, $\mathbf{K}^B$: mass, damping and stiffness matrix of bridge

$\mathbf{p}_B$: equivalent nodal force vector

$\mathbf{u}_B$: nodal displacement vector

δ : virtual quantity

$\delta\Pi_{ad}$: external virtual work done by self-excited forces

The Fourier transform of Eq. (2-11) yields the dynamic virtual work expression of an aeroelastic system in the frequency domain

$$\begin{aligned}\Im(\delta\Pi) = \delta\mathbf{u}_B^{\mathrm{T}}\Big[&\left\{-\omega^2\mathbf{M}^B + i\omega\mathbf{C}^B + \mathbf{K}^B - \boldsymbol{\Psi}_{ad}(\omega)\right\}\Im(\mathbf{u}_B) \\ &- \Im(\mathbf{p}_B)\Big] = 0\end{aligned} \tag{2-12}$$

where $\boldsymbol{\Psi}_{ad}(\omega)$: structural aerodynamic transfer function

$\Im(\cdot)$: Fourier transform operator

Because Eq. (2-12) should hold for all admissible $\delta\mathbf{u}_B$, the equation of motion for a structure that is subject to the action of wind is derived in the frequency domain like following equation.

$$\left[-\omega^2\mathbf{M}^B + i\omega\mathbf{C}^B + \mathbf{K}^B - \boldsymbol{\Psi}_{ad}(\omega)\right]\Im(\mathbf{u}_B) = \Im(\mathbf{p}_B) \tag{2-13}$$

The inverse Fourier transform of Eq. (2-13) yields the equation of motion in the time domain, which contains the well-known convolution expression for the aerodynamic force.

$$\mathbf{M}^B\ddot{\mathbf{u}}_B + \mathbf{C}^B\dot{\mathbf{u}}_B + \mathbf{K}^B\mathbf{u}_B = \mathbf{p}_B + \int_0^t \boldsymbol{\Phi}_{ad}(t-\tau)\mathbf{u}_B(\tau)d\tau \tag{2-14}$$

where $\boldsymbol{\Phi}_{ad}$: aerodynamic impulse response function matrix

SMA approximates structural aerodynamic transfer function by a second-order polynomial with respect to frequency as follows.

$$\boldsymbol{\Psi}_{ad}(\omega) \approx \tilde{\boldsymbol{\Psi}}_{ad}(\omega) = -\omega^2\tilde{\mathbf{M}}^B + i\omega\tilde{\mathbf{C}}^B + \tilde{\mathbf{K}}^B \tag{2-15}$$

where $\tilde{\boldsymbol{\Psi}}_{ad}(\omega)$: approximate structural aerodynamic transfer function

$\tilde{\mathbf{M}}^B, \tilde{\mathbf{C}}^B, \tilde{\mathbf{K}}^B$: unknown coefficient matrices

And the aeroelastic transfer function in Eq. (2-13) is approximated using Eq. (2-15)

$$\begin{aligned}\boldsymbol{\Theta} \approx \tilde{\boldsymbol{\Theta}} &= \left[-\omega^2\mathbf{M}^B + i\omega\mathbf{C}^B + \mathbf{K}^B - \tilde{\boldsymbol{\Psi}}_{ad}(\omega)\right]^{-1} \\ &= \left[-\omega^2\tilde{\mathbf{M}}_{ae}^B + i\omega\tilde{\mathbf{C}}_{ae}^B + \tilde{\mathbf{K}}_{ae}^B\right]^{-1}\end{aligned} \tag{2-16}$$

where $\boldsymbol{\Theta}$, $\tilde{\boldsymbol{\Theta}}$: aeroelastic transfer function and its approximation

$$\tilde{\mathbf{M}}_{ae}^B = \mathbf{M}^B - \tilde{\mathbf{M}}^B,\ \tilde{\mathbf{C}}_{ae}^B = \mathbf{C}^B - \tilde{\mathbf{C}}^B,\ \tilde{\mathbf{K}}_{ae}^B = \mathbf{K}^B - \tilde{\mathbf{K}}^B$$

After substituting Eq. (2-15) into Eq. (2-13), Fourier transform of it yields the approximate equation of motion defined as a usual second-order differential equation in the time domain like Eq. (2-17)

$$\begin{aligned}&\left(\mathbf{M}^B - \tilde{\mathbf{M}}^B\right)\ddot{\mathbf{u}}_B + \left(\mathbf{C}^B - \tilde{\mathbf{C}}^B\right)\dot{\mathbf{u}}_B + \left(\mathbf{K}^B - \tilde{\mathbf{K}}^B\right)\mathbf{u}_B = \mathbf{p}_B \\ &\Rightarrow\quad \tilde{\mathbf{M}}_{ae}^B\ddot{\mathbf{u}}_B + \tilde{\mathbf{C}}_{ae}^B\dot{\mathbf{u}}_B + \tilde{\mathbf{K}}_{ae}^B\mathbf{u}_B = \mathbf{p}_B\end{aligned} \tag{2-17}$$

Like the analysis of bridge by mode superposition, the aeroelastic system matrices can be reduced to by the truncated modal decomposition for the computational efficiency. Jung[85] deduced the relationship between the displacement of the aeroelastic system and the vector of generalized coordinate like Eq. (2-18).

$$\mathbf{u}_B = \boldsymbol{\Phi}_B\mathbf{q} = \sum_{j=1}^{N}\boldsymbol{\varphi}_j q_j(t) \tag{2-18}$$

where $\mathbf{u}_B$: nodal displacement vector of bridge

$\mathbf{\Phi}_B$: the eigenvector matrix

$\mathbf{q}$: vector of generalized coordinate

Because the dynamic behavior of a structural system can be accurately estimated with several dominant modes in many dynamic problems, it may be assumed without any loss of generality that several lower modes in Eq. (2-18) dominate the aerodynamic behaviors of a structure. With this assumption, the displacement of an aeroelastic system may be approximated by truncating Eq. (2-18) at j=1 to $M \leq N$.

$$\mathbf{u}_B \approx \mathbf{\Phi}_{Br}\mathbf{q}_r = \sum_{j=1}^{M} \boldsymbol{\varphi}_j q_j(t) \tag{2-19}$$

where $\mathbf{\Phi}_{Br}$: the truncated eigenvector matrix

$\mathbf{q}_r$: the truncated vector of generalized coordinate

r : the truncated or reduced system

M : reduced number of DOFs

The truncated equation of motion of the aeroelastic system for the generalized coordinates is derived by the substitution of Eq. (2-19) into Eq. (2-13)

$$\begin{aligned} &\mathbf{\Phi}_{Br}^{\mathrm{T}}\left[-\omega^2\mathbf{M}^B + i\omega\mathbf{C}^B + \mathbf{K}^B - \mathbf{\Psi}_{ad}(\omega)\right]\mathbf{\Phi}_{Br}\Im(\mathbf{u}_B) \\ &= \mathbf{\Phi}_{Br}^{\mathrm{T}}\Im(\mathbf{p}_B) \end{aligned} \tag{2-20}$$

The aeroelastic transfer function in the reduced solution space, $\tilde{\mathbf{\Theta}}_r$ is defined as

$$\tilde{\boldsymbol{\Theta}}_r = \left[-\omega^2 \mathbf{M}^{Br} + i\omega \mathbf{C}^{Br} + \mathbf{K}^{Br} - \tilde{\boldsymbol{\Psi}}^r_{ad}(\omega) \right]^{-1} \tag{2-21}$$

where $\tilde{\boldsymbol{\Theta}}_r$: aeroelastic transfer function in the reduced solution space

$$\mathbf{M}^{Br} = \boldsymbol{\Phi}_{Br}^{\mathrm{T}} \mathbf{M}^{B} \boldsymbol{\Phi}_{Br}$$
$$\mathbf{C}^{Br} = \boldsymbol{\Phi}_{Br}^{\mathrm{T}} \mathbf{C}^{B} \boldsymbol{\Phi}_{Br}$$
$$\mathbf{K}^{Br} = \boldsymbol{\Phi}_{Br}^{\mathrm{T}} \mathbf{K}^{B} \boldsymbol{\Phi}_{Br}$$
$$\tilde{\boldsymbol{\Psi}}^r_{ad} = \boldsymbol{\Phi}_{Br}^{\mathrm{T}} \tilde{\boldsymbol{\Psi}}_{ad} \boldsymbol{\Phi}_{Br}$$

The approximate relationship of Eq. (2-15) in the reduced solution space is given as

$$\boldsymbol{\Psi}^r_{ad}(\omega) \approx \tilde{\boldsymbol{\Psi}}^r_{ad}(\omega) = -\omega^2 \tilde{\mathbf{M}}^{Br} + i\omega \tilde{\mathbf{C}}^{Br} + \tilde{\mathbf{K}}^{Br} \tag{2-22}$$

where $\tilde{\boldsymbol{\Psi}}^r_{ad}(\omega)$: approximate structural aerodynamic transfer function in the reduced solution space

$\tilde{\mathbf{M}}^{Br}, \tilde{\mathbf{C}}^{Br}, \tilde{\mathbf{K}}^{Br}$: unknown coefficient matrices in the reduced solution space

The approximate aeroelastic transfer function is defined in the reduced solution space using Eqs. (2-21) and (2-22)

$$\begin{aligned} \tilde{\boldsymbol{\Theta}}_r &= \left[-\omega^2 \mathbf{M}^{Br} + i\omega \mathbf{C}^{Br} + \mathbf{K}^{Br} - \tilde{\boldsymbol{\Psi}}^r_{ad}(\omega) \right]^{-1} \\ &= \left[-\omega^2 \tilde{\mathbf{M}}^{Br}_{ae} + i\omega \tilde{\mathbf{C}}^{Br}_{ae} + \tilde{\mathbf{K}}^{Br}_{ae} \right]^{-1} \end{aligned} \tag{2-23}$$

where $\tilde{\mathbf{M}}^{Br}_{ae}, \tilde{\mathbf{C}}^{Br}_{ae}, \tilde{\mathbf{K}}^{Br}_{ae}$: modal matrix for mass, damping, and stiffness with consideration of aeroelasticity in the reduced solution space

$$\tilde{\tilde{\mathbf{M}}}_{ae}^{Br} = \mathbf{M}^{Br} - \tilde{\tilde{\mathbf{M}}}^{Br}$$
$$\tilde{\tilde{\mathbf{C}}}_{ae}^{Br} = \mathbf{C}^{Br} - \tilde{\tilde{\mathbf{C}}}^{Br}$$
$$\tilde{\tilde{\mathbf{K}}}_{ae}^{Br} = \mathbf{K}^{Br} - \tilde{\tilde{\mathbf{K}}}^{Br}$$

Substitution of Eq. (2-23) into Eq. (2-20) and the inverse Fourier transform of the resulting equation lead to the approximate equation of motion in the reduced solution space

$$\tilde{\tilde{\mathbf{M}}}_{ae}^{Br}\ddot{\mathbf{q}}^{r} + \tilde{\tilde{\mathbf{C}}}_{ae}^{Br}\dot{\mathbf{q}}^{r} + \tilde{\tilde{\mathbf{K}}}_{ae}^{Br}\mathbf{q}^{r} = \boldsymbol{\Phi}_{Br}^{T}\mathbf{p}_{B} \tag{2-24}$$

The modal matrices ($\tilde{\tilde{\mathbf{M}}}_{ae}^{Br}, \tilde{\tilde{\mathbf{C}}}_{ae}^{Br}, \tilde{\tilde{\mathbf{K}}}_{ae}^{Br}$) in Eq. (2-23) can be embedded into Eq. (2-10) in MSM like Eq. (2-25).

$$\begin{aligned}
&\begin{bmatrix} \mathbf{M}_{11}^{t} & \mathbf{M}_{12}^{t}\boldsymbol{\Phi}_{tb,r} \\ \boldsymbol{\Phi}_{tb,r}^{\mathrm{T}}\mathbf{M}_{21}^{t} & \boldsymbol{\Phi}_{tb,r}^{\mathrm{T}}\mathbf{M}_{22}^{t}\boldsymbol{\Phi}_{tb,r} + \tilde{\tilde{\mathbf{M}}}_{ae}^{Br} \end{bmatrix} \begin{pmatrix} \ddot{\mathbf{u}}_{t} \\ \ddot{\mathbf{q}} \end{pmatrix} \\
&+ \begin{bmatrix} \mathbf{C}_{11}^{t} & \mathbf{C}_{12}^{t}\boldsymbol{\Phi}_{tb,r} \\ \boldsymbol{\Phi}_{tb,r}^{\mathrm{T}}\mathbf{C}_{21}^{t} & \boldsymbol{\Phi}_{tb,r}^{\mathrm{T}}\mathbf{C}_{22}^{t}\boldsymbol{\Phi}_{tb,r} + \tilde{\tilde{\mathbf{C}}}_{ae}^{Br} \end{bmatrix} \begin{pmatrix} \dot{\mathbf{u}}_{t} \\ \dot{\mathbf{q}} \end{pmatrix} \\
&+ \begin{bmatrix} \mathbf{K}_{11}^{t} & \mathbf{K}_{12}^{t}\boldsymbol{\Phi}_{tb,r} \\ \boldsymbol{\Phi}_{tb,r}^{\mathrm{T}}\mathbf{K}_{21}^{t} & \boldsymbol{\Phi}_{tb,r}^{\mathrm{T}}\mathbf{K}_{22}^{t}\boldsymbol{\Phi}_{tb,r} + \tilde{\tilde{\mathbf{K}}}_{ae}^{Br} \end{bmatrix} \begin{pmatrix} \mathbf{u}_{t} \\ \mathbf{q} \end{pmatrix} \\
&= \begin{pmatrix} \mathbf{p}_{T} \\ \boldsymbol{\Phi}_{tb,r}^{\mathrm{T}}\mathbf{p}_{tb} + \boldsymbol{\Phi}_{Br}^{\mathrm{T}}\mathbf{p}_{B} \end{pmatrix}
\end{aligned} \tag{2-25}$$

where $\boldsymbol{\Phi}_{tb,r}$: : the truncated eigenvector matrix at the interface node

Now remaining is how to determine the unknown coefficient matrices ($\tilde{\mathbf{M}}^B, \tilde{\mathbf{C}}^B, \tilde{\mathbf{K}}^B$) in Eq. (2-15). The detailed derivation is written in Jung[85] and summarized as follows.

The unknown coefficient matrices, $\tilde{\mathbf{M}}^B, \tilde{\mathbf{C}}^B, \tilde{\mathbf{K}}^B$, can be determined through minimizing the weighted error between the exact and approximate transfer functions by using the weighting function of the exact aeroelastic transfer function. The weighted error matrix of the approximation in Eq. (2-22) is defined by the modulus of a complex number of each component

$$\begin{aligned}\mathbf{E} &= |E_{kl}| = \left[\left|\Psi_{kl}^r - \tilde{\Psi}_{kl}^r\right| w_{kl}\right] \\ &= \left[\left\{\left[\left(\Psi_{kl}^r\right)^R - \left(-\omega^2 \tilde{M}_{kl}^r + \tilde{K}_{kl}^r\right)\right]^2 + \left[\left(\Psi_{kl}^r\right)^I - \omega \tilde{C}_{kl}^r\right]^2\right\}^{0.5} w_{kl}\right]\end{aligned} \tag{2-26}$$

where $\mathbf{E}$, E_{kl} : error matrix and its components

w_{kl} : predefined weighting function

$(\cdot)^R$, $(\cdot)^I$: real and imaginary part

$|\cdot|$: modulus of a complex number

The unknown coefficient matrices are determined by minimizing the norm of the weighted errors in Eq. (2-26)

$$\begin{aligned}\min_{\tilde{\mathbf{M}}^r, \tilde{\mathbf{C}}^r, \tilde{\mathbf{K}}^r} \Pi &= \int_0^{\omega_{\max}} \|\mathbf{E}\|_F^2 \, d\omega = \sum_{k=1}^{mf} \sum_{l=1}^{mf} \int_0^{\omega_{\max}} E_{kl}^2 \, d\omega \\ &= \sum_{k=1}^{mf} \sum_{l=1}^{mf} \left\{ \int_0^{\omega_{\max}} \left[\left(\Psi_{kl}^r\right)^R - (-\omega^2 \tilde{M}_{kl}^r + \tilde{K}_{kl}^r)\right]^2 w_{kl}^2 \, d\omega \right. \\ &\qquad \left. + \int_0^{\omega_{\max}} \left[\left(\Psi_{kl}^r\right)^I - \omega \tilde{C}_{kl}^r\right]^2 w_{kl}^2 \, d\omega \right\}\end{aligned} \tag{2-27}$$

where $\|\cdot\|_F$: Frobenius norm of a matrix

$\omega_{\max}$: maximum frequency that defines the maximum frequency range of the structural aerodynamic transfer function

and the minimization problem of Eq. (2-27) at each component is a quadratic form with only three unknowns, the computational effort for determining the coefficient matrices becomes trivial. The first-order optimality condition yields the following linear algebraic equations:

$$\begin{bmatrix} \int_0^{\omega_{\max}} \omega^4 w_{kl}^2 d\omega & 0 & -\int_0^{\omega_{\max}} \omega^2 w_{kl}^2 d\omega \\ 0 & \int_0^{\omega_{\max}} \omega^2 w_{kl}^2 d\omega & 0 \\ -\int_0^{\omega_{\max}} \omega^2 w_{kl}^2 d\omega & 0 & \int_0^{\omega_{\max}} w_{kl}^2 d\omega \end{bmatrix} \begin{pmatrix} \tilde{M}_{kl}^r \\ \tilde{C}_{kl}^r \\ \tilde{K}_{kl}^r \end{pmatrix} = \begin{pmatrix} -\int_0^{\omega_{\max}} \omega^2 \left(\Psi_{kl}^r\right)^R w_{kl}^2 d\omega \\ \int_0^{\omega_{\max}} \omega^2 \left(\Psi_{kl}^r\right)^I w_{kl}^2 d\omega \\ \int_0^{\omega_{\max}} \left(\Psi_{kl}^r\right)^R w_{kl}^2 d\omega \end{pmatrix} \tag{2-28}$$

The weighting functions in the error matrix are introduced to consider the responses of an aeroelastic system in approximating the structural aerodynamic transfer functions. The weighting function should represent magnitudes of responses of the real aeroelastic system, and thus the transfer function of an aeroelastic system in the reduced solution space given in Eq. (2-21) is recommended to be a good choice for the weighting function in Jung.[85]

$$w_{kl} = \left|\Theta_{kl}^r\right| = \left|\left[-\omega^2 M_{kl}^r + i\omega C_{kl}^r + K_{kl}^r - \tilde{\Psi}_{kl}^r(\omega)\right]^{-1}\right| \tag{2-29}$$

2.4 Implementation of wheel/rail interface

2.4.1 Determination of contact position

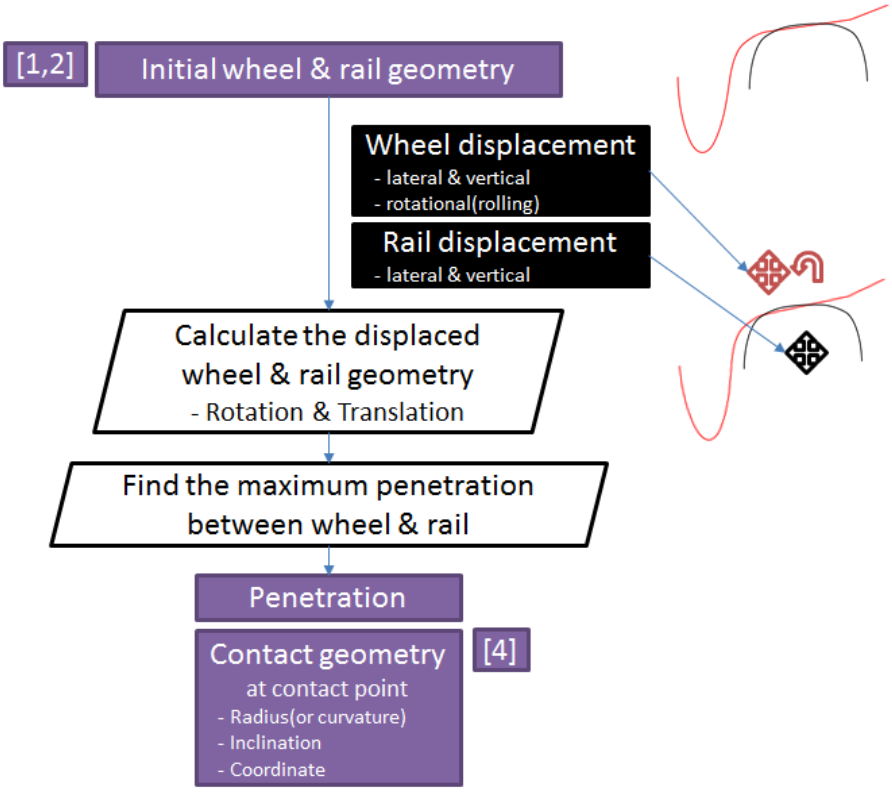

Figure 2.7 Flowchart for finding contact point

If the rail is assumed to be rigid and fixed, i.e. no rail movement occurs, then the calculation of wheel/rail contact point is simple and dependent only upon the wheel displacement, but in reality the rail can move and it makes the contact problems more complex. The wheel can move laterally and vertically, and rotate about longitudinal axis, and even the rail can also do it. So in every single

step, initial profiles of wheel and rail have to be translated and rotated according to their displacements respectively. Then the maximum penetration depth between the displaced wheel and rail profiles can be calculated by some simple arithmetic to solve the geometry problem.

In order to consider the worn profiles of wheel and rail, the measured data of profiles have to be analyzed by using some interpolation skills, like spline analysis. Because the interpolation skill needs much calculation time for every contact-point-searching algorithm, so it is assumed to use the new profiles of wheel and rail without any wear.

Since new rail profile is usually symmetric and divided into five parts, and has actually only three different curvatures, it is very easy to idealize and make numerical formula for it. But the wheel profile is difficult to be defined as simple combination of polynomials because it is very complex like Figure 2.8(a). It needs to be simplified, and this study uses two linear functions to express tread and flange contact respectively. (Figure 2.8(b))

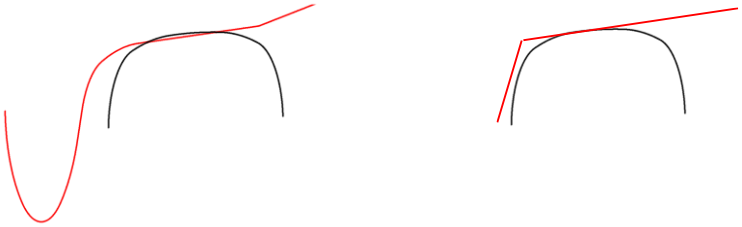

(a) Original profile (b) Bilinear profile

Figure 2.8 Simplification of wheel profile (original to bilinear)

Therefore the contact-point-searching algorithm is now focused on finding the maximum distance and its position between two 1st order linear equations and three 2nd order circular equations like Figure 2.9. The two 1st order linear equations have to be translated and rotated according to the displacement of wheelset, and the three center coordinates of 2nd order circular equations have to be moved according to the rail displacement. The rotational displacement of rail is ignored and the rotation of center coordinate is omitted.

The penetration is easily obtained as a subtraction from the circle radius to the distance from the center of circle to the linear equation. The penetration of right or left contact can be expressed like

$$\begin{aligned}\delta_{\text{Tread}} &= \max\left(R_{R3} - d_{R3}, \text{NaN}\right)\\ \delta_{\text{Flange}} &= \max\left(R_{R1} - d_{R1}, \text{NaN}\right)\end{aligned} \tag{2-30}$$

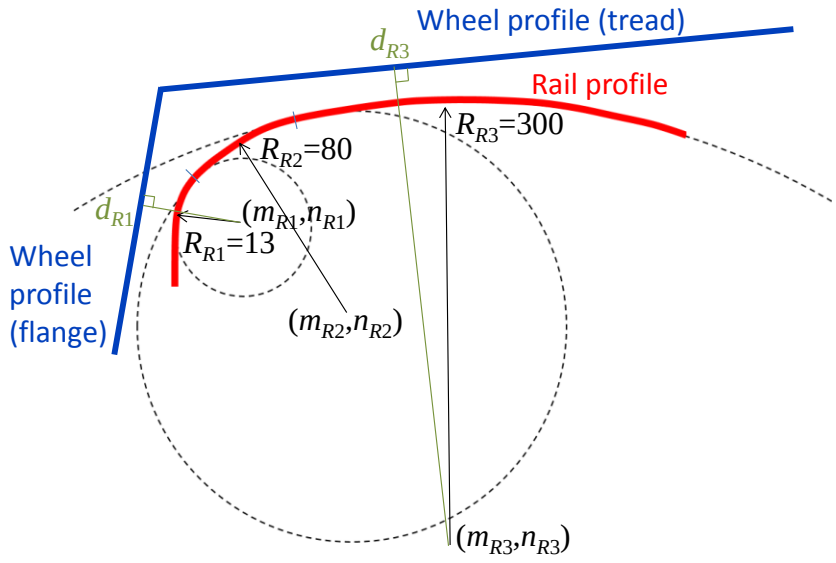

Figure 2.9 Scheme for wheel/rail contact

where δ_i : penetration at the i range (i=Tread or Flange)

R_{Rj} : radius of rail profile at j-th circle (where j=1,2,3)

(R_{R1}=13mm, R_{R2}=80mm, R_{R3}=300mm)

d_{Rj} : distance from the center of j-th circle to the linear equation

NaN : Not-a-Number, which means no penetration

(separation b/w wheel and rail)

In this equation, d_{Rj} can be obtained as follows. When the linearized wheel profile before translation and rotation is expressed as eq. (2-31)

$$y_1 = a_{w1i} x_1 + b_{w1i} \tag{2-31}$$

where a_{w1i}, b_{w1i} : inclination and intercept of wheel profile before translation and rotation at the i area of wheel (i=Tread or Flange)

and the wheel profile after translation, (x_w, y_w), and rotation, θ, can be expressed as Eq. (2-32).[86]

$$\begin{aligned} y_2 &= a_{w2i} x_2 + b_{w2i} \\ a_{w2i} &= \frac{\sin\theta + a_{w1i}\cos\theta}{\cos\theta - a_{w1i}\sin\theta} \\ b_{w2i} &= \frac{1}{\cos\theta - a_{w1i}\sin\theta}\left[x_w\left(a_{w1i} - a_{w1i}\cos\theta - \sin\theta\right)\right. \\ &\qquad \left. - y_w\left(1 - \cos\theta + a_{w1i}\sin\theta\right) + b_{w1i}\right] \end{aligned} \tag{2-32}$$

where a_{w2i}, b_{w2i} : inclination and intercept of wheel profile after translation and rotation at the i area of wheel (i=Tread or Flange)

From the formula for the distance between one point and one straight line, d_{Rj} can be obtained like

$$d_{Rj} = \frac{\left| a_{w2i} m_{Rj} - n_{Rj} + b_{w2i} \right|}{\sqrt{a_{w2i}^2 + 1}} \tag{2-33}$$

where (m_{Rj}, n_{Rj}): the center of *j*-th circle of rail profile after translation
j=1 when *i*=Flange, *j*=3 when *i*=Tread

2.4.2 Creepage formulation

The relative motion between two bodies that are in contact can be the result of rolling and sliding motion. In the general case of rolling and sliding, the two bodies have different velocity at the contact point and different angular velocity. The relative angular velocity along the normal to the surfaces at the contact point is called *spin.* If the linear velocities at the contact point are not equal, the rolling motion is accompanied by sliding. If the angular velocities are not equal, the motion is accompanied by rolling and/or spin. When rolling occurs without sliding or spin, the motion is considered to be pure rolling. In the case of the contact of two elastic bodies subjected to external applied normal load, some contact points on the contact surface may slip, while other points may stick. The difference between the tangential strains of two bodies in the adhesion area leads to a small slip that is called *creepage*. The creepage is, therefore, due to a combination of elastic deformation and friction.[25] This pheonomenon was recognized by Carter.[16]

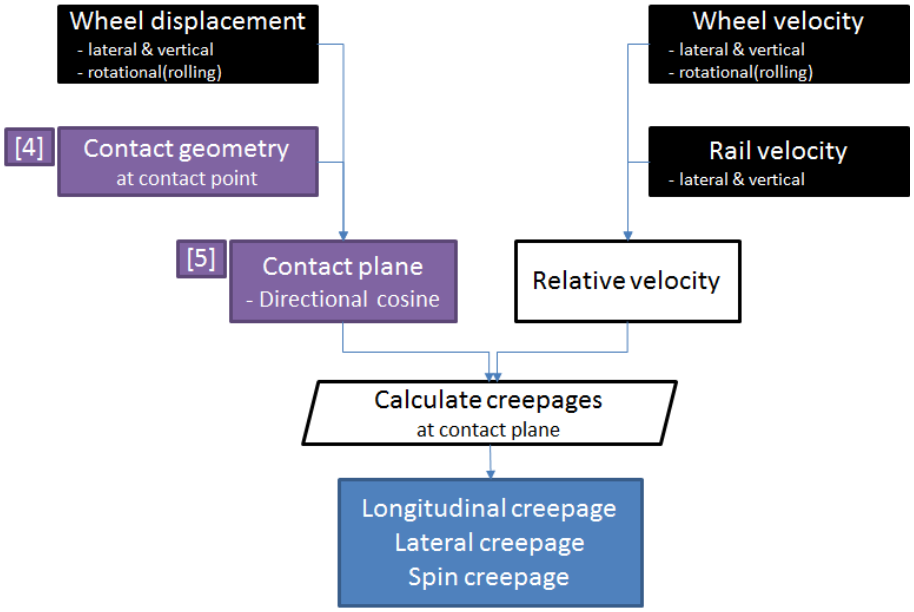

Figure 2.10 Flowchart for calculating creepages

In the case of the wheelset running over the rails, creepage is defined in both the longitudinal and the lateral directions and also about the common normal of the contact patch (spin) as shown in Figure 2.11. The formulation is provided in Garg and Dukkipati[24] as in Eq. (2-34)

$$\begin{aligned} \xi_x &= \left(V_x^w - V_x^r\right)/V \\ \xi_y &= \left(V_y^w - V_y^r\right)/V \quad \text{at contact point} \\ \xi_{sp} &= \left(\omega_z^w - \omega_z^r\right)/V \end{aligned} \tag{2-34}$$

where ξ_x, ξ_y, ξ_{sp} : longitudinal, lateral and spin creepage

V_i^w, V_i^r : i-directional velocity of wheel and rail, respectively ($i = x, y$)

ω_i^w, ω_i^r : z-directional angular velocity of wheel and rail, respectively

V : nominal velocity of train

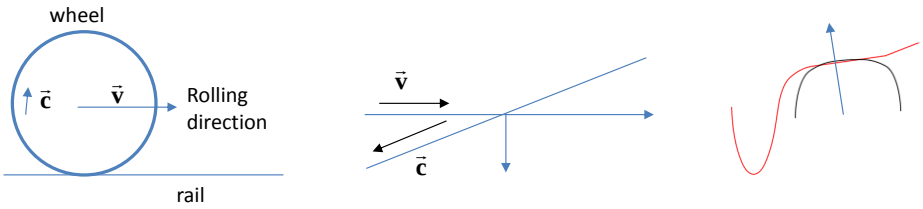

(a) Longitudinal creepage (b) Lateral creepage (c) Spin creepage

Figure 2.11 Definition of creepages[24]

Based on the Eq. (2-34), the right and left creepages which contain rail velocities and fully nonlinear terms without any simplification, can be expressed like Eqs. (2-35) and (2-36)

$$\begin{aligned}
\xi_{xR} &= \left[-\dot{\theta}_w r_{wR} - \dot{\varphi}_w\left(a_{wR}\cos\phi_w + r_{wR}\sin\phi_w\right) + \dot{x}_w\cos\varphi_w\right. \\
&\quad \left. + \sin\varphi_w\left(-\dot{y}_{rR} + \dot{y}_w\right)\right]/V \\
\xi_{yR} &= \left[\dot{\phi}_w\left(-a_{wR}\sin\delta_{rR} + r_{wR}\cos\delta_{rR}\right)\right. \\
&\quad -\sin\left(\phi_w - \delta_{rR}\right)\left\{\dot{z}_{rR} - \dot{z}_w\right\} - \cos\left(\phi_w - \delta_{rR}\right) \\
&\quad \left.\times\left\{\dot{x}_w\sin\varphi_w + \left(\dot{y}_{rR} - \dot{y}_w\right)\cos\varphi_w\right\}\right]/V \\
\xi_{spR} &= \left[\dot{\theta}_w\sin\delta_{rR} + \sin\left(\phi_w - \delta_{rR}\right)\left\{\dot{\theta}_{rR}\cos\varphi_w - \dot{\phi}_{rR}\sin\varphi_w\right\}\right. \\
&\quad \left. + \cos\left(\phi_w - \delta_{rR}\right)\left\{\dot{\varphi}_w - \dot{\varphi}_{rR}\right\}\right]/V
\end{aligned} \tag{2-35}$$

$$\begin{aligned}
\xi_{xL} &= \left[-\dot{\theta}_w r_{wL} + \dot{\varphi}_w\left(a_{wL}\cos\phi_w - r_{wL}\sin\phi_w\right) + \dot{x}_w\cos\varphi_w\right. \\
&\quad \left. + \sin\varphi_w\left(-\dot{y}_{rL} + \dot{y}_w\right)\right]/V \\
\xi_{yL} &= \left[\dot{\phi}_w\left(a_{wL}\sin\delta_{rL} + r_{wL}\cos\delta_{rL}\right)\right. \\
&\quad -\sin\left(\phi_w - \delta_{rL}\right)\left\{\dot{z}_{rL} - \dot{z}_w\right\} - \cos\left(\phi_w - \delta_{rL}\right) \\
&\quad \left.\times\left\{\dot{x}_w\sin\varphi_w + \left(\dot{y}_{rL} - \dot{y}_w\right)\cos\varphi_w\right\}\right]/V \\
\xi_{spL} &= \left[\dot{\theta}_w\sin\delta_{rL} + \sin\left(\phi_w - \delta_{rL}\right)\left\{\dot{\theta}_{rL}\cos\varphi_w - \dot{\phi}_{rL}\sin\varphi_w\right\}\right. \\
&\quad \left. + \cos\left(\phi_w - \delta_{rL}\right)\left\{\dot{\varphi}_w - \dot{\varphi}_{rL}\right\}\right]/V
\end{aligned} \tag{2-36}$$

where x, y, z : translational displacement along longitudinal, lateral and vertical axis, respectively

ϕ, θ, φ : rotational displacement about longitudinal, lateral and vertical axis, respectively

a_w : distance to contact point along the longitudinal wheelset axis from the mass center of wheelset

r_w : rolling radius of wheelset at contact point

δ : inclination of rail seat

V : nominal velocity of train

subscripts R and L : right and left, respectively

subscripts w and r : wheel and rail, respectively

2.4.3 Calculation of creep force and contact force

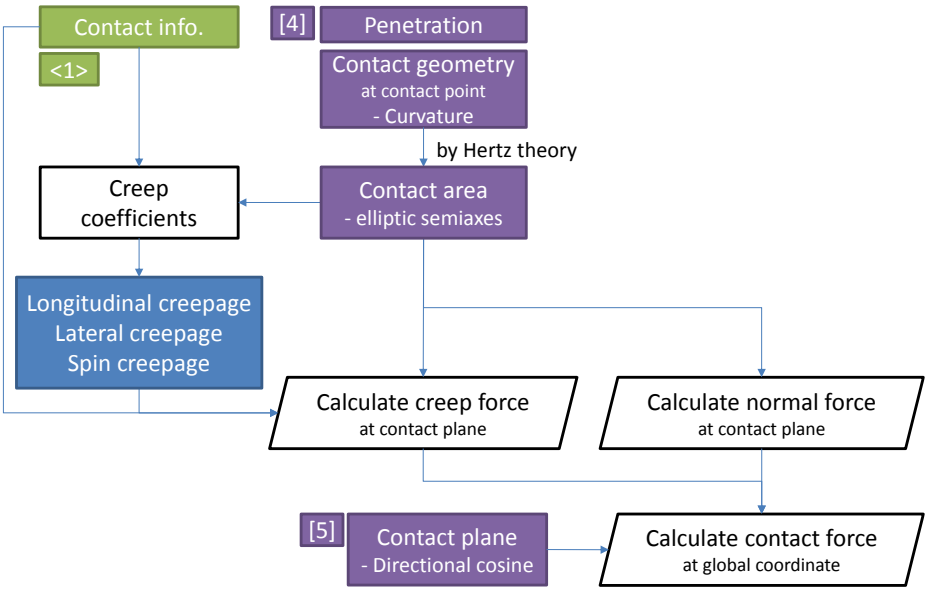

Figure 2.12 Flowchart for calculating creep force and contact force

For the wheel/rail contact problem, Hertz theory[15] is the most commonly used theory to determine the shape of the contact area and the normal contact force which is defined as Eq. (2-37).

$$F_n = K_h \delta^{3/2} \tag{2-37}$$

where F_n: normal contact force

K_h: Hertzian contact spring coefficient

δ : penetration depth between wheel and rail

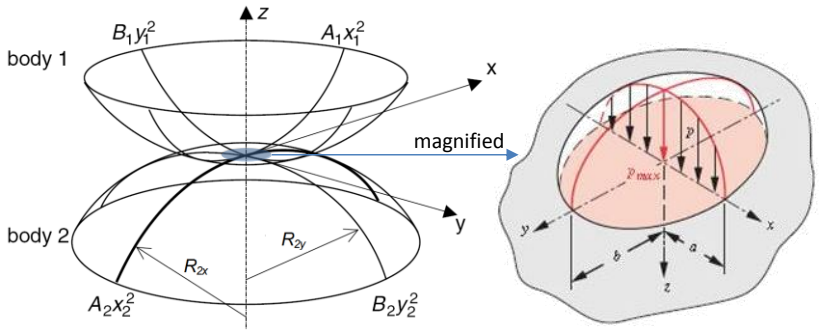

Figure 2.13 Definition of Hertz contact problem

On the other hand, several creep force theories have been developed and applied to solve the wheel/rail contact problem, such as Carter's theory[16], Vermeulen and Johnson's theory[17], Heuristic nonlinear creep force model[24], Polach's nonlinear creep force model[23], Kalker's linear theory, simplified theory and exact theory[21], and so on. Kalker's simplified theory is widely used in the world for the accuracy and efficiency of calculation. Its source code, FASTSIM, is open to public in his paper and applied to calculate the creep force in this study.

The analytical solution based on the simplified theory can be obtained when the effect of spin moment is ignored. In this program the contact surface is discretized into several strips, and the creep forces are calculated by incrementing the tangential tractions from on strip to another. The complete algorithm of FASTSIM can be found in Kalker.[22]

Normal force calculated from Hertzian contact theory, and creep forces calculated from FASTSIM, are defined in the plane of contact patch, and have to be rotated and integrated into the global coordinate, finally expressed as contact forces(longitudinal, lateral and vertical wheel load).

2.5 Wind application

In order to simulate the wind load to bridge and train, first of all, the wind history has to be generated in any way. The random characteristics of wind are usually defined as the mean wind velocity, wind spectrum, turbulence length, turbulence intensity, coherence function and so on. In this section, such parameters are determined to meet the in-situ condition of the target bridge. Since the aeroelasticity is an important factor to bridge response, an efficient way to reflect it into the MSM is introduced. Then the wind load on train is calculated by means of aerodynamic.

2.5.1 Simulation of wind load on bridges

Basic procedure to simulate the wind load on bridge is introduced by Lee.[87, 88] The Von Karman spectrum in Eq. (2-38) is used to simulate a fluctuating wind velocity to reproduce the properties of real wind. (Strømmen[65])

$$\begin{aligned}
\frac{nS_u}{\sigma_u^2} &= \frac{4n_u}{\left(1+70.8n_u^2\right)^{5/6}} \\
\frac{nS_v}{\sigma_v^2} &= \frac{4n_v\left(1+755.2n_v^2\right)}{\left(1+283.2n_v^2\right)^{11/6}} \\
\frac{nS_w}{\sigma_w^2} &= \frac{4n_w\left(1+755.2n_w^2\right)}{\left(1+283.2n_w^2\right)^{11/6}}
\end{aligned} \tag{2-38}$$

where nS_i / σ_i^2 : normalized spectrum (i=u, v, w for longitudinal, lateral and vertical direction, respectively)

n : frequency

σ_i^2 : variance of each component (i=u, v, w)

n_i : normalized frequency of each component (n_i=nL_i/U, i=u, v, w)

U : mean wind velocity along u-direction

L_i : length scales of each component (i=u, v, w)

For the parametric study for various circumstances of fluctuating wind, the mean wind velocity, U, is assumed be six cases, that is U=5, 10, 15, 20, 25 and 30m/s in addition to no-wind condition (U=0). By applying the equation of Strømmen for turbulence length, L_u=157.71(m), L_v=39.43(m) and L_w=13.14(m) is determined in the middle of the Yeongjong Bridge. The turbulence intensity is presented in Design Guidelines for Steel Cable-Supported Bridges (KSCE[89]) that gives the values, I_u=11.88%, I_v=9.50% and I_w=5.94% for this study. In order to consider the spatial correlation of wind velocity, the coherence function is used like Eq. (2-39).

$$\sqrt{\mathrm{coh}(\eta : n)} = \exp\left(-\frac{k_\eta n \eta}{U} \right) \tag{2-39}$$

where n : frequency

η : distance between two points

U : mean wind velocity along u-direction

$k_\eta = 14(\eta / z)^{0.45}$: horizontal coefficient

z : height of each point

To take the uncertainty of the fluctuating wind velocity into account, five wind seeds are generated in this study. (Figure 2.14)

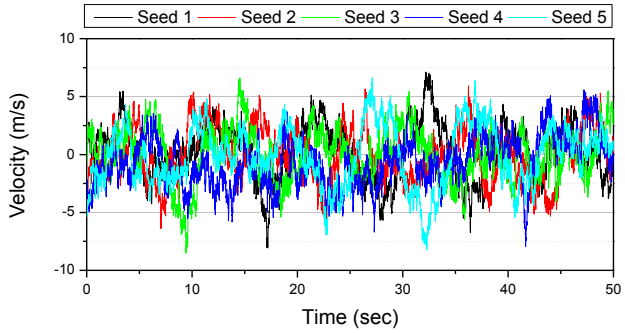

(a) *u*-directional fluctuating wind velocity

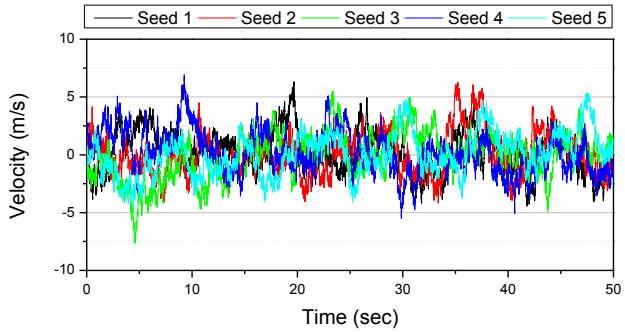

(b) *v*-directional fluctuating wind velocity

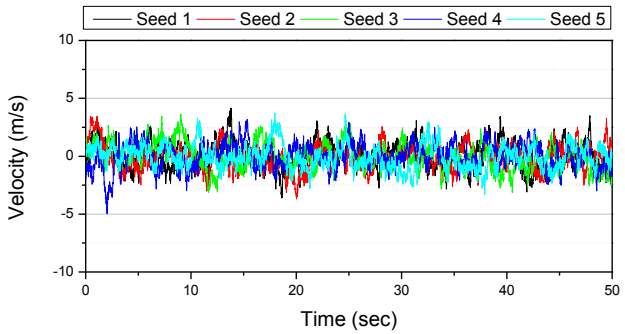

(c) *w*-directional fluctuating wind velocity

Figure 2.14 Simulation result of fluctuating wind velocity

2.5.2 Calculation of wind load on train by aerodynamic coefficients

Fluctuating wind velocity that vibrate the bridge, can give train a kind of loads, such as forces and moments. The relation between resultant wind velocity and force on the train is expressed as Eq. (2-40)[69] and Figure 2.15.

$$\begin{aligned} F_x(\beta) &= C_D(\beta) q h_T w_T \\ F_y(\beta) &= C_S(\beta) q h_T l_T \\ F_z(\beta) &= C_L(\beta) q w_T l_T \\ M_x(\beta) &= C_R(\beta) q h_T^2 l_T \\ M_y(\beta) &= C_P(\beta) q w_T l_T^2 \\ M_z(\beta) &= C_Y(\beta) q h_T l_T^2 \end{aligned} \tag{2-40}$$

where F_x, F_y, F_z : drag, side, lift force on carbody (N)

M_x, M_y, M_z : rolling, pitching, yawing moment on carbody (N·m)

C_D, C_S, C_L : drag, side, lift force coefficient (-)

C_R, C_P, C_Y : rolling, pitching, yawing moment on carbody (N·m)

β : incidence angle (rad)

q : dynamic head pressure (N/m^2), $q = \rho\left(V^2/2\right)$

h_T, w_T, l_T : height, width, and length of carbody (m)

ρ : density of air (ρ =1.275kg/m^3)

V : resultant wind speed (m/s), $V = \sqrt{V_W^2 + V_T^2}$

V_W : wind velocity along lateral direction (m/s)

V_T : train velocity along longitudinal direction (m/s)

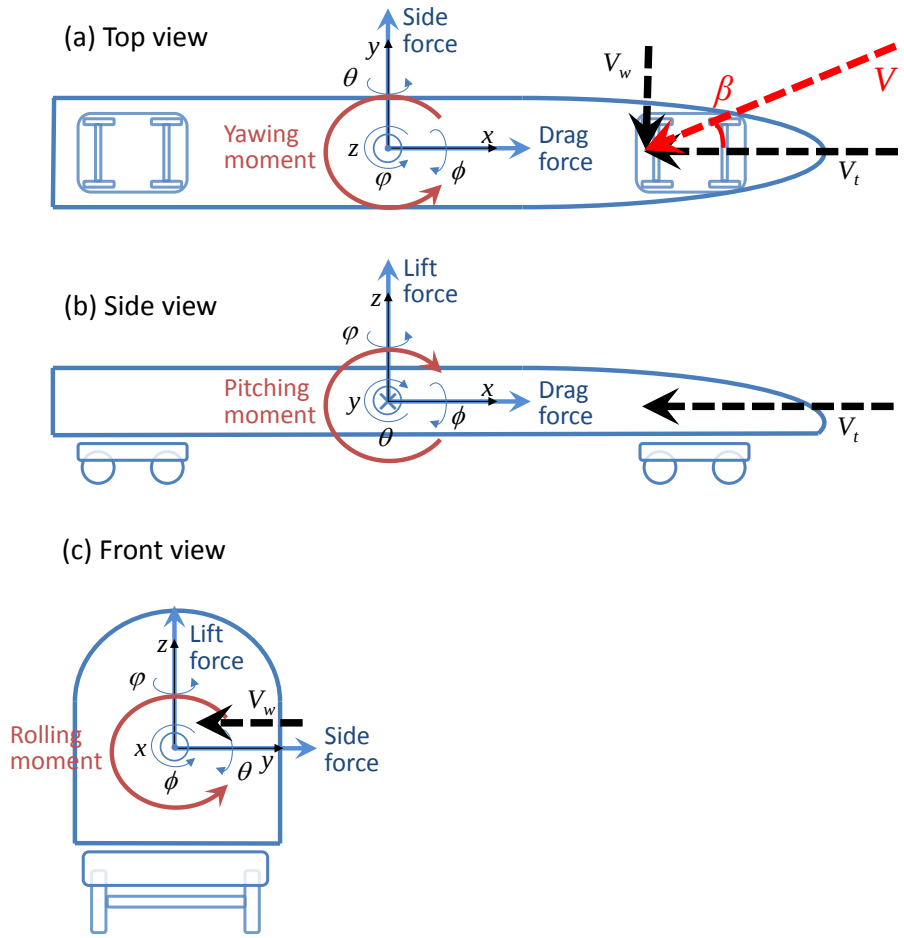

Figure 2.15 Definition of wind load on train

Because the train speed is assumed to be constant, the effect of drag force can be neglected, and the other five loads are applied on the train body. As written already, a lot of analyses and experiments[68-73] had performed for acquiring the aerodynamic coefficients. (C_D, C_S, C_L, C_R, C_P, C_Y) The results of aerodynamic coefficients according to the incidence angle (β) are recalculated by means of Eq. (2-40) and summarized in the Figure 2.16.

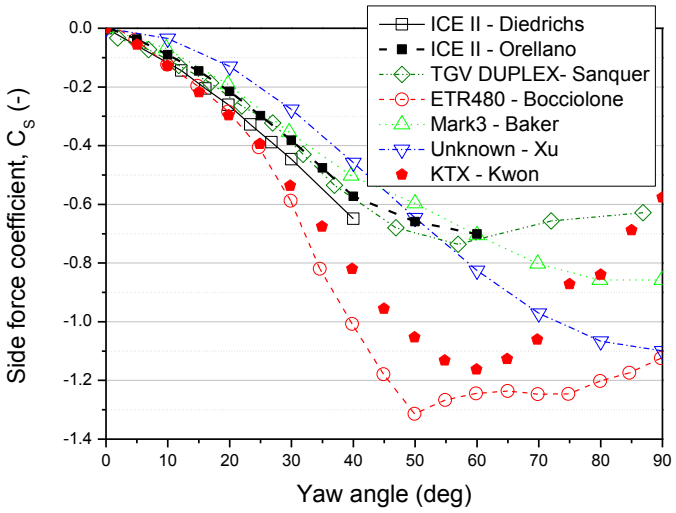

(a) Side force coefficient

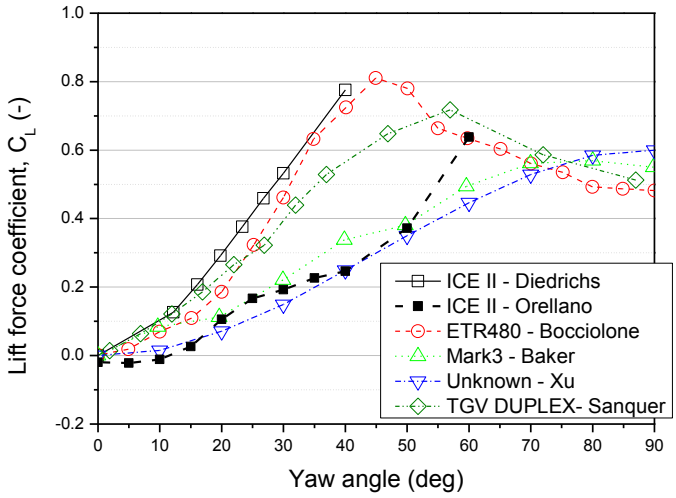

(b) Lift force coefficient

Figure 2.16 Aerodynamic coefficients

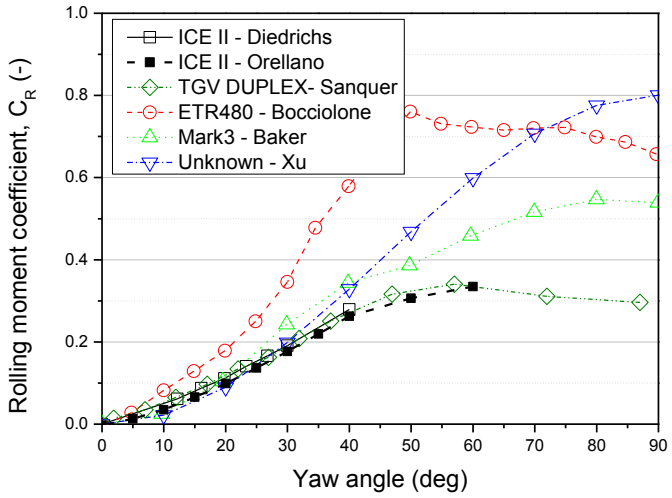

(c) Rolling moment coefficient

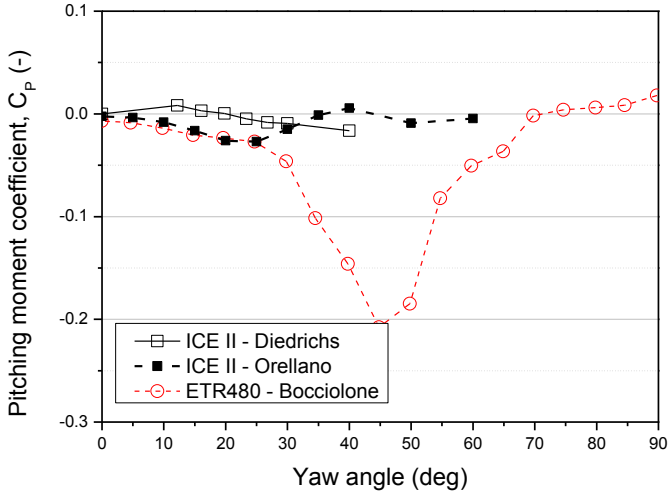

(d) Pitching moment coefficient

Figure 2.16 Aerodynamic coefficients (continued)

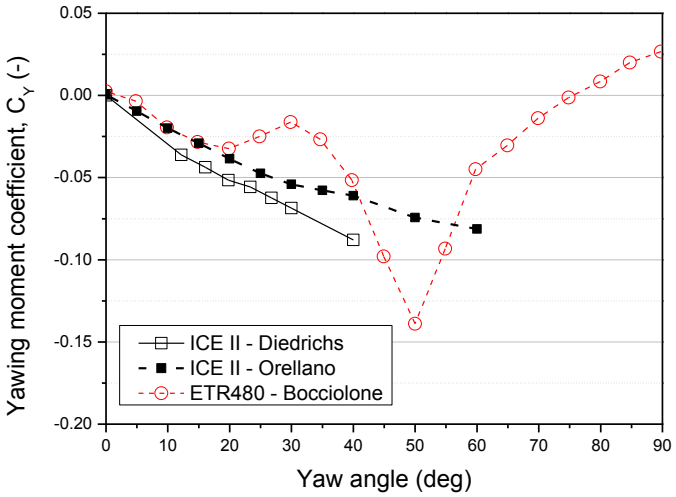

(e) Yawing moment coefficient

Figure 2.16 Aerodynamic coefficients (continued)

Especially Diedrichs[69] and Orellano[70] derived the aerodynamic coefficients for ICE II, and Kwon[73] for KTX by the Computational Fluid Dynamics (CFD) analysis and the wind tunnel test for scaled models. There are not enough test results for KTX that include the six components of aerodynamic coefficients and wide range of incidence angle. The other result that can reflect the aerodynamic characteristics of high speed train has to replace it, therefore the result of Orellano[70] is chosen as an appropriate candidate.

2.6 Iterative procedure and time-stepping method

The iterative procedure is necessary to reflect the nonlinear property of Hertzian contact force and creep force between wheel and rail. The calculated contact forces are applied to the two subsystems by the law of action and reaction, and determine the displacements of train or track, which are used for checking the convergence of iteration. The overall flowchart of this framework is shown in Figure 2.17, and the Newton-Raphson method[59] is applied in this iteration.

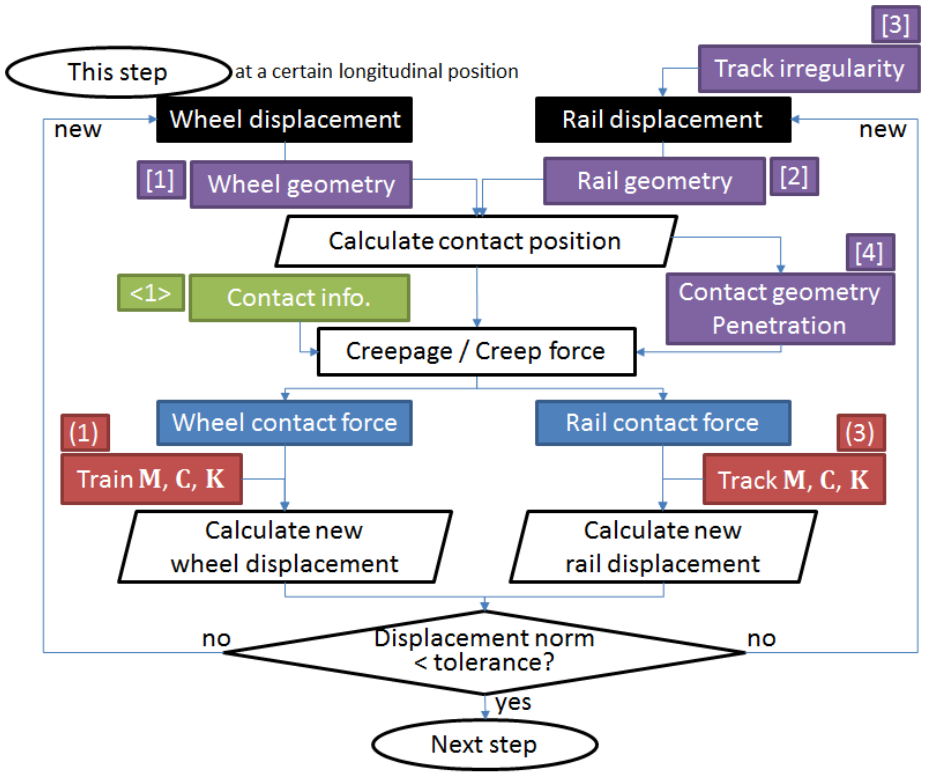

Figure 2.17 The detailed flowchart of overall scheme

Because the displacement norm has to be small enough to converge the contact forces, the sensitivity of wheel/rail contact has to be considered. When the Hertzian contact is linearized as a spring constant, the stiffness is about 2.7×10^{9}(N/m). If the penetration depth between wheel and rail changes 1μm, then the normal contact force changes up to 2.7kN. Therefore the 2nd displacement norm has to be extremely small like 5×10^{-9}(m) or less to guarantee the convergence of force.

Among the solutions for the time-stepping, Newmark method (Chopra[59]) is one of the most popular solutions in the structural dynamics. It assumes the displacement and velocity at the time step of $t+\triangle t$ in Eq. (2-41) and applies them to the equations of motion.

$$\begin{aligned}\dot{\mathbf{U}}_{t+\Delta t} &= \dot{\mathbf{U}}_t + \left[(1-\gamma)\Delta t\right]\ddot{\mathbf{U}}_t + (\gamma\Delta t)\ddot{\mathbf{U}}_{t+\Delta t} \\ \mathbf{U}_{t+\Delta t} &= \mathbf{U}_t + (\Delta t)\dot{\mathbf{U}}_t + \left[(0.5-\beta)(\Delta t)^2\right]\ddot{\mathbf{U}}_t + \left[\beta(\Delta t)^2\right]\ddot{\mathbf{U}}_{t+\Delta t}\end{aligned} \tag{2-41}$$

where $\mathbf{U}_t$, $\mathbf{U}_{t+\triangle t}$: displacement vector at t or $t+\triangle t$

$\dot{\mathbf{U}} = d\mathbf{U}/dt$, $\ddot{\mathbf{U}} = d^2\mathbf{U}/dt^2$

t : time

$\triangle t$: time step

β , γ : the coefficients of Newmark method

However, the Newmark method can consider numerical damping (or algorithmic damping) only by reducing the accuracy. The numerical damping indicates the arbitrary decrease of the cumulative round-off error, truncation

error, and so on in the numerical analysis. As a supplementation for this drawback of Newmark method, Hilber, Hughes and Taylor[90] proposed an α –method (HHT-α method) which introduced α variable to maintain the 2nd order accuracy and simultaneously consider the numerical damping. This method uses the same assumptions of Newmark family and applies the equations of motion like Eq. (2-42) using the coefficient, α.

$$\begin{aligned}[\mathbf{M}]\ddot{\mathbf{U}}_{t+\Delta t}+(1+\alpha)[\mathbf{C}]\dot{\mathbf{U}}_{t+\Delta t}-\alpha[\mathbf{C}]\mathbf{U}_t+(1+\alpha)[\mathbf{K}]\mathbf{U}_{t+\Delta t}\\ -(1+\alpha)[\mathbf{K}]\mathbf{U}_{t+\Delta t}=(1+\alpha)\mathbf{P}_{t+\Delta t}-\alpha\mathbf{P}_t\end{aligned} \tag{2-42}$$

The response at $t+\triangle t$ can be acquired by substituting Eq. (2-41) into Eq. (2-42)

$$[\hat{\mathbf{K}}]\ \ddot{\mathbf{U}}_{t+\Delta t}=\hat{\mathbf{P}}_t \tag{2-43}$$

where $[\hat{\mathbf{K}}]=[\mathbf{M}]+(1+\alpha)\gamma(\Delta t)[\mathbf{C}]+(1+\alpha)\beta(\Delta t)^2[\mathbf{K}]$

$$\begin{aligned}\hat{\mathbf{P}}_t=&(1+\alpha)\mathbf{P}_{t+\Delta t}-\alpha\mathbf{P}_t-(1+\alpha)(1-\gamma)(\Delta t)[\mathbf{C}]\\ &+(1+\alpha)(1-\beta)(\Delta t)^2[\mathbf{K}]\ddot{\mathbf{U}}_t-[\mathbf{C}]+(1+\alpha)(\Delta t)[\mathbf{K}]\dot{\mathbf{U}}_t-[\mathbf{K}]\mathbf{U}_t\end{aligned}$$

In this equation, if $-1/3\le\alpha\le 0,\ \beta=(1-\alpha)^2/4$ and $\gamma=(1-2\alpha)/2$ then HHT-α method is known to be implicitly and unconditionally stable and maintain the 2nd order accuracy.

The time step has to be sufficiently small for solving convergence problem with little error at each step, and simultaneously not too small for the total analysis time to be reduced. The train/track interaction program for only

vertical direction uses the time step of hundreds of micro second which is determined to record the responses of train and track over 50 times between two adjacent sleepers. (Yang[91]) The 3D interaction program, however, has to deal with not only the vertical force but also the lateral force, thus it is more sensitive than 2D program. Consequently the time step of 3D should be much less than that of 2D.

Moreover, when we consider the linearized Hertzian contact spring (2.7×10^{9}(N/m)) and wheelset mass (2.048ton), the natural frequency of wheelset is about 1,148(Hz). A time step is usually chosen based on the smallest vibration period of the interesting body divided by 8~10.[92, 93] Therefore the time step has to be smaller than 8.3×10^{-5}(sec) and is determined to be 2×10^{-5}(sec) in this study in order to satisfy the convergence criterion of displacement norm, 5×10^{-9}(m). The followings are the representative papers which used the time step similar to that of this study.

- W. M. Zhai (2009)[94] : 10×10^{-5}(sec)
- X. Xiao (2011)[95] : 7.2×10^{-6}(sec)
- H. Chollet (2013)[96] : 1.5×10^{-3}(sec, nominal) ~ 0.11×10^{-6}(sec, minimal)

Chapter 3 Verification of the proposed framework

3.1 Overview of verification procedure

Because there is no comparable target program to integrate all the interactions discussed above, the verification of the suggested framework is performed individually in three major parts. The first part is the verification of 3D analysis of wheel/rail interface which includes finding the contact points and calculating the creepages and contact forces. The second is track/bridge interaction part that checks the appropriate result by mode superposition method as suggested before. The last one deals the wind/bridge interaction which includes the aero-elastic deformation of bridge.

3.2 Verification of train/track interaction

3.2.1 Train model and track cases

As explained in section 2.1, the train/track interaction is set with the following sequence.

- Find the contact position between wheel and rail.
- Calculate the creepages using the geometry information and relative velocity of wheel and rail at contact point.
- Compute the normal force from the penetration depth based on the Hertzian contact theory.

- Calculate the tangential creep forces according to FASTSIM algorithm.
- Determine the contact forces by rotating the normal force and creep forces to be fitted to global coordinate.
- Apply the contact force to train system and track system individually and reciprocally.

In 1999, Manchester benchmark project[97] was executed to compare and verify the analysis results of various commercial packages. The main purpose of this project was to present the simulation results of vehicle dynamics to the people who design and research the suspension of train, and to determine the compatibility of them. The major commercial packages at that decade were participated in this project, such as VAMPIRE, GENSYS, SIMPACK, ADAMS-Rail (VI-Rail) and NUCARS. It dealt with four different track types as following table.

Table 3.1 Track cases of Manchester benchmark

Cases	Model	Purpose	Figure 3.1
Case 1	Curve	Quasi-static curving	-
Case 2	Lateral shift	Stability prediction	(a)
Case 3	Lateral periodic irregularity	Lateral interaction	(b)
Case 4	Vertical periodic irregularity	Vertical interaction	(c)

Currently because this study does not includes the analysis of the curved section, it is desired to perform a comparison of the results relating to the remaining three cases (Case 2, 3, 4). The target of Case 2 is to predict the

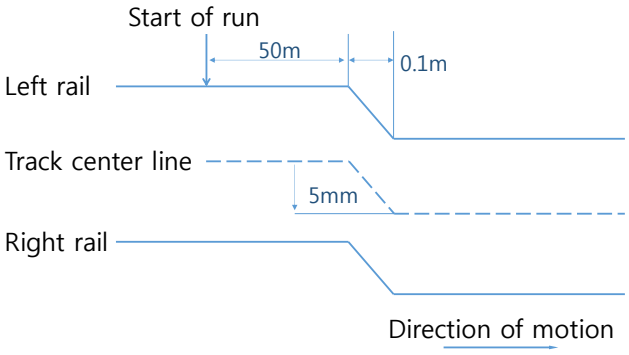

(a) Lateral shift (plan view)

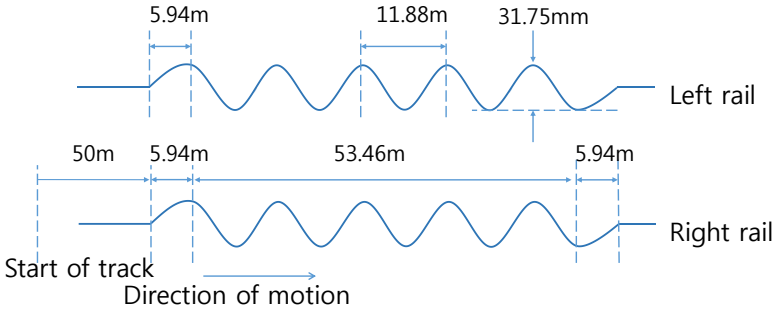

(b) Lateral harmonic irregularity (plan view)

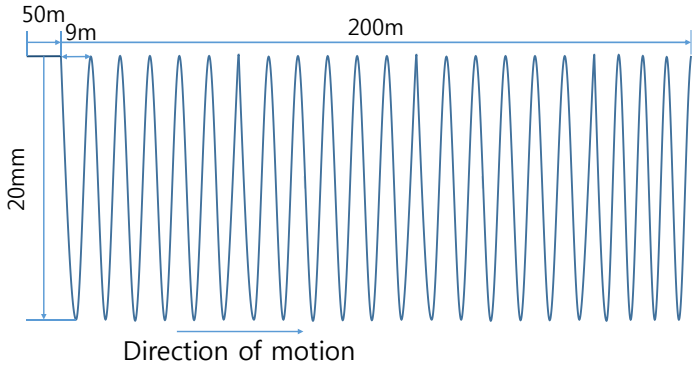

(c) Vertical harmonic irregularity (side view)

Figure 3.1 Track irregularity of Manchester benchmark

stability and characteristics in behavior of vehicle suspension according to the lateral force exerted from the instant lateral shift of track irregularity. The shape of track irregularity is so simple that it is easy to compare the result of wheel/rail contact, such as the contact geometry of wheel and rail at the contact point and creepages. Case 3 and Case 4 is intended to compare the lateral/vertical interaction, respectively, due to the periodic track irregularity in Figure 3.1(b) and (c). Therefore, mainly presented are the results of lateral contact forces in Case 3 and that of vertical forces in Case 4.

3.2.2 Assumptions for simplified train and track

The Manchester project presented two different vehicle models, one is the passenger car with one carbody, two bogies and four wheelsets, and the other is the freight car with one carbody and two wheelsets. Since it is evident that the more accurate comparison is possible when using the simpler vehicle structure, only freight car is used in this study, instead of the passenger car with more complex structures and nonlinear suspensions and dampers. Moreover, the frictional damper included in the freight vehicle of the Manchester benchmarking, is excluded for the simplification.

The actual wheel profile (S1002) used in the Manchester project is replaced by the flat profile like Figure 3.3 for the same purpose. Such assumptions of simplification are thought to be helpful for comparing exactly the results of Manchester and that of this study.

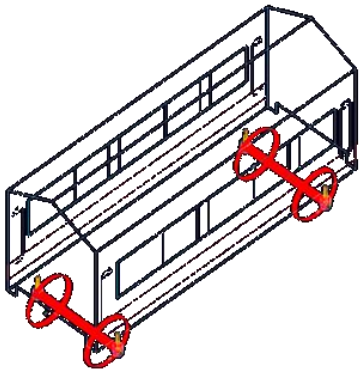

Figure 3.2 Train model in Manchester benchmark

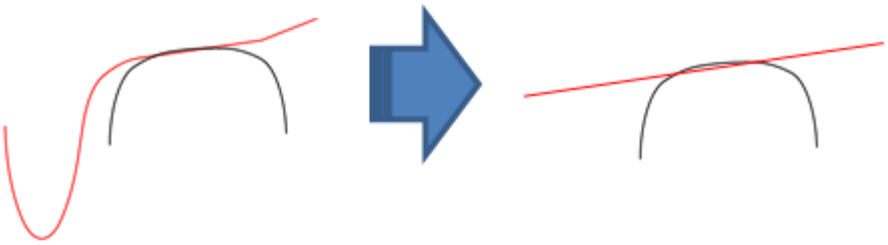

Figure 3.3 Simplification of wheel profile (original to flat)

The commercial package that is available for verification is “VI-Rail”[98] which was called “ADAMS-Rail” at the time of project execution. The embedded model for the freight car is modified to exclude the friction damper and have the flat profile. This study makes the same model by using the same dimension and properties, and the results are compares to that of Manchester. The rail is assumed to be rigid and fixed for eliminating the effect of track movement.

3.2.3 Comparative result with Manchester benchmark

(1) Case 2 - Lateral shift (5mm movement)

Most of all, Case 2 can give comparison of various contact phenomena between wheel and rail. The first change by the contact of wheel and rail is the relative displacement of the two objects. As there is the lateral shift of 5mm along the longitudinal 10cm's track, the vehicle undergo the change of wheel contact point in a moment while driving. Figure 3.4 (a) and (b) shows the result of the contact position of the wheel relative to the center of the rail, it is seen that the larger displacement occurs at the first axle than the second axle, and the results of VI-Rail and this study give almost perfect match in the contact position.

Once the location of the contact point is determined, the creepages can be calculated after extracting the exact geometric information of wheel and rail at the contact point. The representative information is the rolling radius of wheel, which is shown in Figure 3.4 (c) and (d). These results have the same tendency as the lateral movement that the first wheelset changes more than the second one, and also show a good agreement with each other.

In the next step, the creepages that are calculated from the relative velocities and the geometry information, are shown in Figure 3.5 for longitudinal, lateral and spin creepage respectively. Whereas longitudinal creepage and lateral creepage give the matching results, the spin creepage shows the same pattern but the slight difference in the value itself. Given that the inputs (the relative velocities and geometry information) are same, the creepages must be equally

computed. But the gap in spin creepage is predicted to be the difference of creepage equations applied in the two programs.

Since the expressions for creepages are very complex, some packages used to simplify such expression ignoring nonlinear terms in them. But this study contains all terms in Eqs. (2-38) and (2-39) to calculate the creepages more precisely, which is thought to be better results than that of VI-Rail. And the gap is about the order of $10^{-4}m^{-1}$ which is so trivial as to give little effect on the contact force afterward.

Therefore, all results about the contact position of wheel and rail, the geometric information at contact point and the creepage calculated from them according to the lateral shift of the track, confirm that this study substantially yields a good agreement with VI-Rail for the wheel/rail contact problem.

(2) Case 3 - Lateral irregularity (harmonic)

Case 3 simulates and analyzes the lateral track irregularity of periodic sinusoidal wave. While case 2 attempted to verify the contact phenomena of wheel and rail, Case 3 tries to verify the following forces;

- the normal force calculated from the Hertzian contact theory
- the creep forces generated by applying the FASTSIM from the normal force and creepages as input
- the lateral wheel loads by converting the local forces into global coordinate

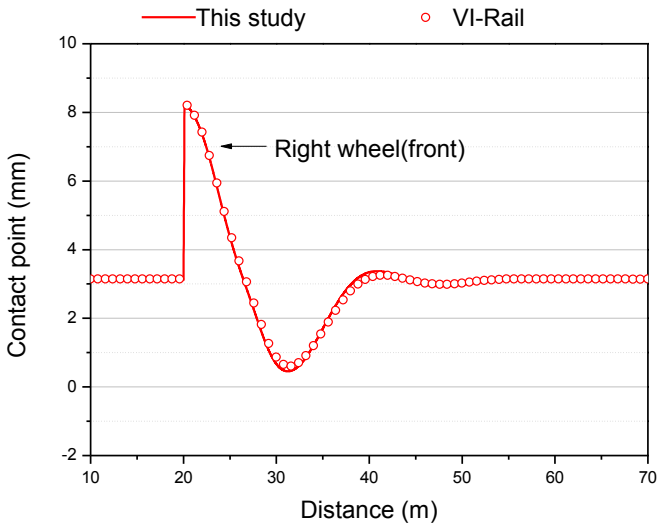

(a) Wheel contact point : front-right wheel

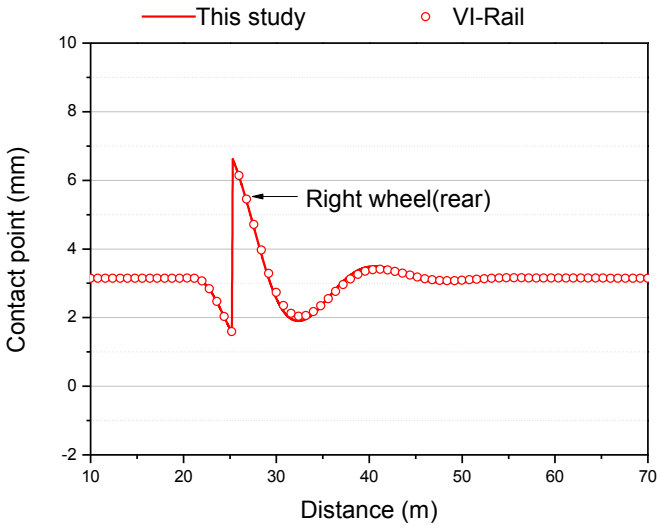

(b) Wheel contact point : rear-right wheel

Figure 3.4 Comparison of contact geometry : Case 2

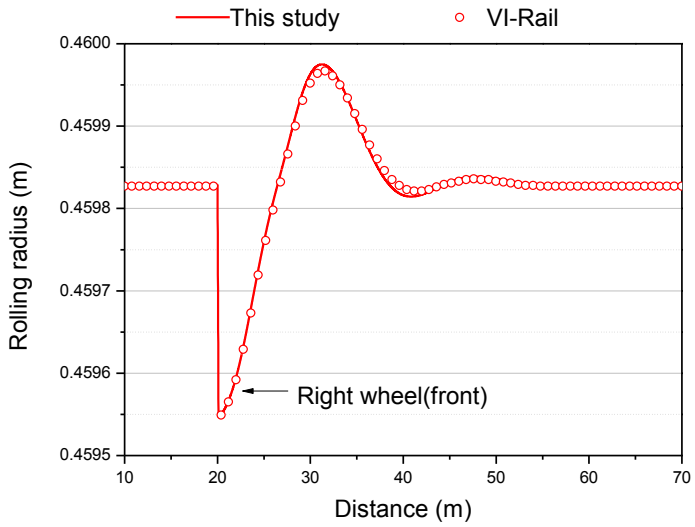

(c) Rolling radius at contact point : front-right wheel

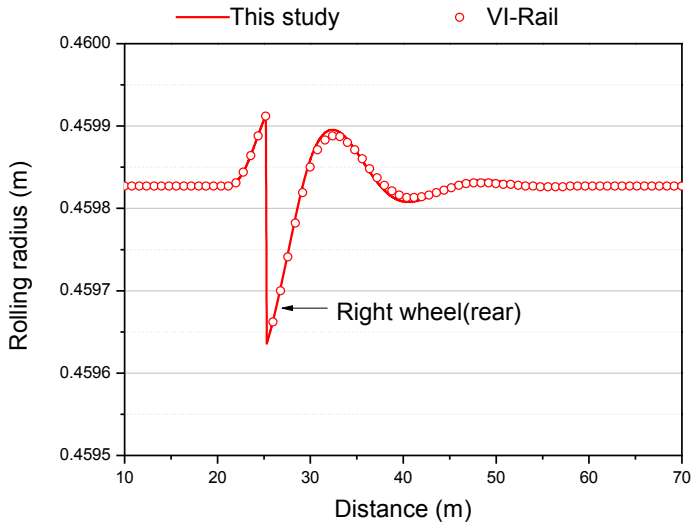

(d) Rolling radius at contact point : rear-right wheel

Figure 3.4 Comparison of contact geometry : Case 2 (continued)

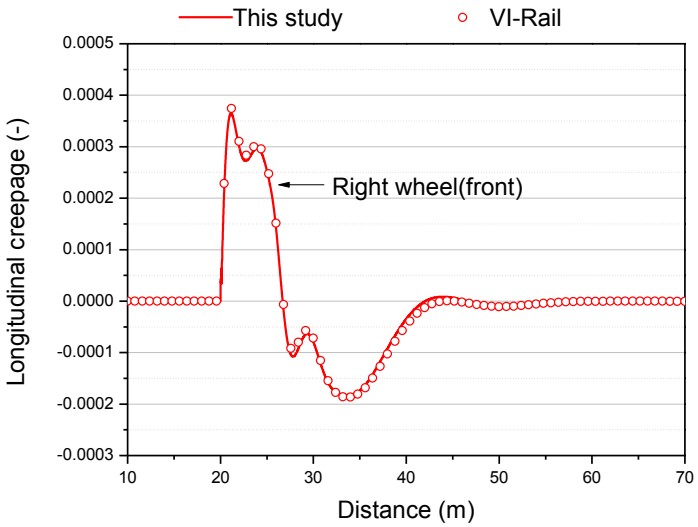

(a) Longitudinal creepage : front-right wheel

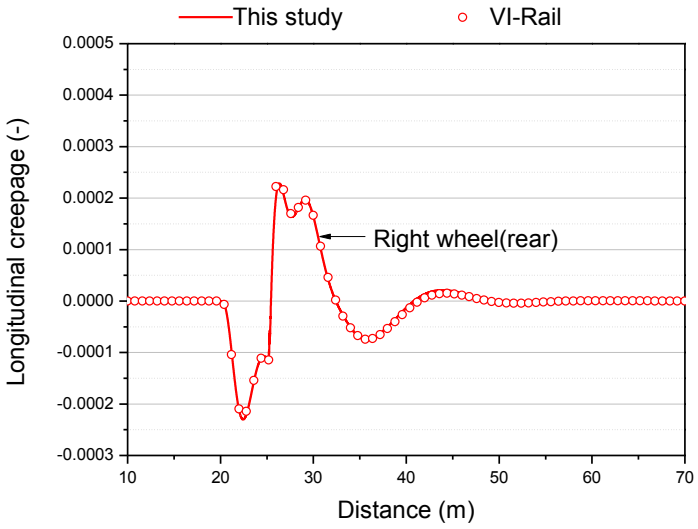

(b) Longitudinal creepage : rear-right wheel

Figure 3.5 Comparison of creepage : Case 2

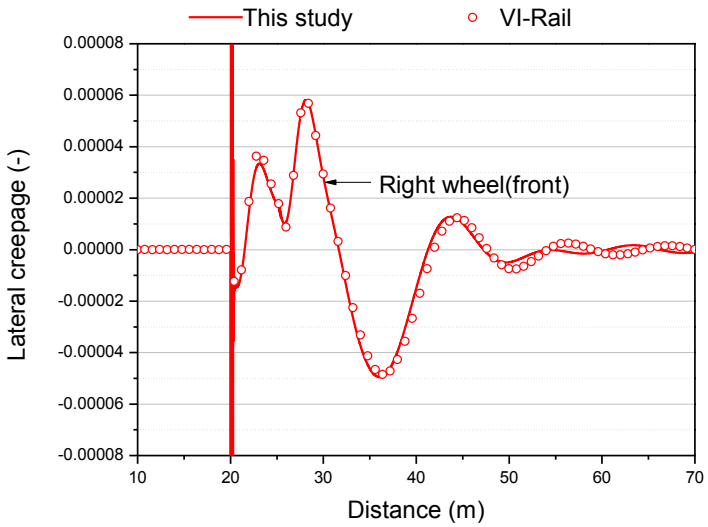

(a) Lateral creepage : front-right wheel

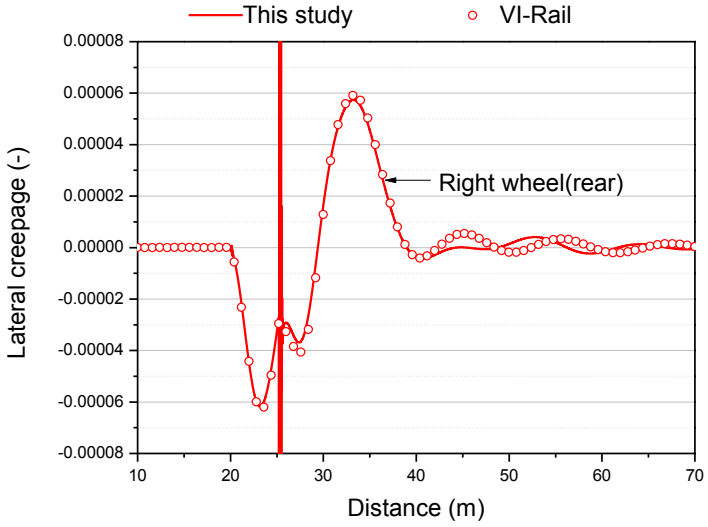

(b) Lateral creepage : rear-right wheel

Figure 3.5 Comparison of creepage : Case 2 (continued)

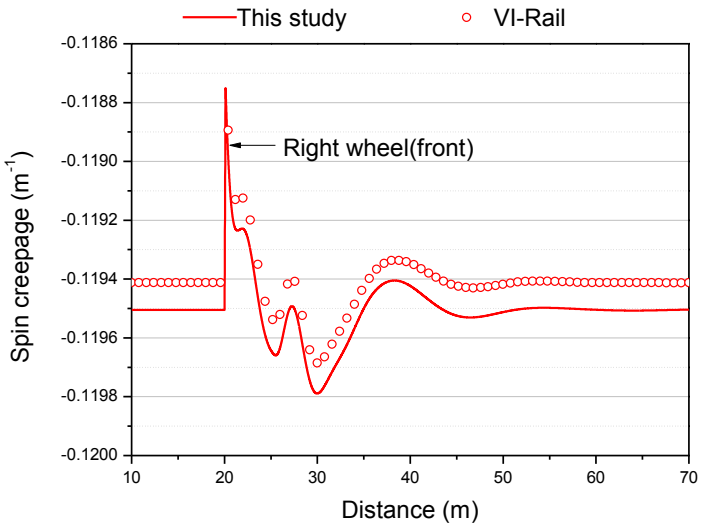

(a) Spin creepage : front-right wheel

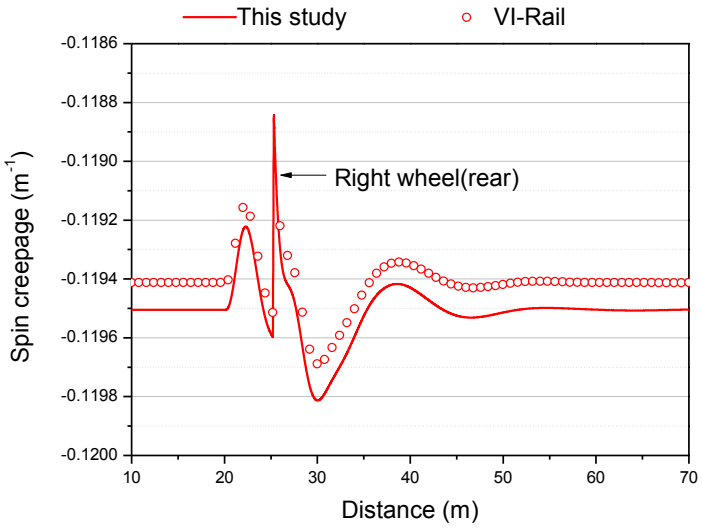

(b) Spin creepage : rear-right wheel

Figure 3.5 Comparison of creepage : Case 2 (continued)

Figure 3.6 deals with the comparison of normal force which is perpendicular to the contact plane and dependent on the penetration depth as a result of wheel/ rail contact, and Figure 3.7 shows the creep forces which is divided into longitudinal and lateral direction separately. Although the value of the normal force on the first axle is almost equal to that of VI-Rail, the second axle seems to vary slightly in the maximum peak value. This phenomenon appears to be similar in the longitudinal creep force and the lateral creep force. The variation is thought to be induced by the dissimilarity in modeling the geometry links of suspension elements, and by the subtle differences of calculating method for normal forces, compared to VI-Rail. Although the peak values show slight differences, the overall variation trend and vibration period are consistent and attenuation characteristics seems to be similar.

The three components – the normal force and two creep forces – which are formed in the contact plane, will be translated rotationally to calculate the wheel load in global coordinate, as Figure 3.8. Like the slight difference but the consistent tendency in creep forces, the same patterns occur in global contact forces because they are the output from the previous three force components, but the result of this study has a good accuracy enough to analyze the overall behavior of train, and the lateral displacement, vertical displacement and yawing angle which are less sensitive than forces, show almost matching to VI-Rail. (Figure 3.9)

Through the analysis of Case 3, the lateral response of running train under the consideration of wheel/rail contact is verified.

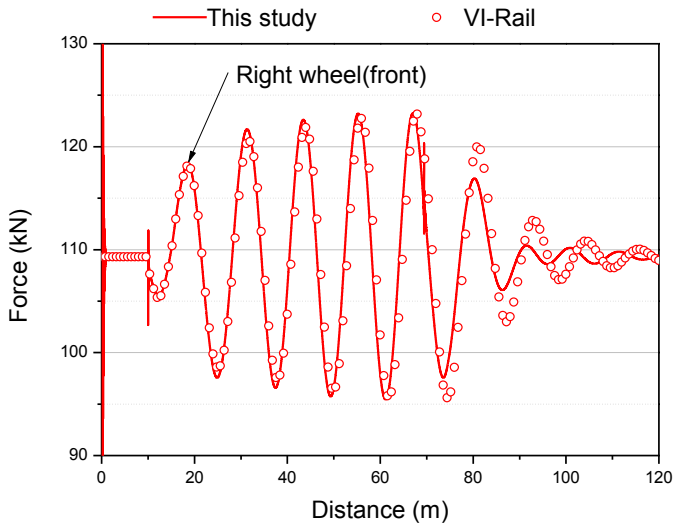

(a) Front-right wheel

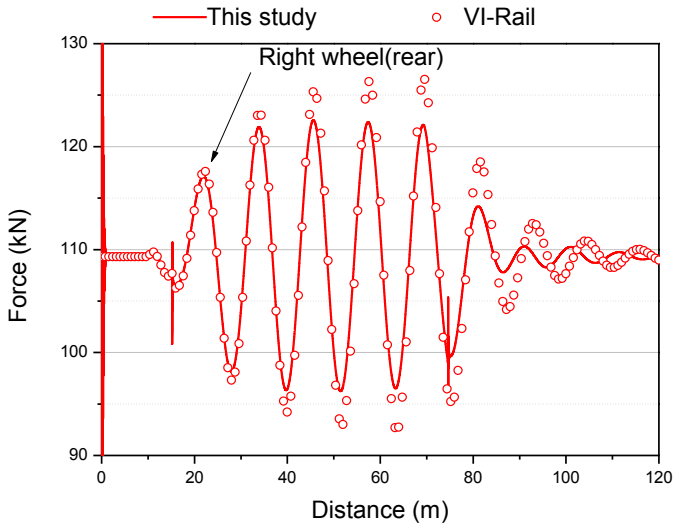

(b) Rear-right wheelset

Figure 3.6 Comparison of normal force : Case 3

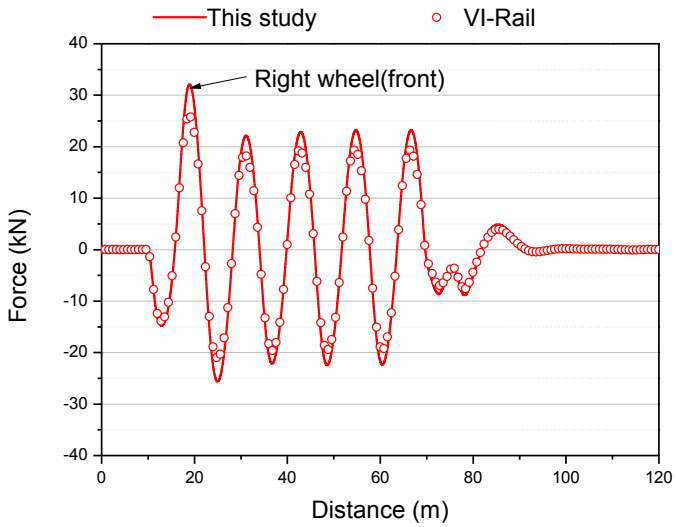

(a) Longitudinal creep force : front-right wheel

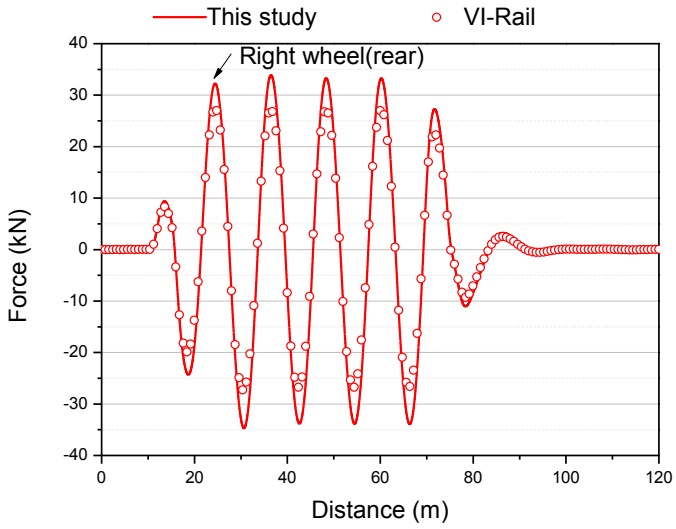

(b) Longitudinal creep force : rear-right wheel

Figure 3.7 Comparison of creep force : Case 3

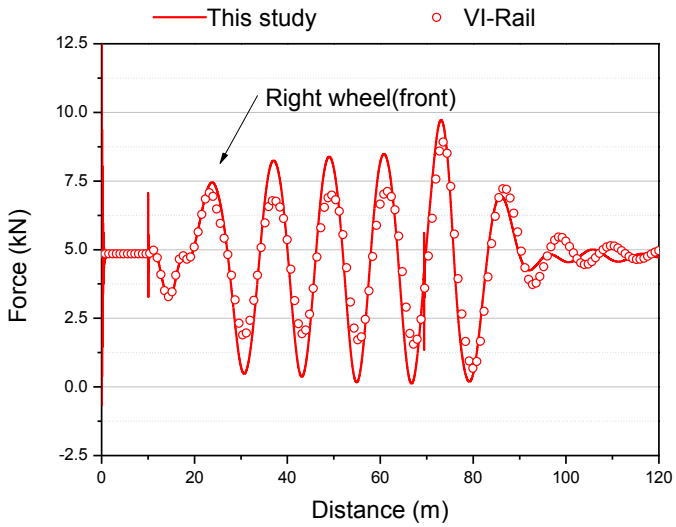

(a) Lateral creep force : front-right wheel

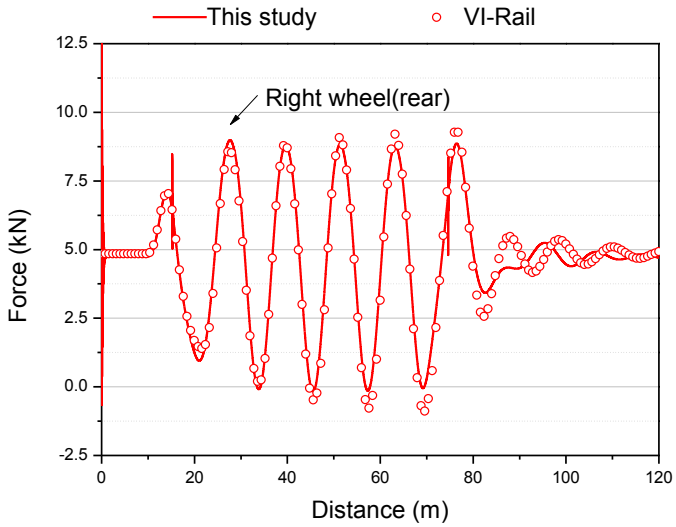

(b) Lateral creep force : rear-right wheel

Figure 3.7 Comparison of creep force : Case 3 (continued)

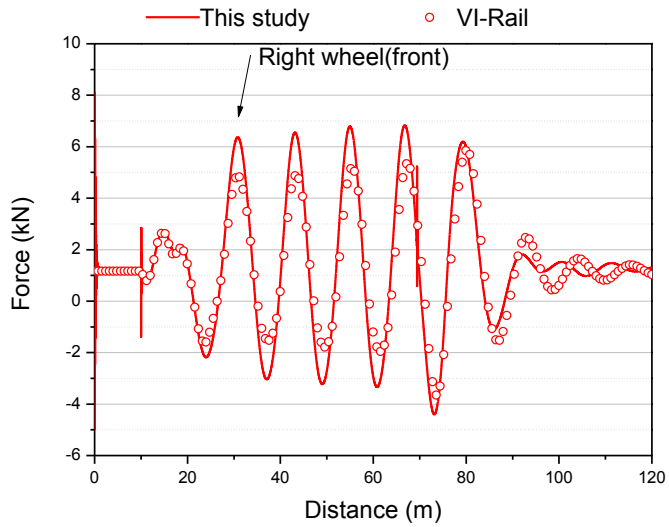

(a) Lateral wheel load : front-right wheel

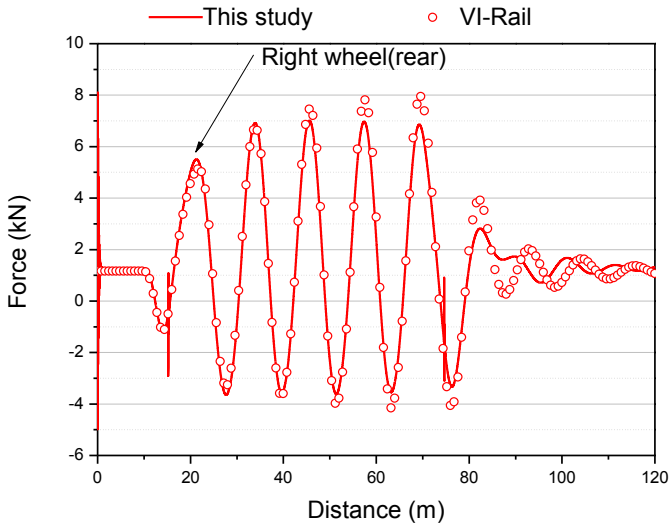

(b) Lateral wheel load : rear-right wheel

Figure 3.8 Comparison of contact force : Case 3

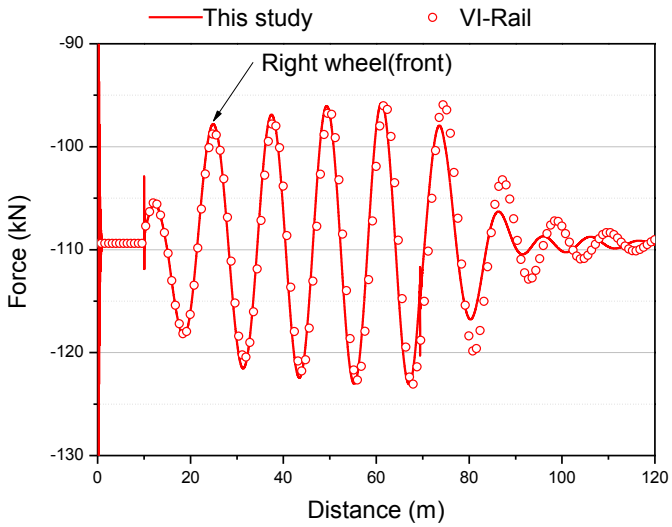

(a) Vertical wheel load : front-right wheel

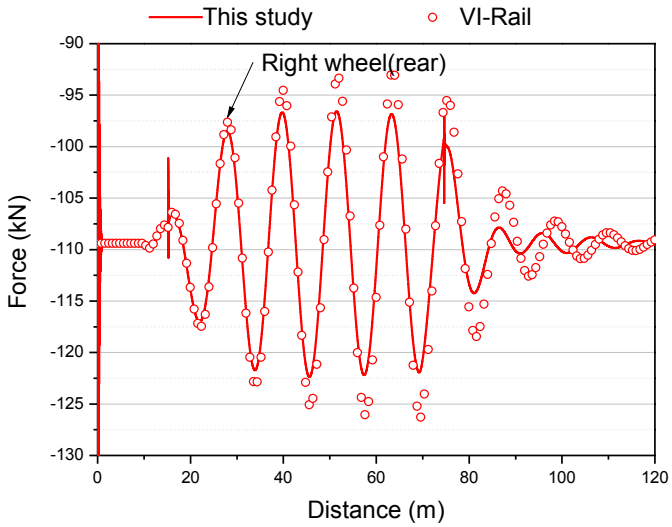

(b) Vertical wheel load : rear-right wheel

Figure 3.8 Comparison of contact force : Case 3 (continued)

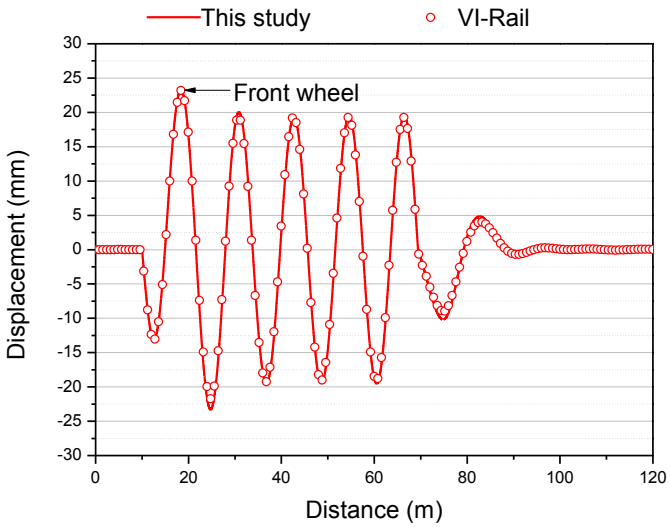

(a) Lateral displacement : front wheelset

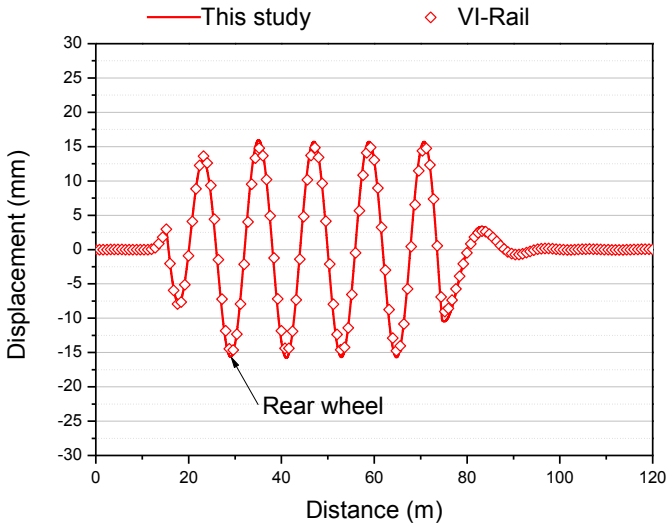

(b) Lateral displacement : rear wheelset

Figure 3.9 Comparison of displacement : Case 3

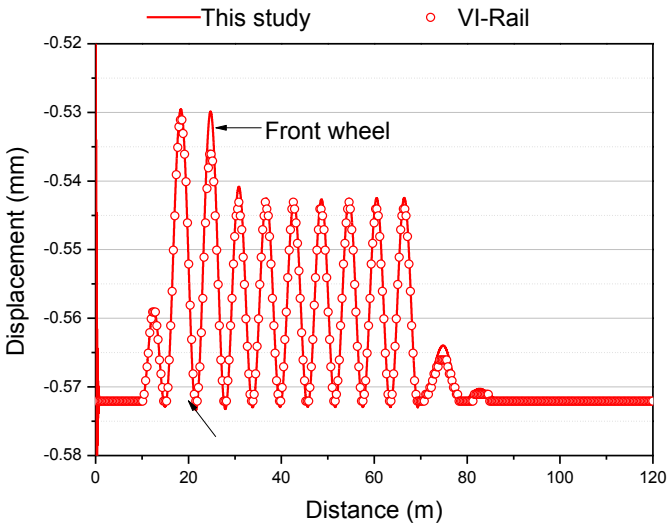

(c) Vertical displacement : front wheel

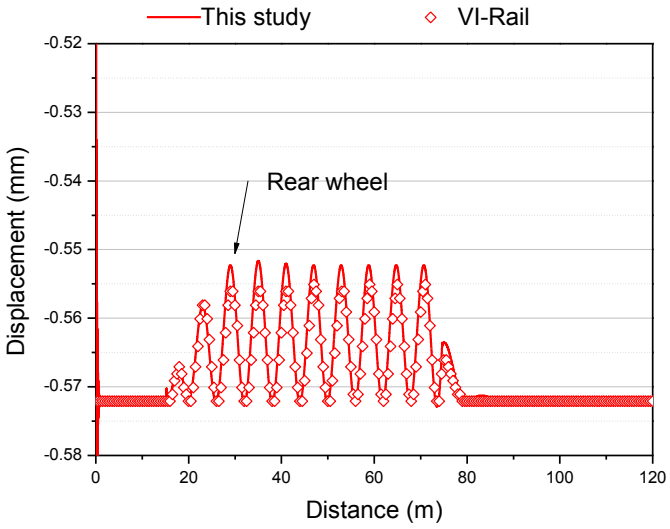

(d) Vertical displacement : rear wheel

Figure 3.9 Comparison of displacement : Case 3 (continued)

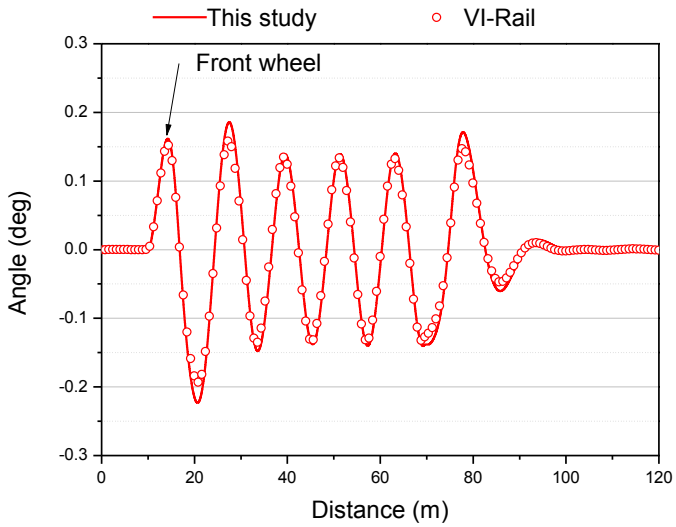

(e) Yawing : front wheel

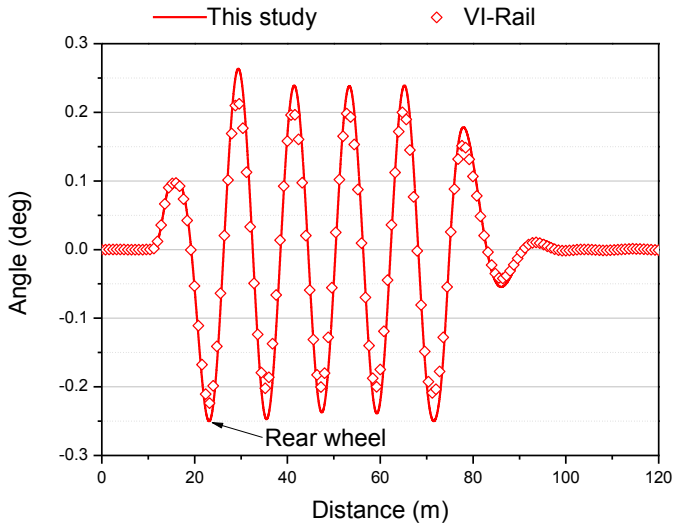

(f) Yawing : rear wheel

Figure 3.9 Comparison of displacement : Case 3 (continued)

(3) Case 4 – Vertical irregularity (harmonic)

Case 4 simulates and analyzes the vertical track irregularity of periodic sinusoidal wave. While case 3 focused on verifying lateral force according to the lateral track irregularity of periodic sinusoidal wave, Case 4 attempts to verify the vertical motion of train/track interaction.

If there is a periodic sinusoidal track irregularity in the vertical direction, the vehicle is displaced in the vertical direction, and accordingly the wheel load will continue to fluctuate.

Figure 3.10 deals with the comparison of normal force which is perpendicular to the contact plane and dependent on the penetration depth as a result of wheel/rail contact. Like the result of Case 3, there is a slight gap in the peak values but a perfectly consistent curve shape and vibration period. Although the variation of lateral creep forces in Figure 3.11 is not big but it show a good agreement with VI-Rail. The lateral and vertical contact forces after rotation to global coordinate, are almost as same as that of VI-Rail in their peak values and patterns. (Figure 3.12) Especially the vertical displacement of wheelset is perfectly matching so that the difference of two peak values are under a few μm. (Figure 3.13)

Through the analysis of Case 4, the vertical response of running train under the consideration of wheel/rail contact is verified.

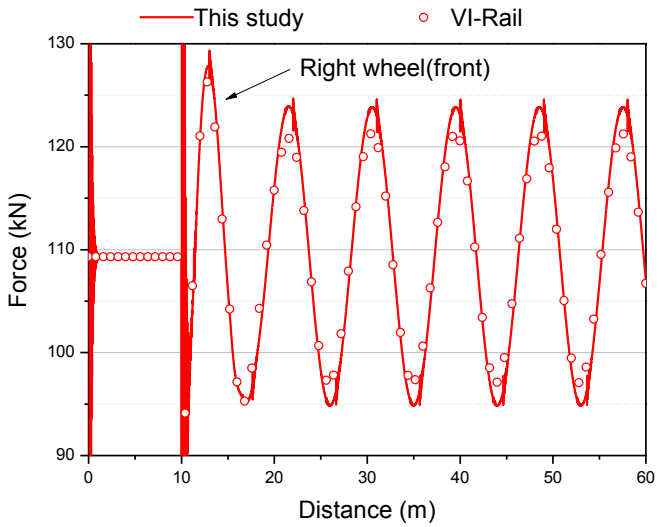

(a) Front-right wheel

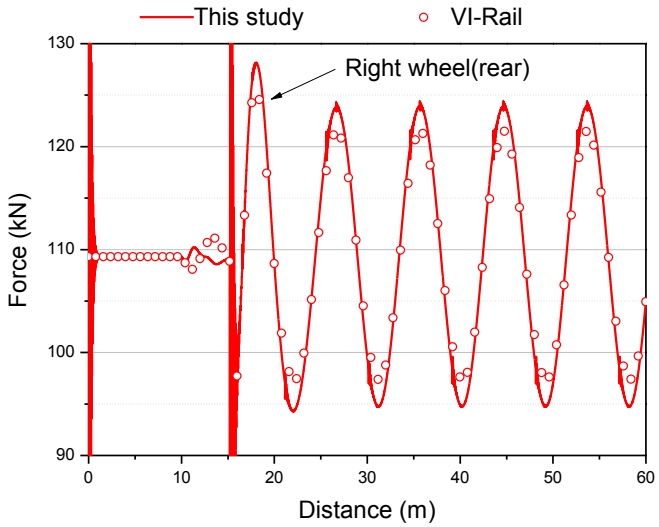

(b) Rear-right wheelset

Figure 3.10 Comparison of normal force : Case 4

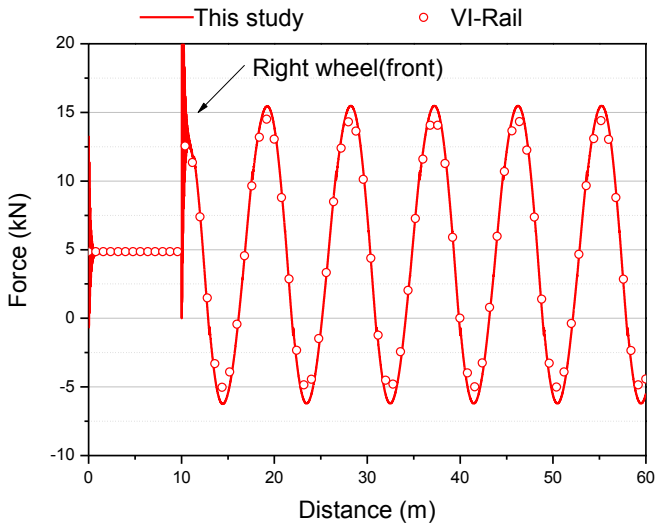

(a) Lateral creep force : front-right wheel

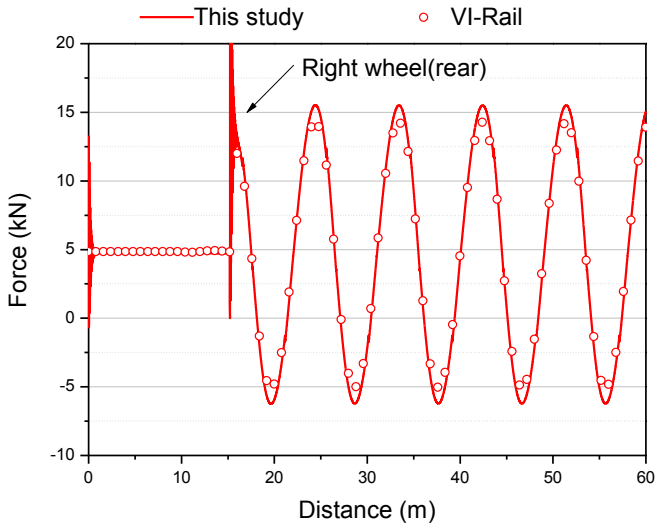

(b) Lateral creep force : rear-right wheelset

Figure 3.11 Comparison of creep force : Case 4

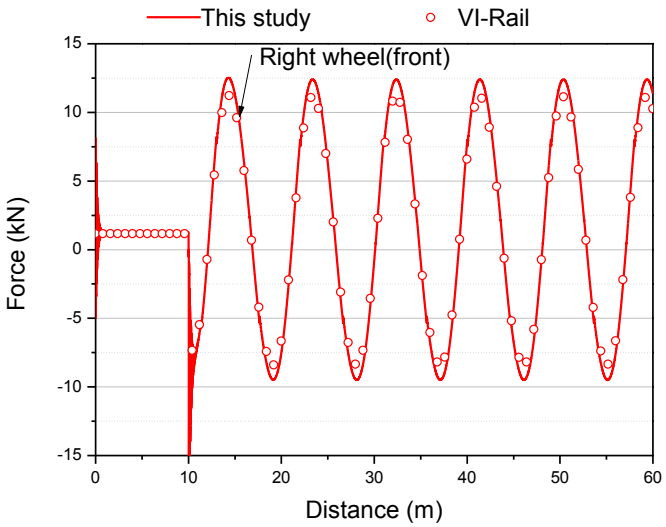

(a) Lateral wheel load : front-right wheel

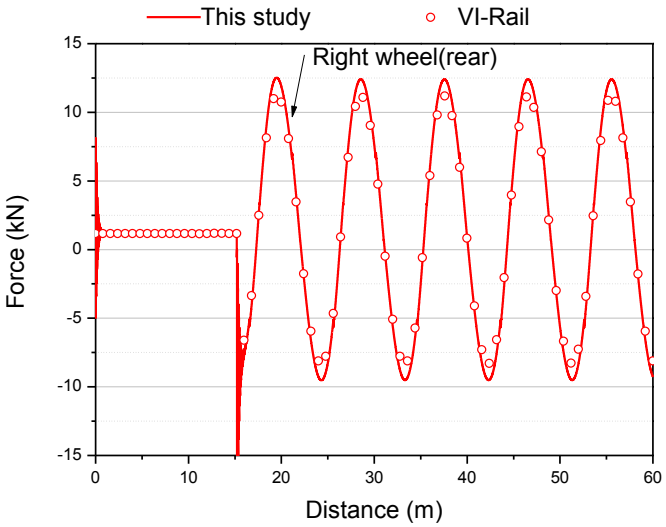

(b) Lateral wheel load : rear-right wheel

Figure 3.12 Comparison of contact force : Case 4

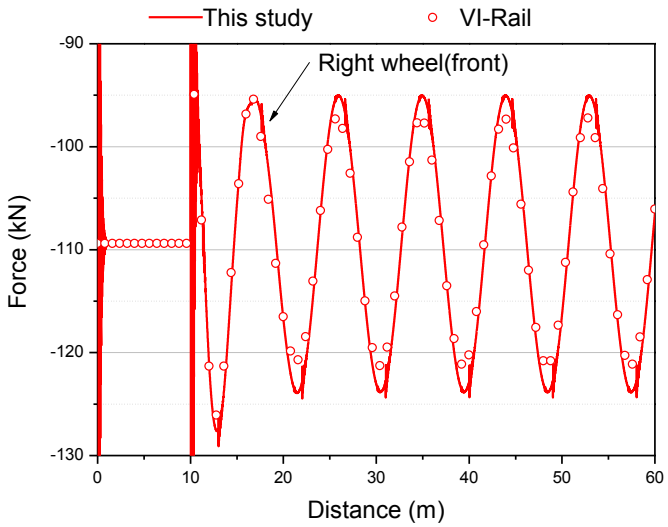

(c) Vertical wheel load : front-right wheel

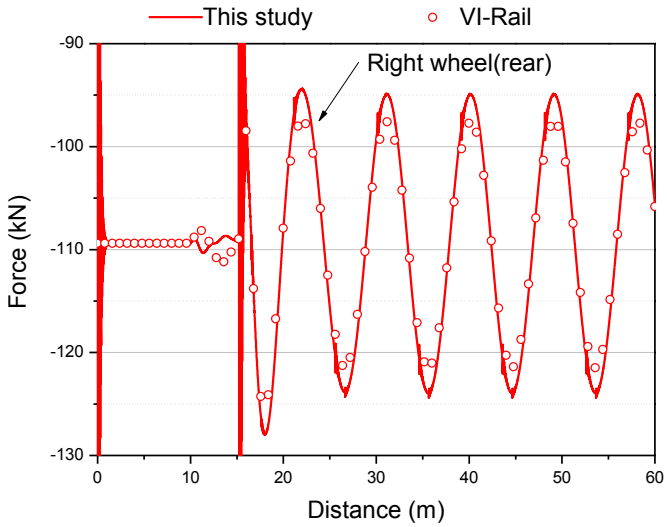

(d) Vertical wheel load : rear-right wheel

Figure 3.12 Comparison of contact force : Case 4 (continued)

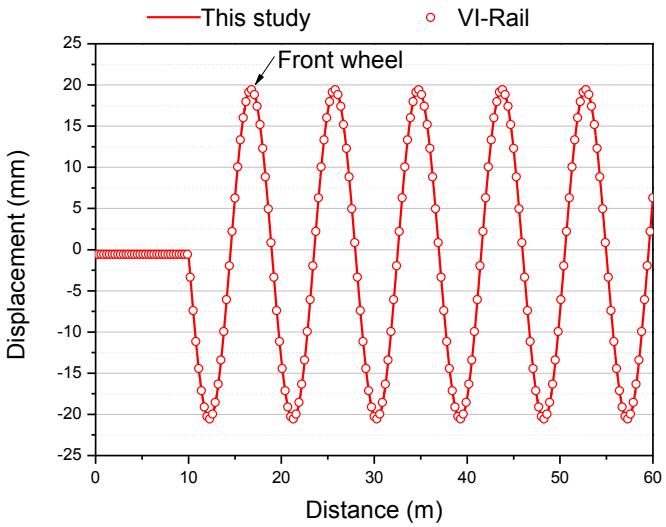

(a) Vertical displacement : front wheelset

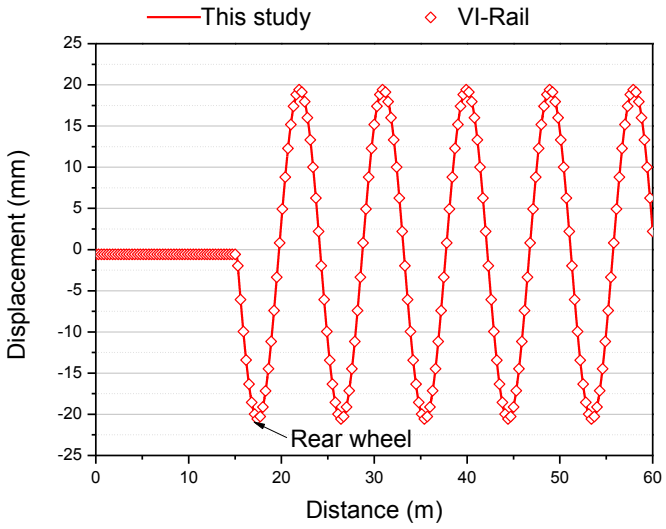

(b) Vertical displacement : rear wheelset

Figure 3.13 Comparison of vertical displacement : Case 4

3.2.4 The effect of irregularity on train runnability

In order to verify the interaction between wheel and rail, one case study is performed as a variable of the magnitude of track irregularity. After assuming one track irregularity on a straight track alignment, five different magnitudes of track irregularity which have the same shape but different amplitude of irregularity, are applied to the train/track interaction.

When the track irregularity gets bigger and bigger, the wheelload and the acceleration becomes larger as the Figure 3.14 which shows the almost linear relationship. The time history of each response is in Figure 3.15. Because the wave shape is same in all the cases, each response has the same shape but the amplitudes gets different. Such phenomenon is thought to be reasonable in wheel/rail interface.

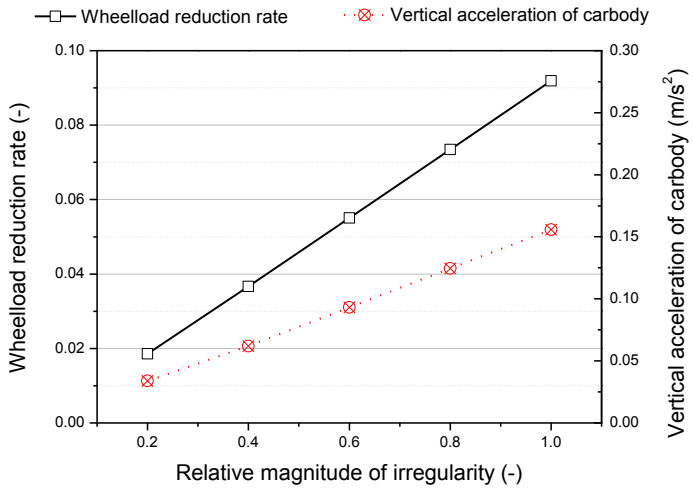

Figure 3.14 Train response for the track irregularity : comparison

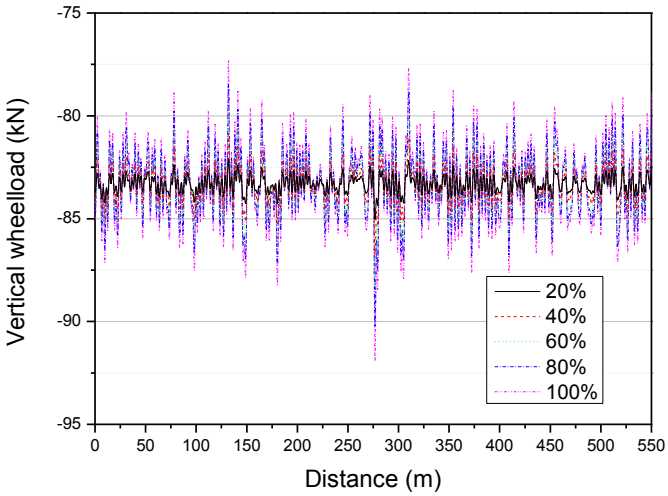

(a) Vertical wheel load

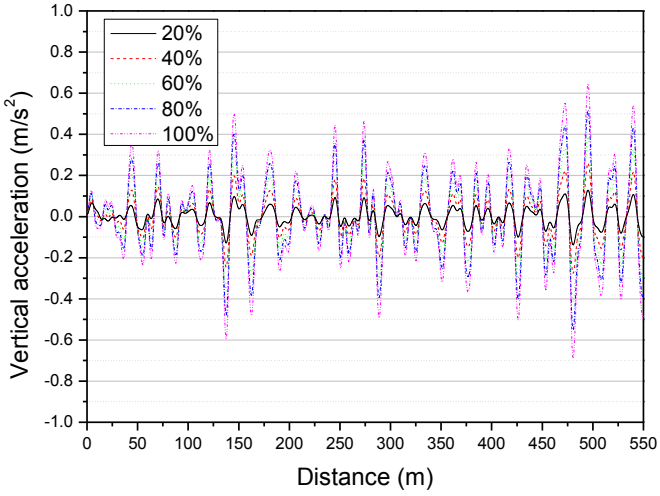

(b) Carbody acceleration

Figure 3.15 Train response for the track irregularity : time history

3.3 Verification of track/bridge interaction

3.3.1 Combination of DSM and MSM

This section aims to verify the results of modeling track and substructure including bridge. Track is modeled by means of Direct Stiffness Method (DSM), substructure is modeled by means of Mode Superposition Method (MSM) and both track and substructure are combined to share the interface DOFs according to the Eq. (2-10).

APATSI(All-Purpose Analysis of Train-Structure Interaction) whose applicability is proven through Yang[91] in 2D vertical analysis, was used as a target program for verification of track/bridge interaction. Since the wheel/rail contact including lateral interaction is already verified in 3.2 and the combination of DSM and MSM formulates the lateral and vertical interaction at the same time like Eq. (2-10), verification of vertical-only interaction in substructure modeling can also prove the validity of lateral interaction. Consequently, if the result of this study is well-matched to APATSI in vertical analysis, the combined analysis of DSM and MSM can be verified in 3D interaction between track and substructure.

For comparison of both programs, a simple beam with 25m span length is modeled as Figure 3.16. The analysis sets up a situation that KTX power car runs on the simple beam with 10m/s and 100m/s respectively in order to show the effect of train speed. The involved results are presented in Figure 3.17~Figure 3.18.

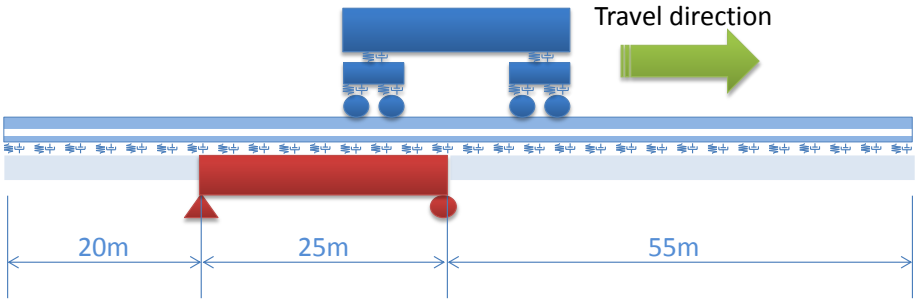

Figure 3.16 Verification model of track/bridge interaction

The time history of vertical wheel load and carbody acceleration shows good agreement in Figure 3.17 and Figure 3.18 for both slow and fast cases. The patterns of increasing wheelload and acceleration in case of fast-running train are almost same in Figure (a) and (b).

So far the combination method of DSM and MSM used in this study is verified by comparing the result of vertical interaction using APATSI, which means the combination method is still valid to vertical and lateral interaction between track and substructure.

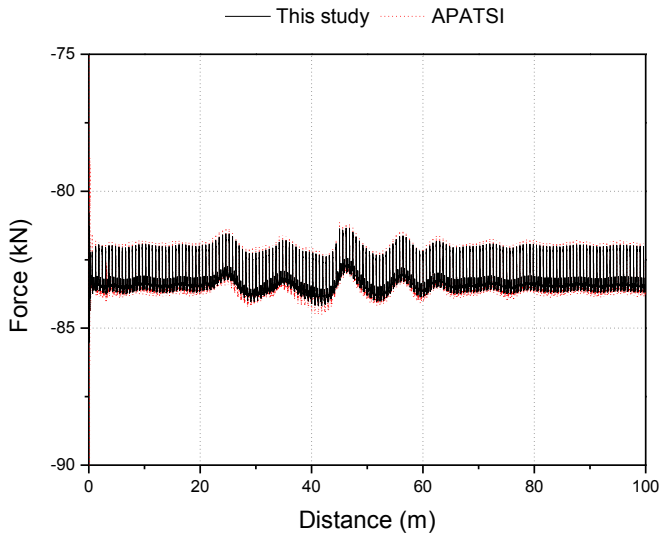

(a) V_T=10m/s

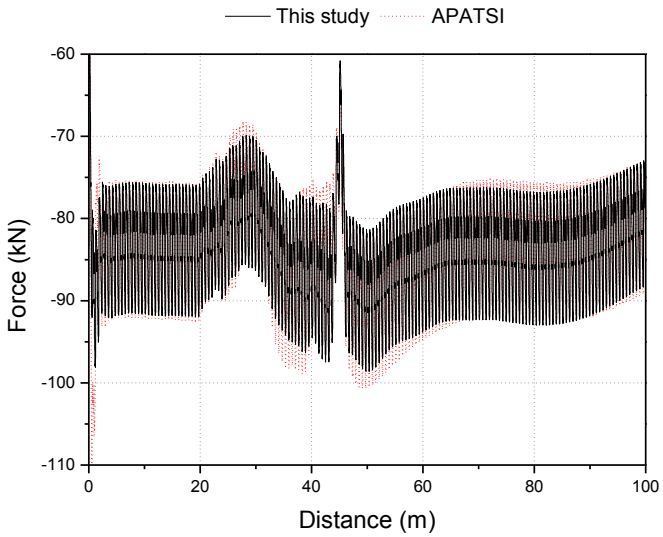

(b) V_T=100m/s

Figure 3.17 Comparison of vertical wheelload to APATSI

(1st wheelset)

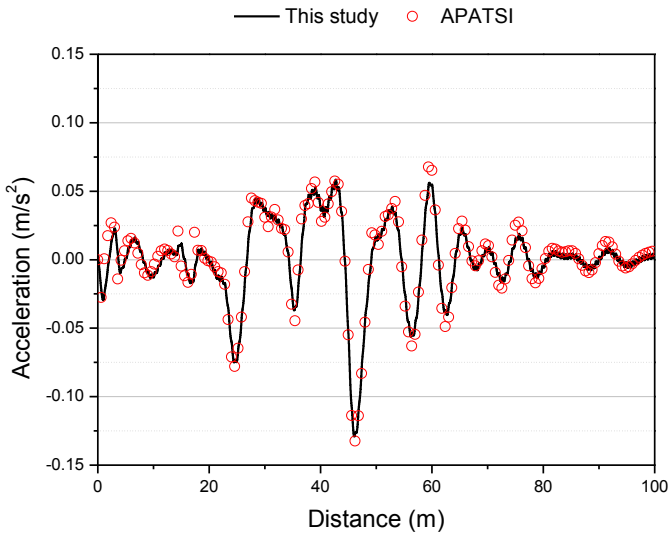

(a) V_T=10m/s

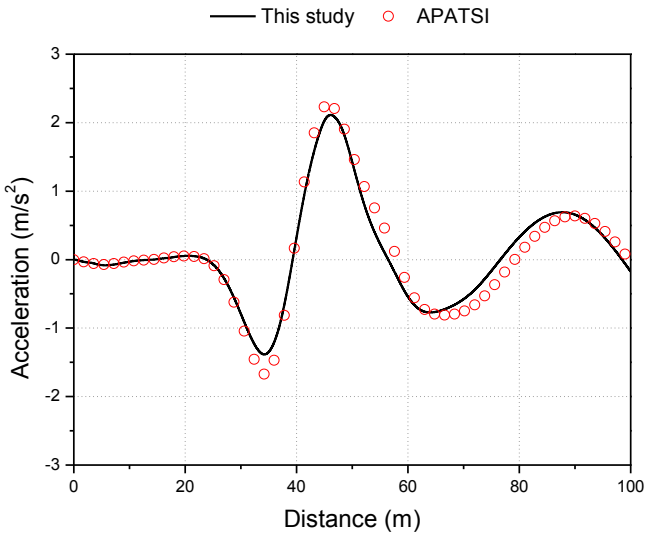

(b) V_T=100m/s

Figure 3.18 Comparison of vertical acceleration of carbody to APATSI

(1st wheelset)

3.3.2 The effect of train speed on train runnability

In order to verify the interaction between train and bridge, the effect of train speed running on a bridge is investigated. The train is assumed to run on a simple beam which is the same as Figure 3.16, and the train speed varies as a step of 50km/h from 50km/h to 250km/h. (total five cases)

The result is easily estimated to show the increasing tendency as the rising train speed. In fact, both the vertical wheelload and the vertical acceleration of carbody gets larger as the train goes faster as Figure 3.19. When the train enters the bridge, the bridge deforms downward as the vertical load of train mass and wheel/rail interaction force are applied to bridge. Because the carbody has its own inertia to go ahead, the wheelload becomes small at the bridge entrance. Reciprocally, when the train passes the middle span of bridge and approaches the exit, the bridge tends to restore its original shape upward and such action makes the wheelload bigger like Figure 3.19(a). The result can be concluded to be reasonable under the consideration of the train/bridge interaction.

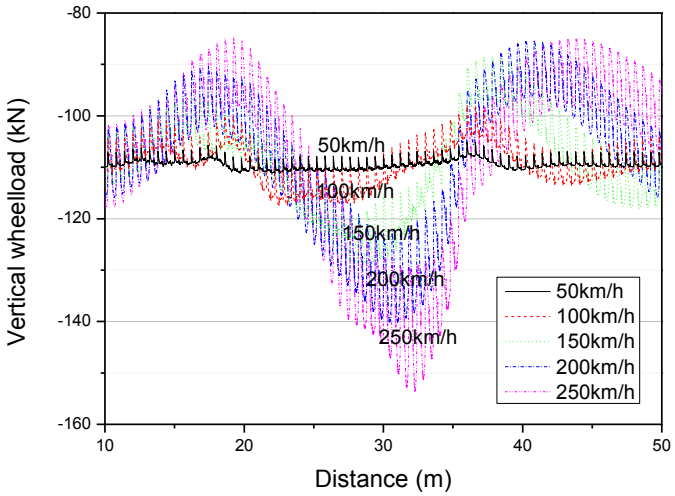

(a) Vertical wheel load

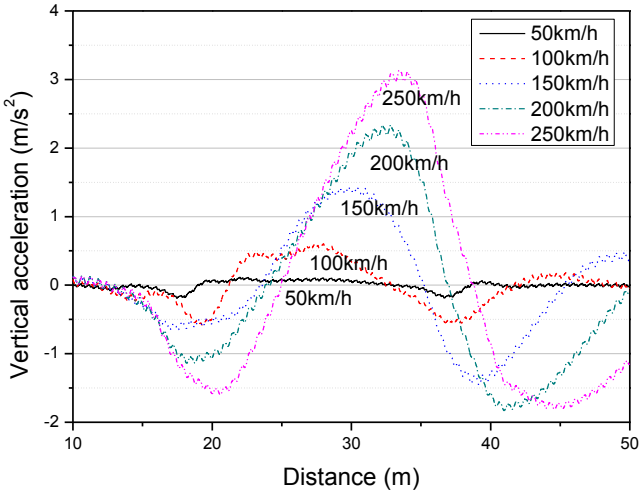

(b) Carbody acceleration

Figure 3.19 Train response for the train speed on bridge : time history

3.3.3 Validity of moving track

In Section 2.3.1, the long track is modeled as the divided and moving track. Especially Cho[99] analyzed the response characteristics according to whether or not the track was modeled outside the PSC-I girder bridge and concluded the track model can affect to the natural frequency of bridge. Therefore it is necessary to check that the moving track yields the same results as the whole track on bridge area.

To do so, two different track types are modelled like Figure 3.20 for Yeongjong Bridge. Whole track extends the rail on bridge to the outside 100m~200m long, and the moving track is divided into just track length. In order to compare the severe condition, the wind velocity is assumed to be 20m/s, and the train velocity 200km/h for accelerating the bridge and track enough. The relevant results are in Figure 3.21~Figure 3.23.

First, the vertical displacements (Figure 3.21) and accelerations (Figure 3.22(a)) of bridge are almost same that the difference is only 1.4% and 2.0%, respectively. The difference of vertical acceleration of train is calculated over 3%. (Figure 3.23) Differently from the result of Cho[99], the modal frequencies are not apparently seemed to be shifted, (Figure 3.22(b)) because the mass and stiffness of cross section in Yeongjong Bridge is much bigger than that of PSC-I girder bridge, and the strengthening effect of long rail is relatively small. Therefore the response of divided and moving track is assumed to be almost same as the whole track model.

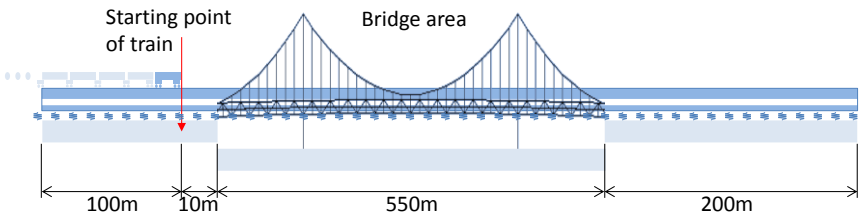

(a) Whole track (long rail)

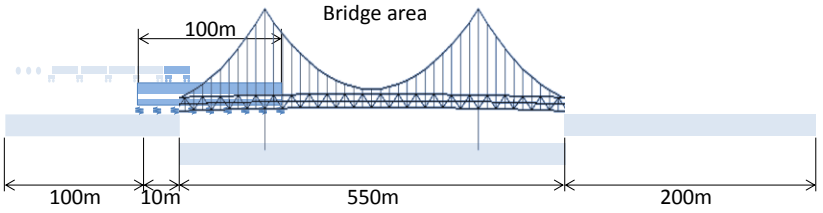

(b) Moving track (divided rail)

Figure 3.20 Definition of whole track and moving track

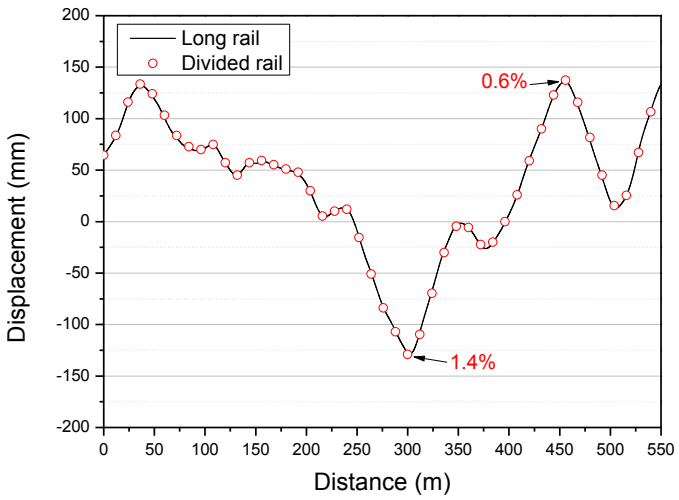

Figure 3.21 Comparison of vertical displacement for track types : bridge

(at center of middle span)

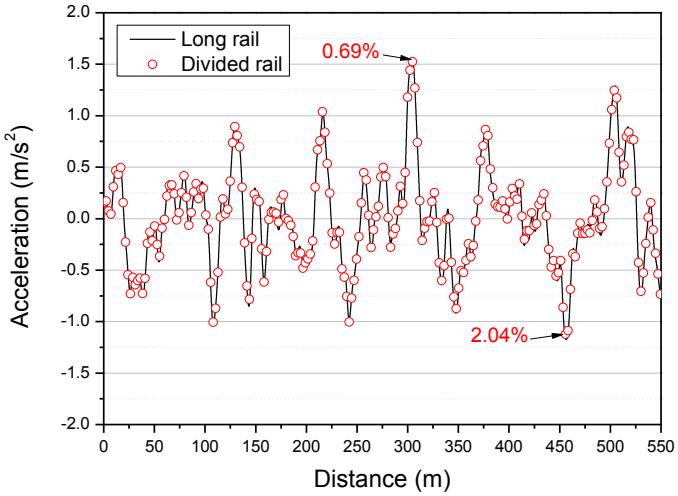

(a) Time domain

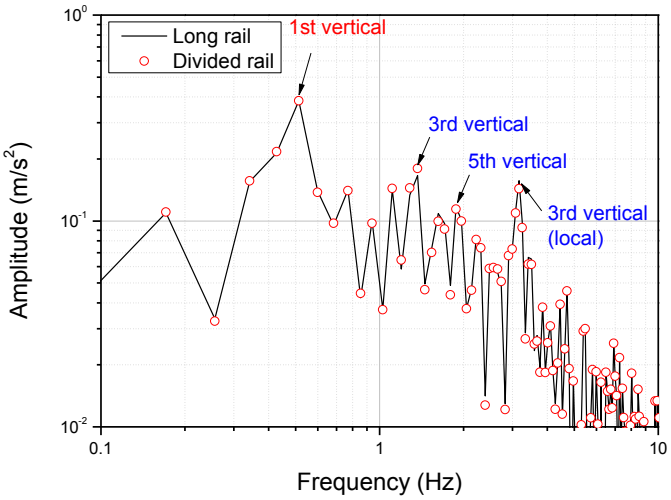

(b) Frequency domain

Figure 3.22 Comparison of vertical acceleration for track types : bridge

(at center of middle span)

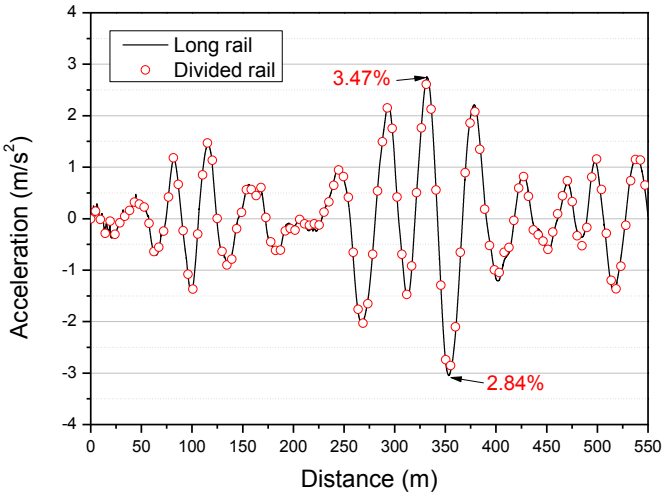

Figure 3.23 Comparison of vertical acceleration for track types : carbody

However when considering the computing time, there is a huge gap. Since the size of system matrix in whole track is 6 to 7 times as big as that of moving track, the analysis time of whole track is 4 to 5 times as long as that of moving track. As a result, little difference in response and great efficiency in computing time allows to use the divided and moving track reasonably in this study.

3.4 Verification of wind/bridge interaction

System Matrix Approximation (SMA) itself is already proved by Jung.[85] This section verifies the application of SMA to the Yeongjong Bridge by checking the displacement result under wind condition.

The target program for comparison and verification is SNUSUS, which is developed for the buffeting analysis in time domain by Structural Design Laboratory in Seoul National University. SMA takes the modal analysis result of SNUSUS as input system matrices and natural frequencies.

SNUSUS uses a Fourier Series Approach (FSA), which is a fitting method for flutter derivatives, for considering self-excited forces and admittance functions.[100] But SMA approximates structural aerodynamic transfer function by a second-order polynomial to eliminate the dependency of the structural aerodynamic transfer function on frequency. Even though each method follows its own equations, the vertical and lateral displacements of Yeongjong Bridge at the center of middle span under the wind of 20m/s, show very good agreement in Figure 3.24. The legend “MSM” indicates mode superposition results without reflecting the aeroelastic effect in it, and the displacement result of MSM deviates from the other two results.

If the aeroelasticity is not included, the response of bridge would be overestimated under the strong wind condition, and the accurate evaluation for the safety could not be performed. As a way to consider the aeroelasticity, system matrix approximation method which can be combined to the mode superposition method, is concluded to be comparatively accurate and efficient.

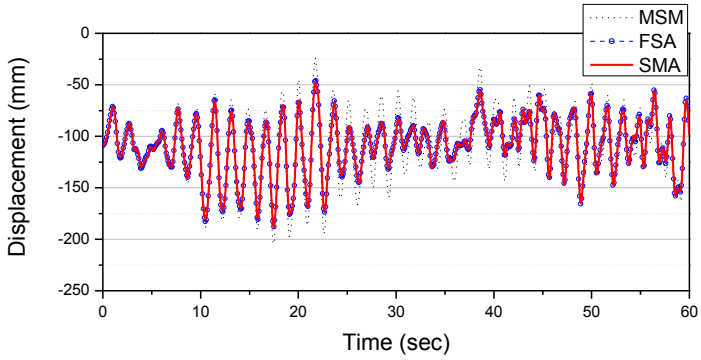

(a) Lateral displacement

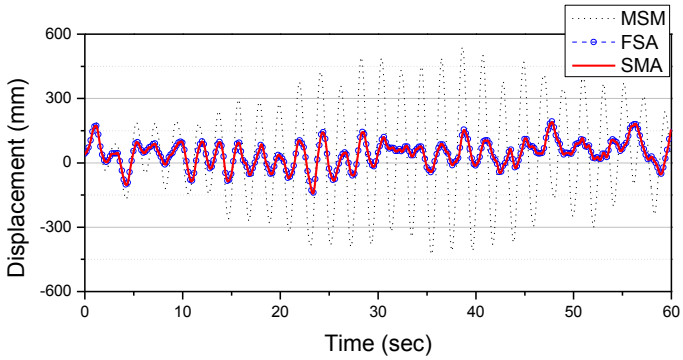

(b) Vertical displacement

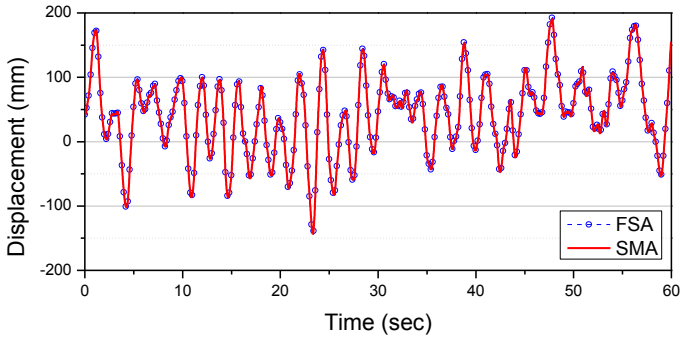

(c) Vertical displacement (magnified)

Figure 3.24 Comparison of results of wind interaction

Chapter 4 Case study for KTX on Yeongjong Bridge

4.1 Basic assumptions of simulation

This section figures out some basic assumptions for applying the unified approach to the simulation of the real bridge. First, the vehicle is chosen to model KTX which is composed of one power car with detailed modeling and the subsequent 9 cars simplified as moving masses. The moving mass model can sufficiently reflect the inertia effect of carbody interacted with the bridge movement. The power car, as well as the following 9 cars is assumed to be applied by the wind force on the carbody at the wheelset position.

Wheel profile is assumed be bilinear, (Figure 2.8(b)) and the yawing of wheelset is ignored only in determining the contact position between wheel and rail.

The target bridge is Yeongjong Bridge, as mentioned in section 2.3.2. Among the total 4,420m length, only 550m length for suspension bridge is modeled in this study, (Figure 4.1) and the other part is assumed as track on roadbed, not the substructure. The modal analysis for Yeongjong Bridge is performed using SNUSUS, as mentioned in section 3.4. As a part of modal analysis result, the information of natural frequency is summarized in Table 4.1, and the representative mode shapes are shown in Figure 4.2. The total count of used mode is 50, and the damping of bridge is assumed as Rayleigh damping with the damping ratio 0.006 for 1^{st} and 2^{nd} modes.

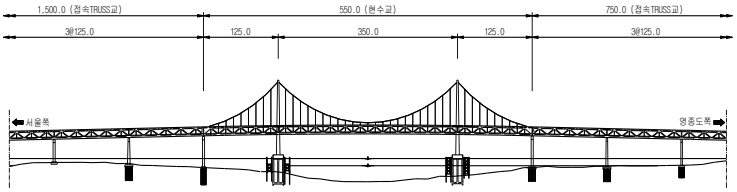

(a) Side view

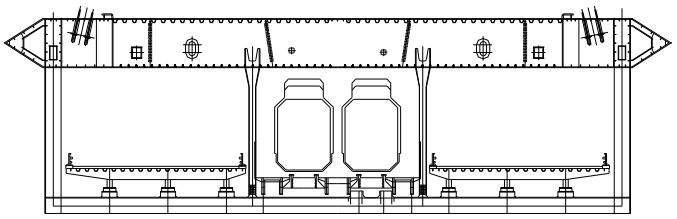

(b) Sectional view

Figure 4.1 Drawing of Yeongjong Bridge

Table 4.1 Modes and natural frequencies of Yeongjong Bridge

Mode	Natural frequency (Hz)	Mode shape	Mode	Natural frequency (Hz)	Mode shape
1	0.327		11	0.983	
2	0.486	1st V	12	0.984	
3	0.592	1st L	13	1.183	2nd L
4	0.772	2nd V	14	1.254	1st T
5	0.830		15	1.292	
6	0.847		16	1.322	
7	0.874		17	1.399	3rd V
8	0.883		18	1.502	
9	0.976		19	1.504	2nd T
10	0.982		20	1.665	

Notes) V : vertical mode, L : lateral mode, T : torsional mode

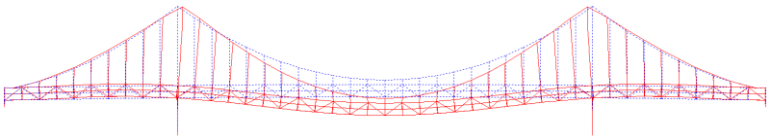

(a) 1st vertical mode (side view)

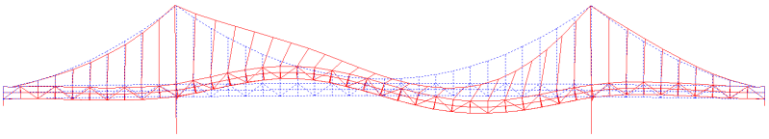

(b) 2nd vertical mode (side view)

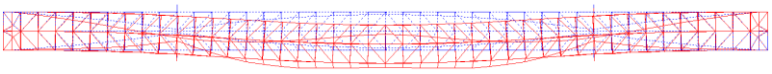

(c) 1st lateral mode (top view)

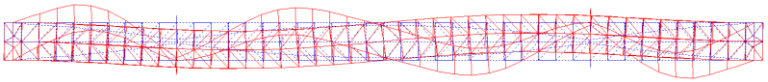

(d) 2nd lateral model (top view)

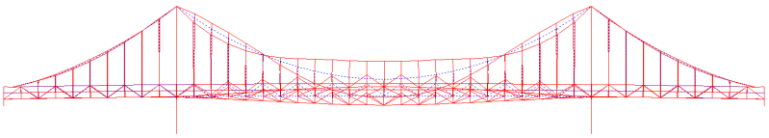

(e) 1st torsional mode (side view)

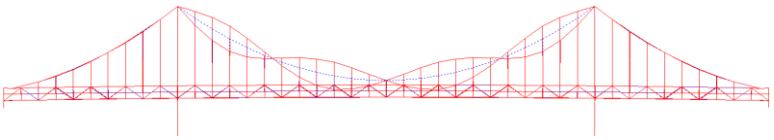

(f) 2nd torsional mode (side view)

Figure 4.2 Representative mode shapes of Yeongjong Bridge

The track is modeled only using rail and fasteners because the rail is installed on the longitudinal frames with direct fastening system in Yeongjong Bridge. The rail is assumed as UIC 60 whose sectional properties and profile is used in input parameters, and is modeled as Timoshenko beam element for reflecting the characteristics of deep beam. Detailed properties for rail and fastening system used in this simulation is summarized in Table 4.2. Finally the in-situ measured data on Yeongjong Bridge by KORAIL, the public corporation in charge of railway maintenance, are used for an input of track irregularity. (Figure 4.3~Figure 4.4)

The wind under consideration is only perpendicular to the bridge because such a wind condition is estimated as the worst case for the response of bridge. Therefore the incidence angle for an input variable of the aerodynamic coefficients can be acquired by a simple calculation like Eq. (4-1).

$$\beta = \arctan\left(V_W / V_T\right) \tag{4-1}$$

where β : incidence angle

V_W, V_T : velocity of wind and train respectively (m/s)

As mentioned in Section 2.5.2, the aerodynamic coefficients of Orellano[70] are used in this study for calculating the wind load on train. (Figure 2.16) Since the result of Orellano[70] was obtained under the condition of running on roadbed, it has to be adjusted for the train running on bridge. But because Yeongjong Bridge is wide enough and the trains run in the middle of deck, (Figure 4.1(b)), it is possible to neglect the effect of bridge on the coefficients.

Table 4.2 Main parameters of the track modeling

Rail mass	60.3kg/m
Cross-sectional area of the rail	$7.750 \times 10^{-3} m^2$
Moment of inertia of the rail	$3.090 \times 10^{-5} m^4$
Young's modulus of the rail	210.0GPa
Poisson ratio of the rail	0.3
Shear factor of the rail	0.34
Stiffness coefficient of the fastener and pad Vertical / Lateral / Longitudinal	50 / 1.69 / 10MN/m
Damping coefficient of the fastener and pad Vertical / Lateral / Longitudinal	250 / 10 / 20kN/(m/s)
Length of the sleeper span	0.60m
Inclination of rail base	1:20
Friction coefficient b/w wheel and rail	0.4

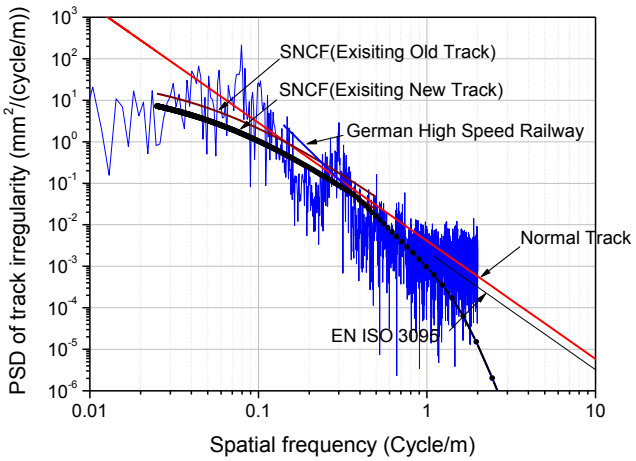

Figure 4.3 PSD of track irregularity in Yeongjong Bridge

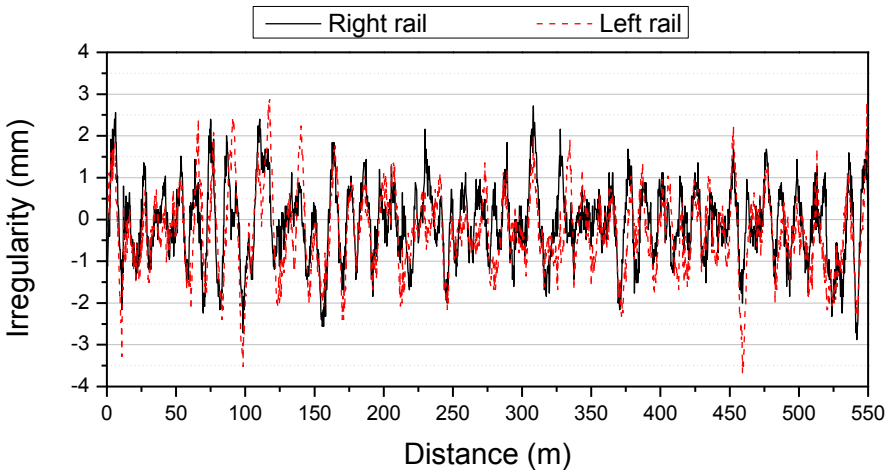

(a) Lateral irregularity

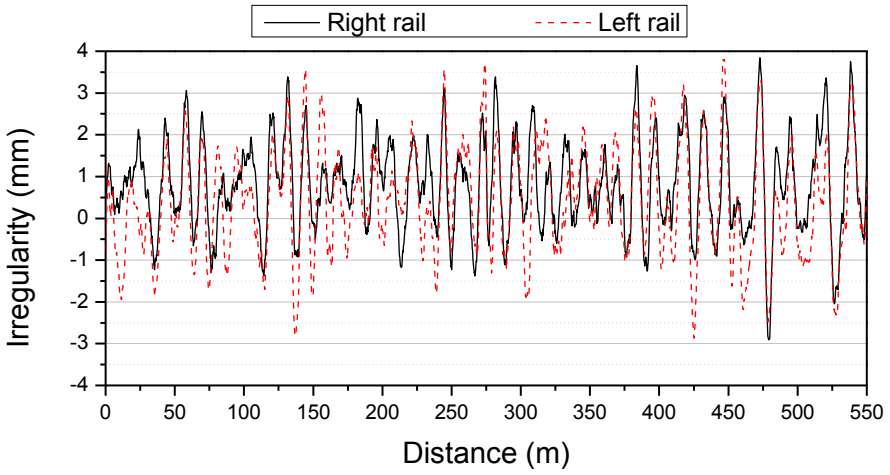

(b) Vertical irregularity

Figure 4.4 Measured irregularity in Yeongjong Bridge

According the aerodynamic coefficients of Orellano[70] and the incidence angle from Eq. (4-1), the side forces for various train and wind velocities can be calculated like Figure 4.5. The side force has a tendency to be larger for the greater wind speed and faster train speed.

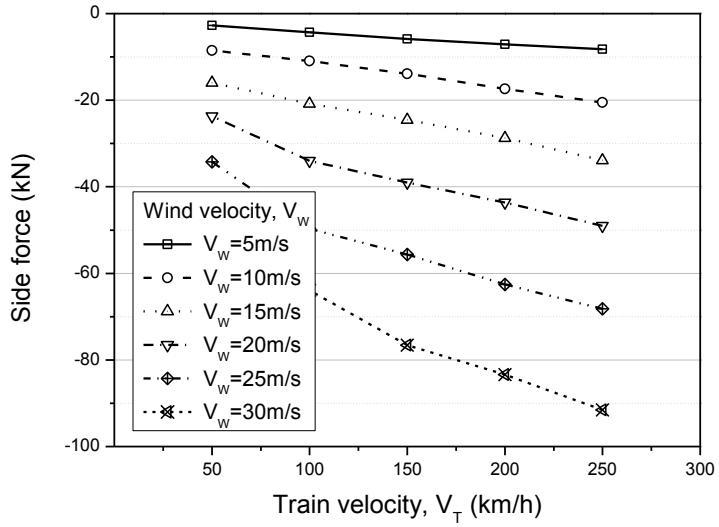

Figure 4.5 Side force on KTX according to wind and train velocity

4.2 Comparative study for the effect of bridge, wind and irregularity

Among many factors that can affect the behavior of running train, the effect of bridge, track irregularity or wind load will be compared in this section. The comparison of analysis for eight different cases in Table 4.3 is carried out.

The target bridge is Yeongjong Bridge and track irregularity is assumed as same as the measured one on Yeongjong Bridge in section 4.1. The wind load is assumed to be 20m/s in the first seed, and the train velocity is 200km/h only.

The lateral displacement of carbody is almost affected by the bridge movement induced by the wind interaction. (Figure 4.6) It is because the long-wave deformation of bridge limits the relative movement between wheel and rail, and the lateral interaction does not interact significantly in this motion.

Table 4.3 Eight cases for bridge, irregularity or wind

Classification	Bridge	Irregularity	Wind
Case-NB-NI-NW	No	No	No
Case-NB-NI-YW	No	No	Yes
Case-NB-YI-NW	No	Yes	No
Case-NB-YI-YW	No	Yes	Yes
Case-YB-NI-NW	Yes	No	No
Case-YB-NI-YW	Yes	No	Yes
Case-YB-YI-NW	Yes	Yes	No
Case-YB-YI-YW	Yes	Yes	Yes

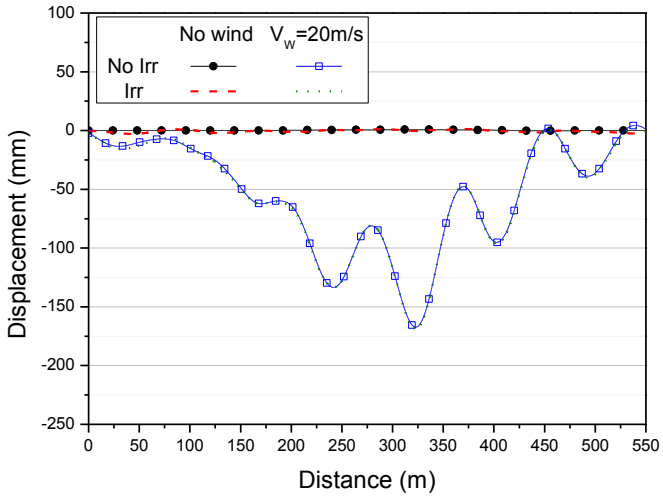

Figure 4.6 Time history of displacement for wind and irregularity

(Lateral displacement of carbody, V_w=20m/s, V_T =200km/h)

Figure 4.7 contains the time history of vertical and lateral wheelloads. Given that there was no wind, both wheelloads experience little variation without track irregularity, and they go through some high-frequency vibration with irregularity. But if there was wind load, they show only long-wave vibration without irregularity, and they undergo the additional short-wave vibrations with irregularity. This phenomenon appears in the same way for the vertical and horizontal acceleration of carbody. (Figure 4.8) The accelerations are little affected by the track irregularity, but they are much affected by the wind-induced response of bridge.

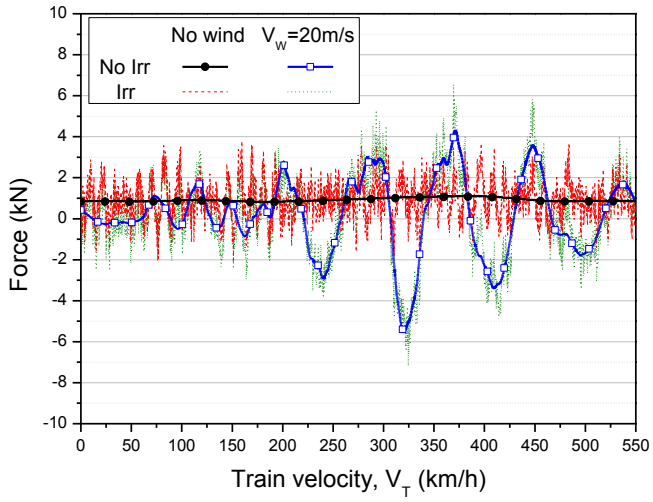

(a) Lateral contact force

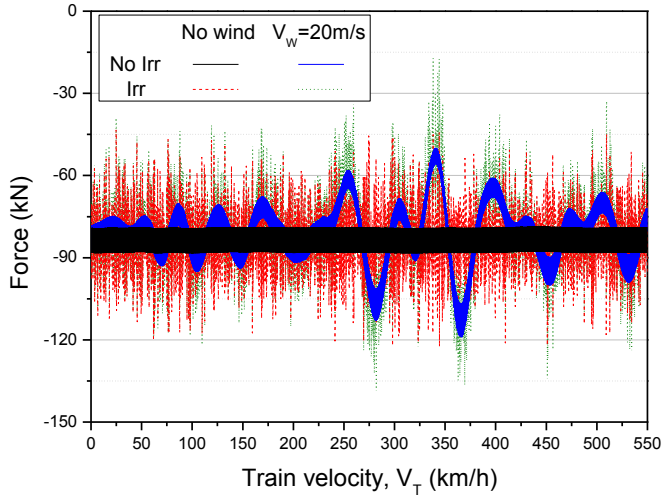

(b) Vertical contact force

Figure 4.7 Time history of wheel load for wind and irregularity

(V_w=20m/s, V_T =200km/h)

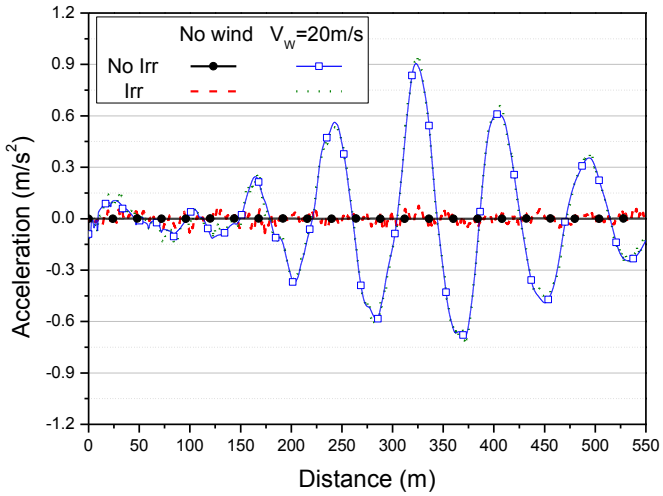

(a) Lateral acceleration of carbody

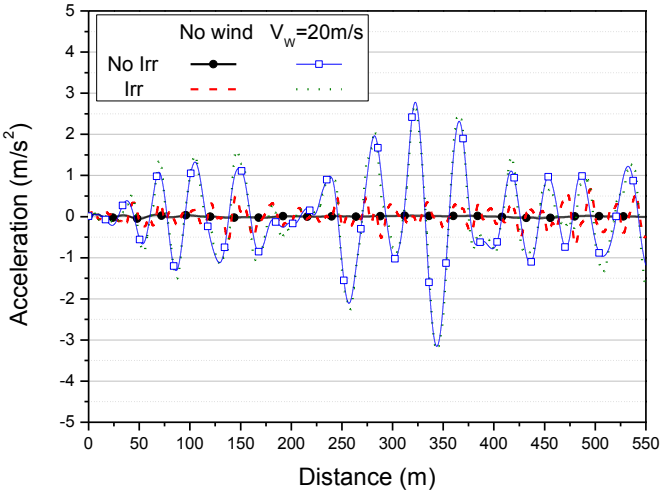

(b) Vertical acceleration of carbody

Figure 4.8 Time history of acceleration for wind and irregularity

(V_w=20m/s, V_T =200km/h)

The acceleration of carbody is the response after being filtered by two main suspension systems – primary and secondary suspensions. Therefore they are susceptible to the bridge motion, and dominantly dependent upon the wind load. However the wheel is not only influenced much by the long-wave bridge deflection according to the wind load, but also affected with high-frequency fluctuation by the track irregularity.

In summary, the wind load can affect dominantly to the assessment result of both safety and running behavior, but track irregularity can influence only the wheelload reduction.

In order to investigate such tendencies in the frequency domain, Fourier transform of vertical wheelload and acceleration are performed. As shown in the time-domain history, wheelload is much influenced by the track irregularity in the high frequency over 4Hz. (Figure 4.9(a)) But the acceleration is only affected by track irregularity within 2~5Hz due to the filter action of suspension. (Figure 4.9(b)) Whereas wheelload has very low frequency amplitude at nearly static area by wind loads, the acceleration does not have such amplitude. However, both responses have common and dominant amplitude within 0.5~2Hz which is induced by wind/bridge interaction, that means the main influence factor for the runnability of KTX on Yeongjong Bridge is bridge motion induced by wind load.

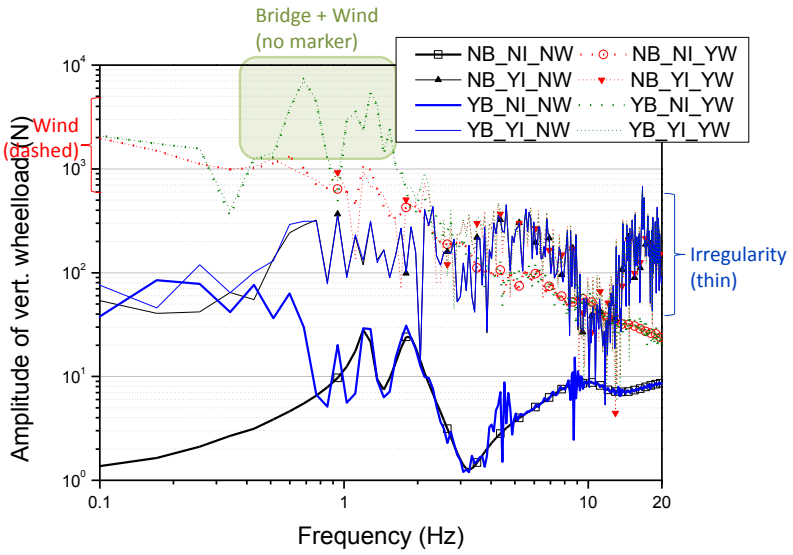

(a) Vertical wheelload : frequency domain

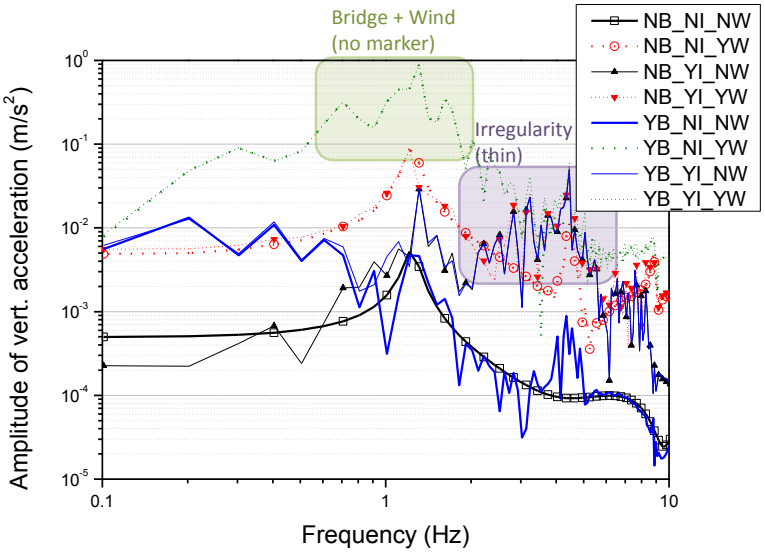

(b) Vertical acceleration : frequency domain

Figure 4.9 Comparison of Fourier transform result for various cases

4.3 Relationship between bridge and train acceleration

To identify the relationship between bridge and train acceleration, the acceleration of bridge deck under wind load without train load is calculated. However for the bridge acceleration to be compared to train acceleration, it has to be assessed at the position of running train according to the train speed. “Case 1” defines the acceleration of “bridge deck” at the longitudinal position of under the wind load without train load, and “Case 2” defines the “train” acceleration at the same position under wind load and train load.(Figure 4.10)

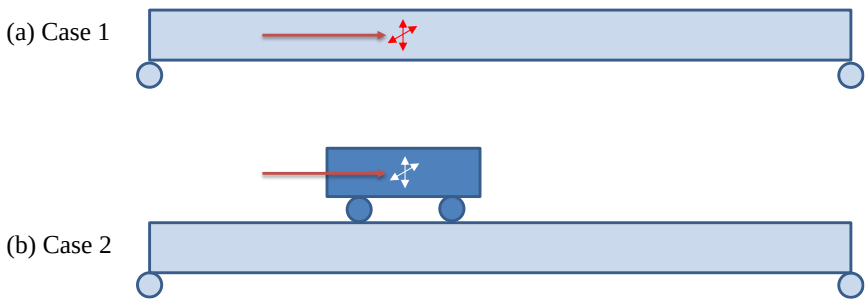

Figure 4.10 Definition of acceleration in bridge deck and train

Figure 4.11 shows the results of the average values for all five seeds under consideration. Even though the acceleration in Case 1 is acquired without the train load, the acceleration of bridge deck at the train position has a strong similarity. Except V_T=250km/h for abnormal lateral acceleration due to amplifying yaw of carbody, the lateral acceleration of bridge in Case 1 shows almost similar peak values and rising trends with the lateral acceleration of train

in Case 2. Although Figure 4.11(a) shows a slight increase of the response from bridge deck to carbody, the lateral acceleration of carbody is closely related to the response of bridge. The maximum lateral force exerted from wind per one car does not exceed 100kN. (Figure 4.5(a)) Because the lateral load is not big, both lateral accelerations show the close relationships.

The vertical acceleration in Figure 4.11(b) gives a similar increasing pattern according to the train velocity, but shows difference in maximum values which is related to the vertical train load applied to the bridge. The static vertical wheelload is about 80kN, and considering 22 wheelsets in 10 cars(Figure 2.3), the total vertical wheelload is summed to be over 3,500kN, which can induce the additional deflection of bridge over 50mm. This train-induced deflection enlarges reversely the acceleration of carbody, which is larger than that of bridge without the train load.

The ratio of train acceleration in Case 2 to bridge acceleration in Case 1 is calculated for every wind and train velocities, and is shown in Figure 4.12. Except for the case of low velocity where the denominator (bridge acceleration) is too small to maintain constant tendency of ratio, it is within two for lateral movement, and within three for vertical movement. If much acceleration data of in-situ long-span bridges have been stacked for a long time, it would be possible to estimate the peak acceleration of running train by just measuring bridge acceleration under wind load.

This analysis proves that the acceleration of carbody running on the cable-stayed bridge has a strong correlation to the bridge acceleration at the train position. Consequently the dynamic characteristics of bridge behavior during the passing time, can give a dominant influence to the runnability of train.

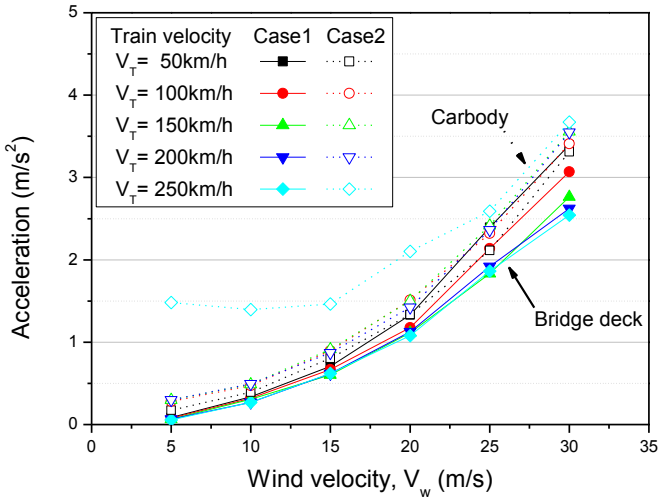

(a) Lateral acceleration of carbody

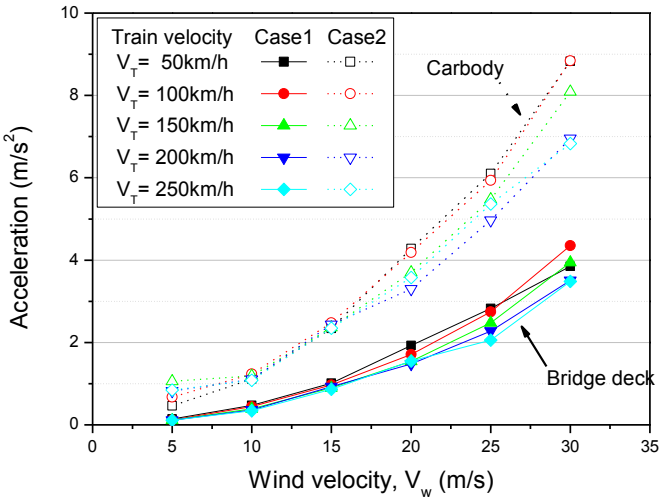

(b) Vertical acceleration of carbody

Figure 4.11 Relationship between bridge and train acceleration : value

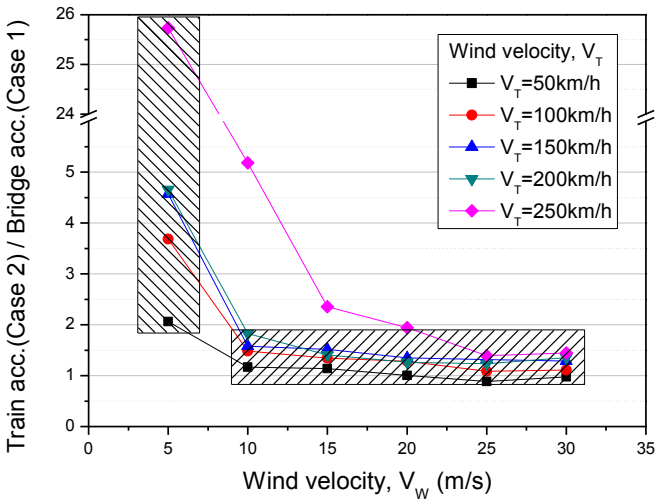

(a) Lateral acceleration of carbody

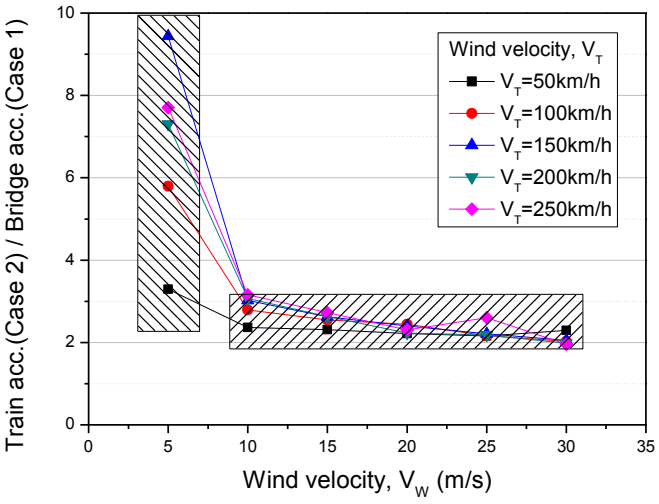

(b) Vertical acceleration of carbody

Figure 4.12 Relationship between bridge and train acceleration : ratio

Chapter 5 Runnability evalution on Yeongjong Bridge

5.1 Assumptions and evaluation criteria

In order to evaluate the train response according to the wind velocity and train speed, the simulation is performed for the combination of various wind velocities (V_W= 5, 10, 15, 20, 25, 30m/s) and train velocities (V_T= 50, 100, 150, 200, 250km/h). Consequently there are 30(=6×5) analysis cases for one seed of wind, and five wind seeds are generated to consider the random characteristics of wind variation. The other basic assumptions for the train, track, and bridge are the same as that in Section 4.1.

According to standards for railway vehicle safety criteria[101], the derailment criterion is

$$K_{PQ} = Q / P \le 0.8 \tag{5-1}$$

where K_{PQ} : derailment coefficient

Q, P : lateral and vertical wheel load, respectively

and the criterion for wheel load reduction is

$$K_{\Delta P} = \Delta P / P_0 \le 0.8 \tag{5-2}$$

where $K_{\Delta P}$: wheel load reduction rate

$\triangle P$: variation of wheel load ($\triangle P = P_0 - P$)

P_0: vertical wheel load on static condition

The UIC leaflet 518[102] suggests Eq. (5-3) for guaranteeing safety

$$\begin{aligned} &[Q/P]_{2m} \le 0.8 \\ &\ddot{y}_b \le 12 - M_b/5 \end{aligned} \tag{5-3}$$

where $[\ \ ]_{2m}$: sliding mean over 2m of track

$\ddot{y}_b$: lateral acceleration of bogie (m/s^2)

M_b : mass of the bogie (ton)

When applying the mass of the bogie in KTX, the limit value of lateral acceleration of bogie is $10.6 m/s^2$.

UIC leaflet 518 also suggests the guideline of running behavior as the lateral and vertical acceleration of carbody for traction units below $2.5 m/s^2$. EN standard[103] sets the standard for ride comfort shown in Table 5.1, but this study follows the criteria of the UIC leaflet 518 as a guideline of running behavior.

Table 5.1 Standards for ride comfort, EN 1990:2003[103]

Vertical car body acceleration(m/s^2)	Level of ride comfort
1.0	Very good
1.3	Good
2.0	Acceptable

5.2 Result of runnability evaluation

In order to identify the trends of overall responses, Figure 5.1~Figure 5.5 shows the maximum responses extracted from each seed as small solid markers, and the average values of all the individual responses as large hollow markers with lines. Every figure contains train responses on the axis of ordinates, and train speed in (a) or wind velocity in (b) on the axis of abscissa.

For the safety assessment of running train, Figure 5.1~Figure 5.3 show the result of derailment coefficient, wheelload reduction rate, and the lateral acceleration of bogie.

The derailment coefficient is taken as a moving average of longitudinal 2m according to UIC 518, and is confirmed to be susceptible to the increasing wind speed. Except the case of V_T=250km/h at which the train experiences the abrupt amplification of carbody yawing, it can be seen that the derailment coefficient increases smoothly with the rising train velocity. The reason is estimated that as the train speed leads the great wind load on train like Figure 4.5, the leeward wheel has to take more lateral load which results in the increasing derailment coefficient. However, for applying the limit of 0.8, the present results are evaluated to be safe for most cases, which means the derailment coefficient is not a sensitive index to evaluate the safety under the wind condition in this evaluation.

Wheelload reduction rate, which is directly affected by the track irregularity, is, therefore, susceptible to the train velocity, and it shows the linear rising tendency as train speed increases, even under the no-wind condition. In addition, since it can also change according to the bridge movement, nonlinearly

increasing pattern happens in connection with the rising wind velocity. Differently from the derailment coefficient, wheelload reduction rate reveals distinctly the higher risk of derailment for faster wind and train velocities. When checking that wheelload reduction rate becomes over 0.8 (the limit value) in some analysis cases, wheelload variation is an important index to evaluate the running safety of train in this study.

Among the three acceleration responses under consideration, only the lateral acceleration of bogie is classified as a safety criterion by UIC leaflet 518. The bogie is affected by the train/track interaction as a component to link to wheelset by primary suspensions. As a result, the lateral acceleration of bogie grows slightly larger with the increasing train velocity, and gets much larger with increasing wind velocity. Like the result of derailment coefficient, most values are much below the limit of 10.6(m/s^2), which means that the lateral acceleration of bogie is not a sensitive index to evaluate the running safety during cross wind in this analysis.

Figure 5.4~Figure 5.5 represent the result of carbody accelerations for evaluating running behavior of train. Because the body acceleration is acquired from the loading points (the wheel/rail contact) through the primary and secondary suspension, it looks like a filtered response of the wheelset acceleration. Therefore, it tends to be more affected by the long-wave vibration due to the interaction with bridge, than by the short-wave impact due to the contact force or track irregularity. In addition, because the length of Yeongjong Bridge is long and the deformation shapes are smooth, the two accelerations does not change significantly with regard to the train velocity like Figure 5.4(a) and Figure 5.5(a).

However, as the displacement and acceleration of bridge deck gets larger due to the growing wind speed, the acceleration of carbody becomes exponentially increased like Figure 5.4(b) and Figure 5.5(b). While the lateral acceleration of carbody satisfies its limit of running behavior ($2.5m/s^2$) for most cases, the vertical acceleration of carbody exceeds already its comfort limit ($2.5m/s^2$) over V_W=20m/s. It is because the vertical acceleration response of the bridge is bigger than the lateral acceleration response, (Figure 4.11) and it is transmitted to the vehicle body which is reacted closely by the acceleration of the bridge. Since the inclination of wheel profile is nearly 1:20 in the tread area (Figure 2.8(b)) and there is gap of about 7mm between wheel flange and rail, the lateral acceleration can be transmitted less than the vertical acceleration.

Both the vertical and lateral accelerations of the carbody are confirmed to be worthy indices to assess the running behavior.

For most wind seeds, there is a curious phenomenon that the acceleration becomes larger for lower train velocity. The reason of such phenomenon is estimated that the train with lower velocity takes longer time to pass the bridge, thus is exposed to the wind load for the longer time, which could finally lead to more interaction between train and bridge. Therefore, the exposure time to wind load has to be categorized into one of major impact factors.

Through the analysis done in this section, the runnability of train on the Yeongjong Bridge under cross wind, is concluded more susceptible to the variation of wind velocity than the train velocity. However, as the train goes faster, the train speed increases the dynamic impact to bridge but decreases the exposure time to bridge vibration. Consequently the train speed does not give significant impacts to the running behavior.

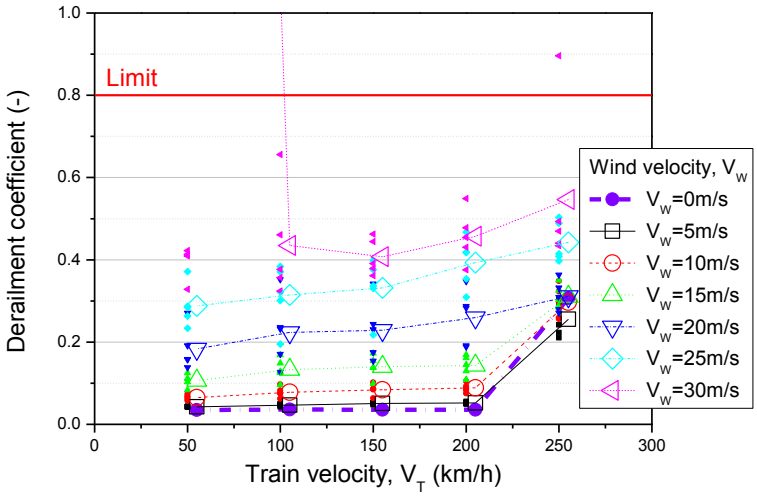

(a) Train velocity vs derailment coefficient

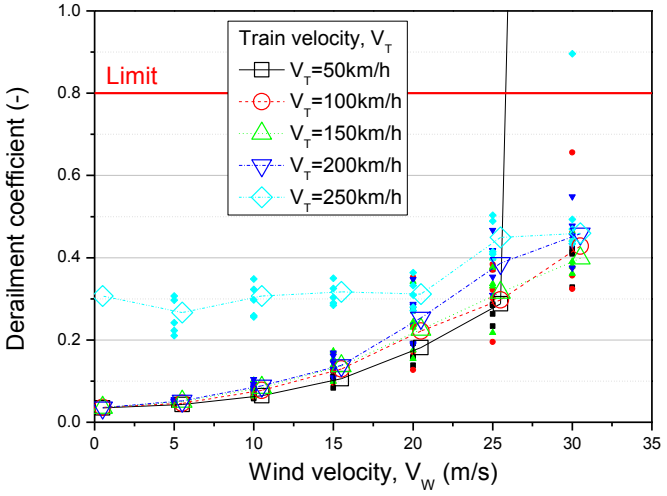

(b) Wind velocity vs derailment coefficient

Figure 5.1 Derailment coefficient

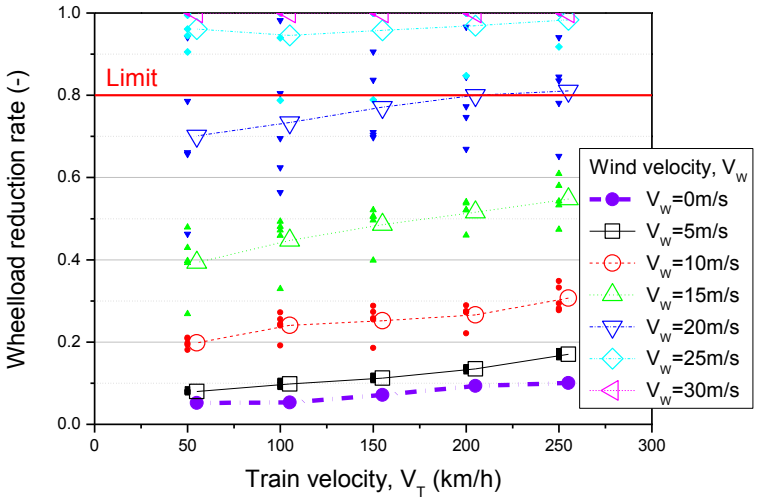

(a) Train velocity vs wheelload reduction rate

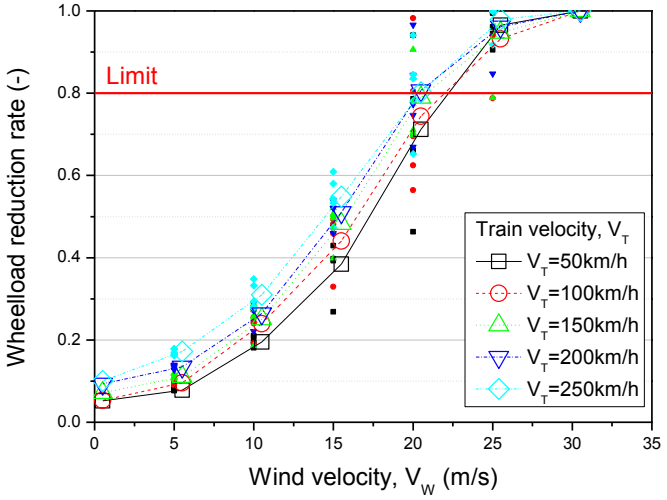

(b) Wind velocity vs wheelload reduction rate

Figure 5.2 Wheelload reduction rate

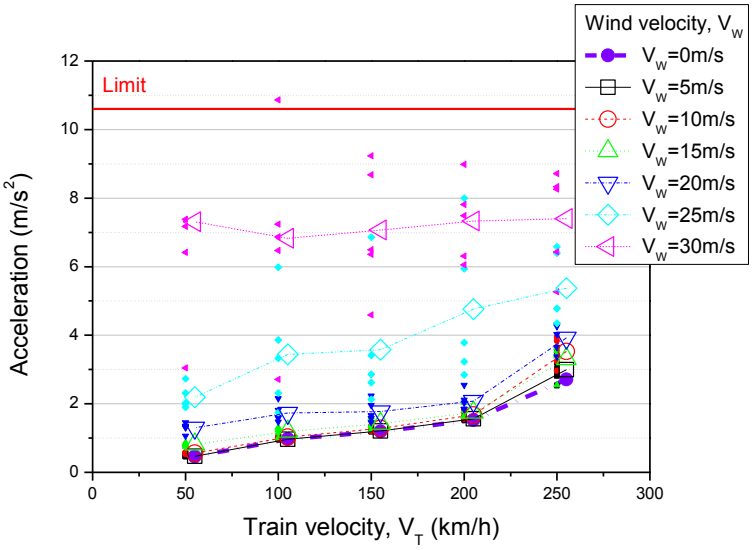

(a) Train velocity vs acceleration

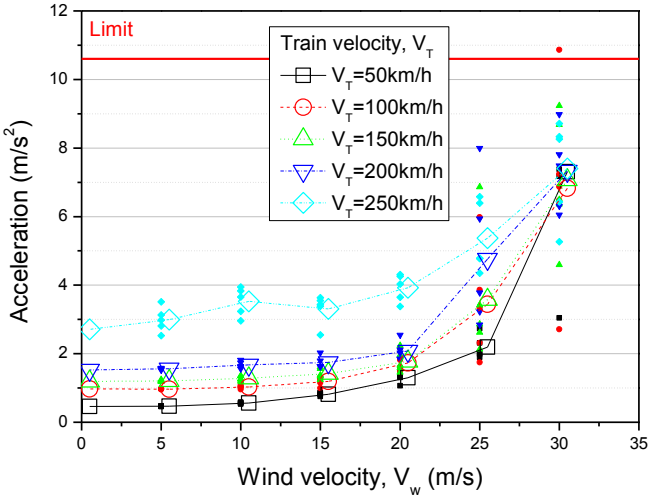

(b) Wind velocity vs acceleration

Figure 5.3 Lateral acceleration of bogie

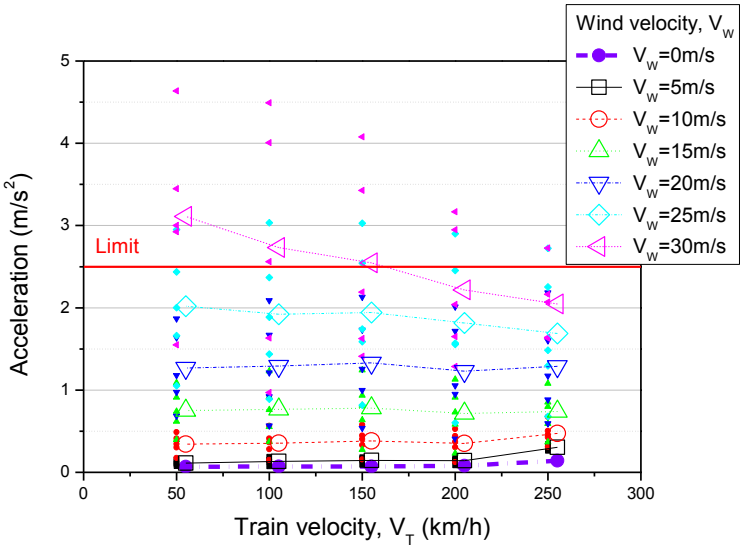

(a) Train velocity vs acceleration

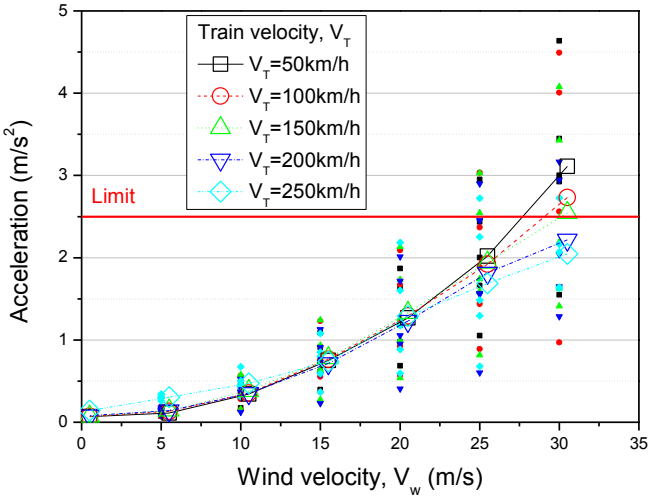

(b) Wind velocity vs acceleration

Figure 5.4 Lateral acceleration of carbody

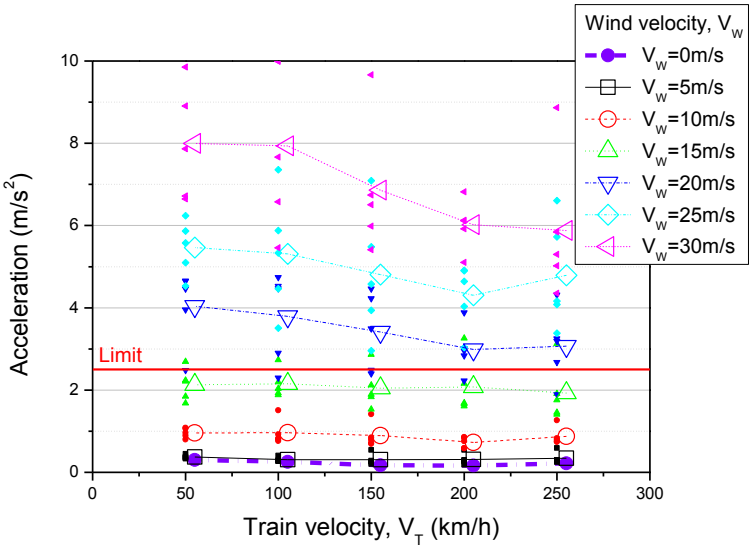

(a) Train velocity vs acceleration

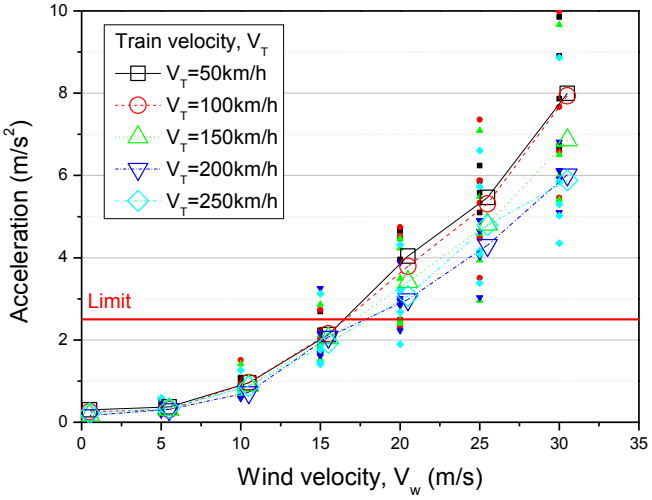

(b) Wind velocity vs acceleration

Figure 5.5 Vertical acceleration of carbody

5.3 Critical wind velocity

As a result of analyzing five indices described above, Figure 5.6 summarizes the whole cases categorized as follows.

- Green : Safe and GOOD running behavior
- Yellow : SAFE but Bad running behavior
- Red : DANGEROUS

In (a) the runnability is determined by the [mean] values, and in (b) it is determined by the [mean + 1 standard deviation] which performs a more conservative assessment than (a).

The train speed has to be limited according to the following instruction when applying the peak values of (a)

- If the wind velocity is below 20m/s, all train velocities satisfy the criteria of safety and running behavior.
- If the wind velocity is about 25m/s, train velocities below 200km/h satisfy the safety criterion only. (but do not satisfy the criterion of running behavior)

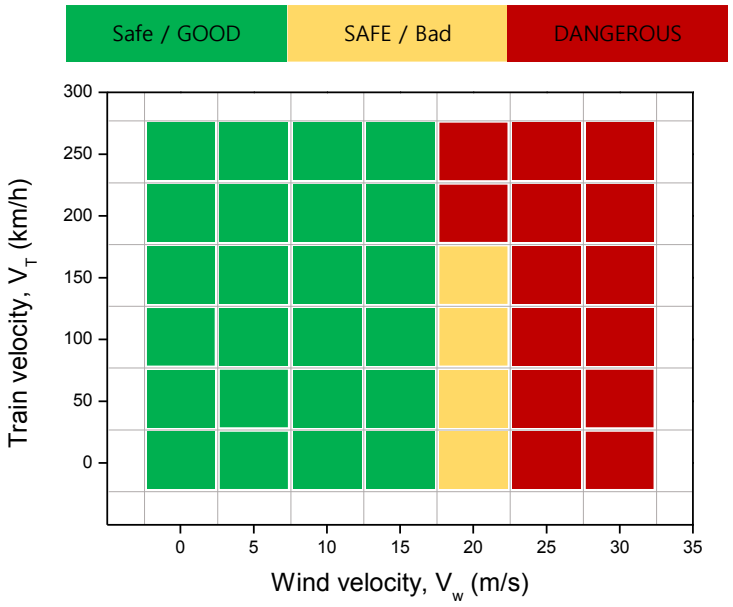

(a) Critical velocity according to mean responses

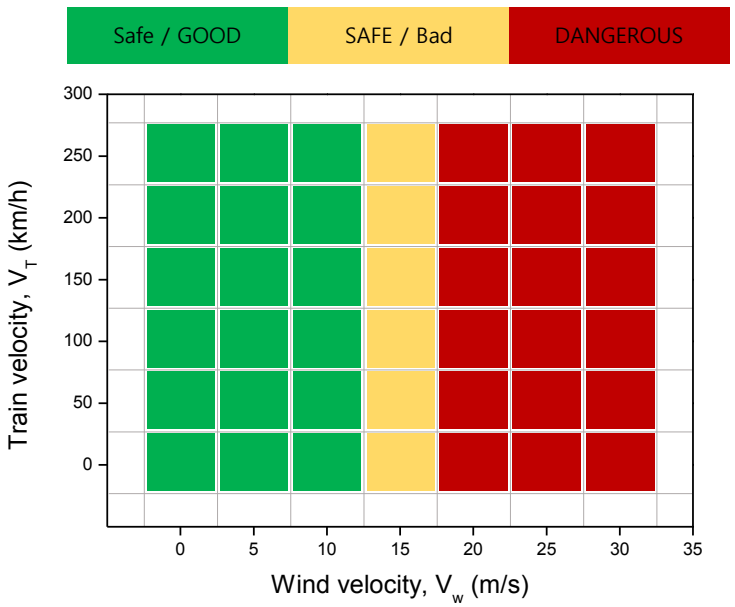

(b) Critical velocity according to (mean + 1 S.D.) response

Figure 5.6 Critical wind velocity

Chapter 6 Conclusions

A unified framework for the train/track/bridge/wind interaction was presented. The validity of the proposed method was confirmed by comparing its result to that of VI-Rail or previous study for each interaction step. With this framework, the runnability evaluation was performed as a target of running KTX on Yeongjong Bridge. The analysis for the various wind and train velocity could set up the critical velocity, and the additional parametric study investigated the impact factor that can affect the running behavior of train.

Unlike the previous analysis program, the proposed approach can reflect all the interaction among train, track, bridge and wind. To reflect the contact phenomenon between wheel and rail, calculated were the contact positions, creepages and contact forces on the basis of the contact theory. And since it combines the direct stiffness method for track modeling and the mode superposition method for substructure modeling, it can calculate the wheel/rail contact forces in consideration of track dynamics and improve the efficiency of the analysis in the track/bridge interaction. Finally System Matrix Approximation (SMA) method was embedded into the MSM to reflect the aeroelastic effect in bridge/wind interaction.

Through the parametric study and the runnability assessment of KTX on Yeongjong Bridge, the following conclusions can be obtained.

(1) The runnability of KTX train on Yeongjong Bridge under cross wind, is

more susceptible to the variation of wind velocity than the train velocity. It is because the dynamic movement of bridge which has direct relationship to the response of train over it, responds sensitively to the increase of wind velocity. However, as the train goes faster, the train speed increases the dynamic impact to bridge but decreases the exposure time to bridge vibration. Consequently the train speed does not give significant impacts to the running behavior of train on the bridge.

(2) The acceleration of train on a bridge is strongly correlated to the acceleration of bridge deck at the train position. Consequently the dynamic characteristics of the bridge response during the passing time can influence the safety and running behavior dominantly. In “some” cases under strong wind which vibrates the bridge violently, the train response was examined to become large even under lower train speed due to the increasing passing time. Therefore, the exposure time to wind load has to be categorized into one of major impact factors.

(3) Through the evaluation of running safety and riding comfort of train, the train speed has to be limited according to the following instruction when applying the peak values of [mean].

- If the wind velocity is below 20m/s, all train velocities satisfy the criteria of safety and running behavior.
- If the wind velocity is above 25m/s, train velocities below 200km/h satisfy the safety criterion only. (but do not satisfy the criterion of running behavior)

(4) As the safety of running train is closely related to the acceleration and displacement of bridge, the reflection of aeroelastic effect is inevitable. If the aeroelasticity is not included, the response of bridge would be overestimated under the strong wind condition, and the accurate evaluation for the safety could not be performed. As a way to consider the aeroelasticity, system matrix approximation method which can be combined to the mode superposition method, is concluded to be comparatively accurate and efficient.

(5) The track irregularity has a direct correlation to the variation of wheelload and bogie acceleration by the high-frequency, short-wave loading. On the other hand, the wind load vibrates the bridge in displacement and acceleration by the low-frequency, long-wave loading. The presence of wind is confirmed to give more dominant affects to the response of carbody than that of track irregularity.

References

[1] 채희남, 신영주, 임철수, 김강석, 정인철, 김준구, and 이오규, 2006, 일본 철도교의 현황과 설계 계산 예, 이엔지북.

[2] 이종수, and 주성문, 2006, 2006 Suspension Bridges in the World : 세계의 현수교, 현대건설주식회사, (주)유신코퍼레이션.

[3] Iwnicki, S., 2006, Handbook of railway vehicle dynamics, CRC press.

[4] Xu, Y., Ko, J., and Zhang, W., 1997, "Vibration studies of Tsing Ma suspension bridge," Journal of Bridge Engineering, 2(4), pp. 149-156.

[5] Yau, J.-D., Yang, Y.-B., and Kuo, S.-R., 1999, "Impact response of high speed rail bridges and riding comfort of rail cars," Engineering structures, 21(9), pp. 836-844.

[6] Yau, J.-D., Wu, Y.-S., and Yang, Y.-B., 2001, "Impact response of bridges with elastic bearings to moving loads," Journal of Sound and Vibration, 248(1), pp. 9-30.

[7] Au, F., Wang, J., and Cheung, Y., 2001, "Impact study of cable-stayed bridge under railway traffic using various models," Journal of Sound and Vibration, 240(3), pp. 447-465.

[8] Kargarnovin, M. H., Younesian, D., Thompson, D., and Jones, C., 2005, "Ride comfort of high-speed trains travelling over railway bridges," Vehicle System Dynamics, 43(3), pp. 173-197.

[9] Xu, Y., Zhang, N., and Xia, H., 2004, "Vibration of coupled train and cable-stayed bridge systems in cross winds," Engineering Structures, 26(10), pp. 1389-1406.

[10] Xia, H., and Zhang, N., 2005, "Dynamic analysis of railway bridge under high-speed trains," Computers & Structures, 83(23), pp. 1891-1901.

[11] Guo, W., Xia, H., and Xu, Y., 2010, "Running safety analysis of a train on the Tsing Ma Bridge under turbulent winds," Earthquake Engineering and Engineering Vibration, 9(3), pp. 307-318.

[12] Guo, W., Xia, H., De Roeck, G., and Liu, K., 2012, "Integral model for train-track-bridge interaction on the Sesia viaduct: Dynamic simulation and critical

assessment," Computers & Structures, 112, pp. 205-216.

[13] Chen, Z., and Chen, B., 2014, "Recent Research and Applications of Numerical Simulation for Dynamic Response of Long-Span Bridges Subjected to Multiple Loads," The Scientific World Journal, 2014.

[14] Xu, Y., Xia, H., and Yan, Q., 2003, "Dynamic response of suspension bridge to high wind and running train," Journal of Bridge Engineering, 8(1), pp. 46-55.

[15] Hertz, H., 1882, "Ueber die Berührung fester elastischer Körper," Journal für die reine und angewandte Mathematik, 1882(92), pp. 156-171.

[16] Carter, F., 1926, "On the action of a locomotive driving wheel," Proceedings of the Royal Society of London. Series A, 112(760), pp. 151-157.

[17] Vermeulen, P., and Johnson, K., 1964, "Contact of nonspherical elastic bodies transmitting tangential forces," Journal of Applied Mechanics, 31(2), pp. 338-340.

[18] Johnson, K. L., and Johnson, K. L., 1987, Contact mechanics, Cambridge university press.

[19] Kalker, J. J., 1990, Three-dimensional elastic bodies in rolling contact, Springer.

[20] Kalker, J., 1979, "Survey of wheel—rail rolling contact theory," Vehicle System Dynamics, 8(4), pp. 317-358.

[21] Kalker, J., 1991, "Wheel-rail rolling contact theory," Wear, 144(1), pp. 243-261.

[22] Kalker, J., 1982, "A fast algorithm for the simplified theory of rolling contact," Vehicle System Dynamics, 11(1), pp. 1-13.

[23] Polach, O., 2000, "A fast wheel-rail forces calculation computer code," Vehicle System Dynamics, 33, pp. 728-739.

[24] Garg, V., 1984, Dynamics of railway vehicle systems, Elsevier.

[25] Shabana, A. A., Zaazaa, K. E., and Sugiyama, H., 2010, Railroad vehicle dynamics: a computational approach, CRC Press.

[26] Shabana, A. A., 1997, "Flexible multibody dynamics: review of past and recent developments," Multibody system dynamics, 1(2), pp. 189-222.

[27] Shabana, A. A., Berzeri, M., and Sany, J. R., 2001, "Numerical procedure for the simulation of wheel/rail contact dynamics," Journal of Dynamic Systems, Measurement, and Control, 123(2), pp. 168-178.

[28] Shabana, A. A., and Sany, J. R., 2001, "An augmented formulation for mechanical systems with non-generalized coordinates: application to rigid body contact problems," Nonlinear dynamics, 24(2), pp. 183-204.

[29] Shabana, A. A., and Sany, J. R., 2001, "A survey of rail vehicle track simulations and flexible multibody dynamics," Nonlinear Dynamics, 26(2), pp. 179-212.

[30] Shabana, A. A., Zaazaa, K. E., Escalona, J. L., and Sany, J. R., "Modeling two-point wheel/rail contacts using constraint and elastic-force approaches," Proc. ASME 2002 International Mechanical Engineering Congress and Exposition, American Society of Mechanical Engineers, pp. 35-50.

[31] Shabana, A. A., Zaazaa, K. E., Escalona, J. L., and Sany, J. R., 2004, "Development of elastic force model for wheel/rail contact problems," Journal of Sound and Vibration, 269(1), pp. 295-325.

[32] Shabana, A. A., Tobaa, M., Sugiyama, H., and Zaazaa, K. E., 2005, "On the computer formulations of the wheel/rail contact problem," Nonlinear Dynamics, 40(2), pp. 169-193.

[33] Handoko, Y., 2006, "Investigation of the dynamics of railway bogies subjected to traction/braking torque," Centre for Railway Engineering, Central Queensland University.

[34] Handoko, Y., 2006, "Investigation of the dynamics of railway bogies subjected to traction/braking torque," Degree of Doctor of Philosophy, Central Queensland University Australia

[35] Yang, Y., Yau, J., and Wu, Y., 2004, Vehicle-bridge interaction dynamics, World Scientific.

[36] Yang, Y.-B., and Lin, B.-H., 1995, "Vehicle-bridge interaction analysis by dynamic condensation method," Journal of Structural Engineering, 121(11), pp. 1636-1643.

[37] Yang, F., and Fonder, G., 1996, "An iterative solution method for dynamic response of bridge–vehicles systems," Earthquake engineering & structural dynamics, 25(2), pp. 195-215.

[38] Yang, Y.-B., and Yau, J.-D., 1997, "Vehicle-bridge interaction element for dynamic analysis," Journal of Structural Engineering, 123(11), pp. 1512-1518.

[39] Yang, Y.-B., Yau, J.-D., and Hsu, L.-C., 1997, "Vibration of simple beams due to trains moving at high speeds," Engineering structures, 19(11), pp. 936-944.

[40] Yang, Y.-B., Chang, C.-H., and Yau, J.-D., 1999, "An element for analysing vehicle–bridge systems considering vehicle's pitching effect," International Journal for Numerical Methods in Engineering, 46(7), pp. 1031-1047.

[41] Yang, Y.-B., and Wu, Y.-S., 2001, "A versatile element for analyzing vehicle–bridge interaction response," Engineering Structures, 23(5), pp. 452-469.

[42] Yang, Y.-B., and Wu, Y.-S., 2002, "Dynamic stability of trains moving over bridges shaken by earthquakes," Journal of Sound and Vibration, 258(1), pp. 65-94.

[43] Wu, Y.-S., and Yang, Y.-B., 2003, "Steady-state response and riding comfort of trains moving over a series of simply supported bridges," Engineering Structures, 25(2), pp. 251-265.

[44] Yau, J.-D., and Yang, Y.-B., 2004, "A wideband MTMD system for reducing the dynamic response of continuous truss bridges to moving train loads," Engineering structures, 26(12), pp. 1795-1807.

[45] Matsumoto, N., Sogabe, M., Wakui, H., and Tanabe, M., 2004, "Running safety analysis of vehicles on structures subjected to earthquake motion," Quarterly Report of RTRI, 45(3), pp. 116-122.

[46] Sogabe, M., Ikeda, M., and Yanagisawa, Y., 2007, "Train-Running Quality during Earthquakes and Its Improvement for Railway Long Span Bridges," Quarterly Report of RTRI, 48(3), pp. 183-189.

[47] Tanabe, M., Matsumoto, N., Wakui, H., and Sogabe, M., 2011, "Simulation of a Shinkansen train on the railway structure during an earthquake," Japan journal of industrial and applied mathematics, 28(1), pp. 223-236.

[48] Zhai, W., Wang, Q., Lu, Z., and Wu, X., 2001, "Dynamic effects of vehicles on tracks in the case of raising train speeds," Proceedings of the Institution of Mechanical Engineers, Part F: Journal of Rail and Rapid Transit, 215(2), pp. 125-135.

[49] Chen, G., and Zhai, W., 2004, "A new wheel/rail spatially dynamic coupling model and its verification," Vehicle System Dynamics, 41(4), pp. 301-322.

[50] Zhai, W., Xia, H., Cai, C., Gao, M., Li, X., Guo, X., Zhang, N., and Wang, K., 2013, "High-speed train–track–bridge dynamic interactions–Part I: theoretical model and numerical simulation," International Journal of Rail Transportation, 1(1-2), pp. 3-24.

[51] Zhai, W., Wang, S., Zhang, N., Gao, M., Xia, H., Cai, C., and Zhao, C., 2013, "High-speed train–track–bridge dynamic interactions–Part II: experimental validation and engineering application," International Journal of Rail Transportation, 1(1-2), pp. 25-41.

[52] Xia, H., Xu, Y., and Chan, T. H., 2000, "Dynamic interaction of long suspension bridges with running trains," Journal of Sound and Vibration, 237(2), pp. 263-280.

[53] Xia, H., Zhang, N., and De Roeck, G., 2003, "Dynamic analysis of high speed railway bridge under articulated trains," Computers & structures, 81(26), pp. 2467-2478.

[54] Xia, H., Zhang, N., and Gao, R., 2005, "Experimental analysis of railway bridge under high-speed trains," Journal of Sound and Vibration, 282(1–2), pp. 517-528.

[55] Xia, H., Zhang, N., and Guo, W., 2006, "Analysis of resonance mechanism and conditions of train–bridge system," Journal of Sound and Vibration, 297(3), pp. 810-822.

[56] Xia, H., Han, Y., Zhang, N., and Guo, W., 2006, "Dynamic analysis of train–bridge system subjected to non-uniform seismic excitations," Earthquake engineering & structural dynamics, 35(12), pp. 1563-1579.

[57] Xia, H., Chen, J., Xia, C., Inoue, H., Zenda, Y., and Qi, L., 2010, "An experimental study of train-induced structural and environmental vibrations of a rail transit elevated bridge with ladder tracks," Proceedings of the Institution of Mechanical Engineers, Part F: Journal of Rail and Rapid Transit, 224(3), pp. 115-124.

[58] Xia, C., Xia, H., and De Roeck, G., 2014, "Dynamic response of a train–bridge system under collision loads and running safety evaluation of high-speed trains," Computers & Structures, 140, pp. 23-38.

[59] Chopra, A. K., 1995, Dynamics of structures, Prentice Hall New Jersey.

[60] Fryba, L., and Frýba, L., 1999, Vibration of solids and structures under moving

loads, Thomas Telford.

[61] 이윤석, 2002, "단순보 교량의 교량-차량 상호 작용에 대한 인자 연구," 석사, 서울대학교, 대한민국.

[62] 임명훈, 2004, "모드중첩법을 이용한 교량-차량 상호작용 해석," 석사, 성균관대학교, 대한민국.

[63] 이준석, 2007, "능동제어되는 자기부상열차-가이드웨이의 동적상호작용 해석," 박사, 성균관대학교, 대한민국.

[64] Miyata, T., 2003, "Historical view of long-span bridge aerodynamics," Journal of wind engineering and industrial aerodynamics, 91(12), pp. 1393-1410.

[65] Strømmen, E. N., 2006, Theory of bridge aerodynamics, Springer.

[66] Baker, C., 2014, "A review of train aerodynamics Part 1–Fundamentals," AERONAUTICAL JOURNAL, 118(1201), pp. 201-228.

[67] Baker, C., 2010, "The simulation of unsteady aerodynamic cross wind forces on trains," Journal of Wind Engineering and Industrial Aerodynamics, 98(2), pp. 88-99.

[68] Baker, C., Jones, J., Lopez-Calleja, F., and Munday, J., 2004, "Measurements of the cross wind forces on trains," Journal of Wind Engineering and Industrial Aerodynamics, 92(7), pp. 547-563.

[69] Diedrichs, B., Ekequist, M., Stichel, S., and Tengstrand, H., 2004, "Quasi-static modelling of wheel-rail reactions due to crosswind effects for various types of high-speed rolling stock," Proceedings of the Institution of Mechanical Engineers, Part F: Journal of Rail and Rapid Transit, 218(2), pp. 133-148.

[70] Orellano, A., and Schober, M., "Aerodynamic performance of a typical high-speed train," Proc. Proceedings of the 4th WSEAS International Conference on Fluid Mechanics and Aerodynamics, Elounda, Greece, pp. 18-25.

[71] Sanquer, S., Barre, C., de Virel, M. D., and Cleon, L.-M., 2004, "Effect of cross winds on high-speed trains: development of a new experimental methodology," Journal of Wind Engineering and Industrial Aerodynamics, 92(7), pp. 535-545.

[72] Bocciolone, M., Cheli, F., Corradi, R., Muggiasca, S., and Tomasini, G., 2008, "Crosswind action on rail vehicles: wind tunnel experimental analyses," Journal of

Wind Engineering and Industrial Aerodynamics, 96(5), pp. 584-610.

[73] Kwon, H.-B., Nam, S.-W., and You, W.-H., 2010, "Wind Tunnel Testing on Crosswind Aerodynamic Forces Acting on Railway Vehicles," Journal of Fluid Science and Technology, 5(1), pp. 56-63.

[74] Chen, Z., Xu, Y., Li, Q., and Wu, D., 2011, "Dynamic stress analysis of long suspension bridges under wind, railway, and highway loadings," Journal of Bridge Engineering, 16(3), pp. 383-391.

[75] Guo, W., and Xu, Y., 2001, "Fully computerized approach to study cable-stayed bridge–vehicle interaction," Journal of Sound and Vibration, 248(4), pp. 745-761.

[76] Guo, W., Xia, H., and Xu, Y.-l., 2007, "Dynamic response of a long span suspension bridge and running safety of a train under wind action," Frontiers of Architecture and Civil Engineering in China, 1(1), pp. 71-79.

[77] Guo, W., Xu, Y., Xia, H., Zhang, W., and Shum, K., 2007, "Dynamic response of suspension bridge to typhoon and trains. II: Numerical results," Journal of Structural Engineering, 133(1), pp. 12-21.

[78] Li, Y., Qiang, S., Liao, H., and Xu, Y., 2005, "Dynamics of wind–rail vehicle–bridge systems," Journal of Wind Engineering and Industrial Aerodynamics, 93(6), pp. 483-507.

[79] Xu, Y.-L., and Guo, W., 2003, "Dynamic analysis of coupled road vehicle and cable-stayed bridge systems under turbulent wind," Engineering structures, 25(4), pp. 473-486.

[80] Xu, Y., and Ding, Q., 2006, "Interaction of railway vehicles with track in cross-winds," Journal of Fluids and Structures, 22(3), pp. 295-314.

[81] Xu, Y., Guo, W., Chen, J., Shum, K., and Xia, H., 2007, "Dynamic response of suspension bridge to typhoon and trains. I: Field measurement results," Journal of Structural Engineering, 133(1), pp. 3-11.

[82] Yongle, L., Huoyue, X., Mengxue, W., and Shizhong, Q., 2012, "Wind loads and coupling vibration of wind-vehicle-bridge system in the process of two trains passing each other," The Seventh International Colloquium on Bluff Body Aerodynamics and Applications (BBAA7) pp. 1467-1473.

[83] 박흥석, 1998, "개선된 고속철도열차모형을 사용한 교량의 동적해석에 관한 연구," 박사, 연세대학교, 대한민국.

[84] Song, M.-K., Noh, H.-C., and Choi, C.-K., 2003, "A new three-dimensional finite element analysis model of high-speed train–bridge interactions," Engineering Structures, 25(13), pp. 1611-1626.

[85] Jung, K., Kim, H.-K., and Lee, H. S., 2013, "New Unified Approach for Aeroelastic Analyses Using Approximate Transfer Functions of Aerodynamic Forces," Journal of Engineering Mechanics, 140(4).

[86] 황성호, 2010, "차륜/레일 접촉점 산정을 위한 이산점의 회전변환 방법," 한국철도학회 학술발표대회논문집, pp. 1110-1115.

[87] 이정화, 2014, "케이블 강교량을 주행하는 열차의 횡풍에 대한 주행안전성 평가," 석사, 서울대학교, 대한민국.

[88] 이정화, 윤제성, and 김호경, 2013, "공기력에 미치는 어드미턴스 효과를 고려한 공간상 변동풍속 생성," 한국풍공학회지, 17(3), pp. 93-100.

[89] 대한토목학회, 2006, "케이블 강교량 설계지침,"대한민국.

[90] Hilber, H. M., Hughes, T. J., and Taylor, R. L., 1977, "Improved numerical dissipation for time integration algorithms in structural dynamics," Earthquake Engineering & Structural Dynamics, 5(3), pp. 283-292.

[91] Yang, S., 2009, "Enhancement of the finite-element method for the analysis of vertical train—track interactions," Proceedings of the Institution of Mechanical Engineers, Part F: Journal of Rail and Rapid Transit, 223(6), pp. 609-620.

[92] Clough, R. W., and Penzien, J., 1975, "Dynamics of structures."

[93] Liu, K., Zhang, N., Xia, H., and De Roeck, G., 2014, "A comparison of different solution algorithms for the numerical analysis of vehicle-bridge interaction," International Journal of Structural Stability and Dynamics, 14(02).

[94] Zhai, W., Wang, K., and Cai, C., 2009, "Fundamentals of vehicle–track coupled dynamics," Vehicle System Dynamics, 47(11), pp. 1349-1376.

[95] Xiao, X., Ling, L., and Jin, X., 2012, "A study of the derailment mechanism of a high speed train due to an earthquake," Vehicle System Dynamics, 50(3), pp. 449-470.

[96] Chollet, H., Sébès, M., Maupu, J. L., and Ayasse, J. B., 2013, "The VOCO multi-body software in the context of real-time simulation," Vehicle System Dynamics, 51(4), pp. 570-580.

[97] Iwnick, S., 1998, "Manchester benchmarks for rail vehicle simulation," Vehicle System Dynamics, 30(3-4), pp. 295-313.

[98] 2010, VI-Rail 14.0 Documentation, VI-grade GmbH.

[99] 조정래, 김동석, 김영진, 곽종원, and 장승엽, 2013, "PSC-I 거더 철도교량의 3차원 동적 이동하중 해석 모델," 한국철도학회 논문집, 16(4), pp. 286-297.

[100] Park, J., Jung, K., Hong, Y. H., Kim, H.-K., and Lee, H. S., 2013, "Exact Enforcement of the Causality Condition on the Aerodynamic Impulse Response Function Using a Truncated Fourier Series," Journal of Engineering Mechanics, 140(5).

[101] 국토교통부, 2013, "철도차량 안전기준에 관한 규칙,"대한민국.

[102] UIC, 2009, "Testing and approval of railway vehicles from the point of view of their dynamic bahaviour."

[103] Eurocode, 1990, "Basis of structural design(BS EN 1990-2002) ", British Standards.

국 문 초 록

본 논문에서 차량/궤도/교량/바람 사이에서 발생되는 상호작용을 함께 해석할 수 있는 통합 framework을 제안하였다. 차륜과 레일에서 발생되는 접촉 현상을 반영하기 위해, 접촉 이론에 근거하여 접촉 위치, 크리피지, 그리고 접촉력을 계산하였다. Direct Stiffness Method (DSM)와 Mode Superposition Method (MSM)을 조합하여 3차원 궤도/교량 상호작용 및 궤도 동역학을 반영하였으며, 효율적이면서도 정확하게 윤중과 횡압을 산정할 수 있었다. 마지막으로 System Matrix Approximation (SMA) 방법을 MSM에 적용하여 교량과 풍하중 사이에 발생하는 주파수 의존적 공탄성 효과를 반영하였다.

제안된 방법은 상용 패키지인 VI-Rail, 그리고 기존 문헌과의 비교/검증을 통해 각 상호작용에 대해 개별적으로 타당성을 확인하였다. 국내 유일의 철도 케이블 교량인 영종대교를 대상으로 시뮬레이션하여 KTX 열차의 주행성을 평가하였다. 다양한 풍속과 열차 속도에 대한 case 분석을 통해, 가정된 조건과 판정 기준에 의거하여 임계속도를 제안하였다.

추가적인 매개변수 해석을 통해 영종대교를 주행하는 열차의 동적 거동에 영향을 줄 수 있는 인자들에 대해 고찰하였다. 열차의 주행성은 열차의 속도보다는 풍속의 증가에 훨씬 민감하게 반응하는 것을 확인하였다. 이는 열차가 달리고 있는 교량의 동적 거동이 열차에 가장 큰 영향을 미치기 때문인 것으로 분석되었으며, 이에 따라 교량의 공탄성 효과는 반드시 반영되어야 함을 알 수 있었다.

주요어: 차량/궤도/교량/바람 상호작용, 주행성 평가,
궤도 동역학, 교량 공탄성
학 번: **2005-30271**